Università degli studi di Napoli Federico II

Facoltà di Scienze MM.FF.NN. Dipartimento di Scienze Fisiche

Dottorato di Ricerca XIX Ciclo

PhD Thesis in Fundamental and Applied Physics

November 2006

Adaptive Optics Techniques for Gravitational Wave Interferometers

Coordinator:

Prof. Gennaro Miele

Advisors:

Prof. Leopoldo Milano

Dr. Enrico Calloni

Author: Saverio Avino

To Isabel

Contents

Introduction **6**

1 Gravitational waves **9**

1.1 Einstein equations in the week-field approximation 9

1.2 Propagation of gravitational waves 11

1.3 Sources of gravitational waves 13

1.3.1 Gravitational waves generation 13

1.3.2 Supernovae 15

1.3.3 Coalescent binaries 16

1.3.4 Pulsars 16

1.3.5 Stochastic background 17

2 GW interferometric detection: the Virgo project **19**

2.1 Interferometric detection of gravitational waves 19

2.2 Shot-noise and quantum limit 22

2.3 Fabry-Perot cavities and recycling of light 23

2.4 Seismic noise 26

2.5 Thermal noise 28

2.6 The VIRGO experiment 30

2.6.1 introduction 30
2.6.2 Optical layout 31
2.6.3 Optics 33
2.6.4 Suspensions 34
2.6.5 The commissioning of the interferometer 37
2.6.6 Status of Virgo 39

3 Adaptive Optics 42

3.1 Introduction 42
3.2 Wavefront sensing 43
3.3 Wavefront control 47
3.4 Adaptive Optics applications 49

4 Adaptive optics system for the correction of aberrations of input laser beam in gravitational wave interferometers 52

4.1 Introduction 52
4.2 Effects of coupling between the interferometer asymmetries and the input beam jitters 54
4.3 Implementation of an Adaptive Optics system in gravitational wave interferometers 59
4.4 Adaptive Optics system based on interferometric wave-front sensing and membrane deformable mirror 61
4.4.1 Experimental Apparatus 61
4.4.2 Wavefront sensing 62
4.4.3 Actuation 69
4.4.4 Signal processing 72

4.4.5 Experimental results . . . 73
4.5 Implementation of a piezoelectric deformable mirror as actuator . . . 80
4.5.1 Piezoelectric deformable mirror . . . 80
4.5.2 Experimental results . . . 81
4.6 Discussion . . . 83

5 Generation of non-Gaussian flat laser beams 85
5.1 Introduction . . . 85
5.2 thermoelastic noise . . . 85
5.3 Mexican-Hat cavities and generation of flat-beam . . . 86
5.4 Generation of flat-beam by using deformable mirrors . . . 89
5.5 Results and discussion . . . 94

6 Scanning wavefront sensor for the analysis of thermal deformation effects of the Virgo mirrors 97
6.1 Thermal compensation problem . . . 97
6.2 Wavefront signal extraction . . . 101
6.2.1 Signals in DP and BS in the ideal case and introduction to approximations . . . 101
6.2.2 Signals in DP and BS in the not ideal case of input mirrors aberrations . . . 106
6.3 Scanning wavefront sensor . . . 110
6.4 Characterization of the PZT tip-tilt mirror . . . 112
6.4.1 Characterization of the PSD readout . . . 113
6.4.2 Characterization of the PZT mirror . . . 116
6.4.3 Tests results . . . 121

6.5 Implementation in Virgo: first images acquisition 123

Conclusion **131**

Appendix **132**

A Calculation of the c_{ij} coefficients **133**

Bibliography **139**

Acknowledgments **145**

Introduction

The present work has been carried out in the framework of Virgo experiment, a ground-based interferometric antenna for gravitational wave detection, located in Cascina (Pisa, Italy).

The gravitational waves are perturbations of the space-time metric propagating at th speed of light, foreseen by the General Theory of Relativity. The existence of gravitational waves has been provided indirectly in 1992 by J.H. Taylor and R.A. Hulse. They observed an orbital period decay of the binary system PSR 1913+16, which was in agreement with the results predicted by gravitational wave emission. However, not yet direct detection of gravitational waves has been performed. Indeed, is not possible to produce detectable gravitational waves in laboratory, and also those produced by astronomical objects are very weak and difficult to detect. For this reason, very complex and high sensitivity ground-based detectors have been built, in order to obtain the firsts gravitational wave detections and to study and observe the universe through a new observational window, that is developing a Gravitational Wave Astronomy.

Different kinds of gravitational wave detector have been developed; among them the most important and diffused presently are the ground-based laser interferometric detectors. An interferometric detector consists of a long baseline Michelson interferometer with a Fabry-Perot cavity implemented in each arm; the passage of a

gravitational wave causes a differential variation of the length of the arms, which is detected at the output of the interferometer as variation of the interference pattern. To detect the very small length variations expected (of the order of $10^{-18}m$), it necessary to reduce all the noise sources that can mask the signal, as for example, the seismic noise, the thermal noise, the shot-noise.

The various detectors presently in operation are near (or have already reached) the design curve of sensitivity. In this condition the interferometer, besides the isolation from the fundamental noises, must work in condition of extremely precision, especially in terms of alignments and wavefronts matching; for example, the angular jitter of the Virgo input laser, cleaned by an input mode-cleaner at the level of $10^{-11}rad/\sqrt{Hz}$, imposes that the mirrors of the cavities must be aligned with an accuracy of the order of $3 \times 10^{-9}rad$. In this thesis, it has been investigated the possibility to apply the Adaptive Optics techniques to improve the interferometer performances for these requirements. The first part of the work has been addressed to the problem of noise generated by the coupling of the laser input geometrical aberrations with the interferometer asymmetries. In particular, an adaptive optics system based on interferometric wavefront detection and deformable mirrors has been developed in order to correct the laser aberrations and to improve the beam matching to the interferometer. The system has shown performances in terms of efficiency, bandwidth and reintroduced noise which respect the specifics required for the application in the advanced Virgo interferometer.

In the second part, the use of this system has been extended to generate, starting from standard Gaussian laser beams, the so called Flat-Beams, which are laser beams with particular shape proposed for future detectors in order to reduce the effects of thermoelastic noise. First flat-beams have been generated demonstrating

the efficiency of this technique.

Finally, the third part, has been dedicated to the effects of thermal deformations of the Virgo mirrors. In fact, due to the high laser power used and to the non-zero absorption coefficients, part of the laser power is absorbed by Virgo optics, which are heated and then deformed. Therefore, a wavefront extraction technique is necessary to study the effects of these deformations on the fields circulating inside the interferometer. In particular, it has been studied a wavefront signal extraction technique to analyze the fields aberrations taking the main signals at the output of the interferometer. Then, a wavefront sensor based on a scanning pin-hole system to reconstruct field images at the modulation frequency has been developed. The system has been installed on the Virgo detection bench and first tests and image acquisitions have been performed, showing that Virgo is presently working at the limit of allowed aberrations.

The thesis is divided in six chapters. Chapters 1-2 are dedicated to an introduction to gravitational wave physics. In particular, there is a review of the gravitational waves, the expected sources, the principle of interferometric detection and a description of the Virgo interferometer. In chapter 3 there is a description of Adaptive Optics techniques. Chapter 4 reports the study and development of the adaptive optics system for the correction of the input laser aberrations, while in chapter 5 it is described the generation of Flat-Beams. Finally, chapter 6 is dedicated to the wavefront sensor developed for the analysis of the thermal deformations effects of the Virgo mirrors.

Chapter 1

Gravitational waves

1.1 Einstein equations in the week-field approximation

The existence of gravitational waves (GW) is foreseen by the theory of the general relativity of Einstein [1, 2, 3, 4]. In this chapter we shortly recall the principles of the theory and how from these it is possible to arrive to the forecast of the existence of the gravitational waves.

The structure and the evolution of the space-time, that is the metric tensor $g_{\mu\nu}$, are regulated by the Einstein field equations, which determine the $g_{\mu\nu}$ tensor and its derivatives (contained in the Ricci tensor $R_{\mu\nu}$) as function of impulse-energy tensor $T_{\mu\nu}$:

$$R_{\mu\nu} - \frac{1}{2} g_{\mu\nu} R \;=\; -\frac{8\pi G}{c^4} T_{\mu\nu} \tag{1.1}$$

where $R_{\mu\nu}$ is the contraction over two indices of the Riemann tensor $R_{\mu\nu\rho\sigma}$:

$$R^{\lambda}_{\mu\nu\kappa} \;=\; \frac{\partial \Gamma^{\lambda}_{\mu\nu}}{\partial x^{\kappa}} - \frac{\partial \Gamma^{\lambda}_{\mu\kappa}}{\partial x^{\nu}} + \Gamma^{\eta}_{\nu\mu}\Gamma^{\lambda}_{\kappa\eta} - \Gamma^{\eta}_{\mu\kappa}\Gamma^{\lambda}_{\mu\kappa} \tag{1.2}$$

and $\Gamma^{\lambda}_{\mu\nu}$ is the affine connection:

$$\Gamma^{\lambda}_{\mu\nu} \;=\; \frac{1}{2} g^{\sigma\lambda} \left(\frac{\partial g_{\nu\sigma}}{\partial x^{\mu}} + \frac{\partial g_{\sigma\mu}}{\partial x^{\nu}} - \frac{\partial g_{\mu\nu}}{\partial x^{\sigma}} \right)$$

The Ricci tensor contains the first and the second derivatives of the metric tensor, so that the vacuum field equations ($T_{\mu\nu} = 0$), as for the classical electrodynamics, foresee the existence of a free gravitational field, that is a gravitational waves field. The non linearity of Einstein equations and the Gauge freedom of the theory imply an high complexity in the resolution of the equations. If we consider the approximation of week-field, which is represented by a metric tensor given by the flat space-time tensor $\eta_{\mu\nu}$ plus a perturbative term $h_{\mu\nu}$:

$$g_{\mu\nu} = \eta_{\mu\nu} + h_{\mu\nu} \tag{1.3}$$

(where $h_{\mu\nu} \ll 1$)
the equations can be linearized by expanding the tensor $R_{\mu\nu}$ to the lowest order in $h_{\mu\nu}$. Then the Einstein equations become:

$$\Box^2 h_{\mu\nu} - \frac{\partial h^{\beta}_{\nu}}{\partial x^{\beta}\partial x^{\mu}} - \frac{\partial h^{\alpha}_{\mu}}{\partial x^{\alpha}\partial x^{\nu}} + \frac{\partial h^{\alpha}_{\alpha}}{\partial x^{\mu}\partial x^{\nu}} = -\frac{16\pi G}{c^4} S_{\mu\nu} \tag{1.4}$$

If we choice the gauge so that:

$$\partial_{\mu} h^{\mu}_{\nu} = \frac{1}{2}\partial_{\nu} h^{\mu}_{\mu} \tag{1.5}$$

we obtain the following form:

$$\Box^2 h_{\mu\nu} \;=\; -\frac{16\pi G}{c^4}[T_{\mu\nu} - \frac{1}{2}\eta_{\mu\nu} T^{\lambda}_{\lambda}] \tag{1.6}$$

The solution of this equation is:

$$h_{\mu\nu} = \frac{4G}{c^4}\int d^3\overrightarrow{x}\,\frac{[T_{\mu\nu} - 1/2\eta_{\mu\nu}T^{\lambda}_{\lambda}]_{t-r/c}}{|\overrightarrow{x} - \overrightarrow{x'}|} \tag{1.7}$$

From this solution we can see that the impulse-energy tensor not only produces a perturbation of the surrounding space-time metric, but moreover, variations of it

generate metric perturbations which propagate at the speed of light through the space-time. These are the gravitational waves.

1.2 Propagation of gravitational waves

Consider the vacuum field equation:

$$\Box^2 h_{\mu\nu} \;=\; 0 \qquad\qquad \partial_\mu h^\mu_\nu = \frac{1}{2}\partial_\nu h^\mu_\mu \tag{1.8}$$

A generic solution can be written as superposition of plane waves:

$$h_{\mu\nu} = \varepsilon_{\mu\nu}\exp(ik_\lambda x^\lambda) + \varepsilon^*_{\mu\nu}\exp(-ik_\lambda x^\lambda) \tag{1.9}$$

with

$$k_\lambda k^\lambda = 0 \qquad\qquad k_\mu \varepsilon^\mu_\nu = \frac{1}{2}k_\nu \varepsilon^\mu_\mu \tag{1.10}$$

The metric tensor ε^μ_ν describes the polarization of the wave and due to the gauge invariance it has six independent components. As in the case of electromagnetic waves, the gauge condition does not bring to a unique solution. There is a residual arbitrariness respect to coordinate transformations generated by functions $\xi^\mu(x)$ satisfying the equation $\partial^\alpha\partial_\alpha\xi^\mu$ (restricted gauge transformation). By using these transformations it is possible to reduce to two the independent components of the tensor ε^μ_ν. In particular it is possible to reduce ε^μ_ν to a traceless and transverse tensor to respect the wave propagation direction. This is called TT gauge (transverse and traceless) and the relative metric tensor is indicated as $h^{TT}_{\mu\nu}$.
In the particular case of a wave traveling along the z-axis, that is with $k^\mu = (k, 0, 0, k)$, we have:

$$\varepsilon_{\mu\nu} = h_+\varepsilon^+_{\mu\nu} + h_\times\varepsilon^\times_{\mu\nu} \tag{1.11}$$

with $\varepsilon^+ = \begin{pmatrix} 0 & 0 & 0 & 0 \\ 0 & 1 & 0 & 0 \\ 0 & 0 & -1 & 0 \\ 0 & 0 & 0 & 0 \end{pmatrix}$ $\varepsilon^\times = \begin{pmatrix} 0 & 0 & 0 & 0 \\ 0 & 0 & 1 & 0 \\ 0 & 1 & 0 & 0 \\ 0 & 0 & 0 & 0 \end{pmatrix}$

From the expressions ε^+ and $\varepsilon^\times$ we can see that a tensor is obtained by the other through a rotation of $\pi/4$. Therefore, the gravitational field, under our hypotheses, is described by a massless particle of spin 2: the graviton.

To understand the effect of a gravitational wave over a set of particles in free-fall, we need to recall the geodesic deviation equation. If $\xi^\alpha = x_2^\alpha - x_1^\alpha$ is the quadrivector distance between two mass in free-fall, we can write the following equation:

$$\frac{D^2\xi^\alpha}{D\tau^2} + R^\alpha_{\beta\gamma\delta}\frac{dx^\beta}{d\tau}\xi^\gamma\frac{dx^\delta}{d\tau} = 0 \tag{1.12}$$

where $D/D\tau$ is the covariant derivative. In the Newtonian limit the geodesic deviation equation become:

$$\frac{d^2\xi^i}{d\tau^2} + R^i_{0j0}\xi^j = 0 \tag{1.13}$$

which is the classical tidal force equation. It is possible to demonstrate that in TT gauge it is worth the relation $R_{i0j0} = 1/2\, h_{ij,00}$, by this the eq. 1.13 become:

$$\frac{d^2\xi^i}{d\tau^2} = 1/2\, h_{ij,00}\xi_j \tag{1.14}$$

where $\xi^i = x_1^i - x_2^i$. The solution of the eq. 1.14 is:

$$\delta\xi_i = \frac{1}{2}h_{ij}\xi_j \tag{1.15}$$

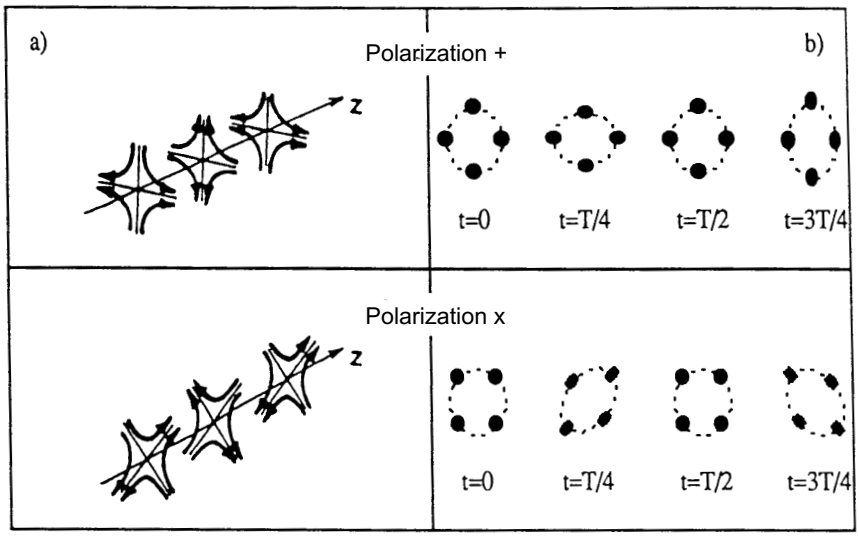

Figure 1.1: a) lines of force of a plane gravitational wave for the two polarization states; b) effect of a gravitational wave over a circular set of masses varying on time.

Therefore, the effect of a gravitational wave over two mass in free-fall is to vary the relative distance along the directions perpendiculars to the wave propagation direction. This proves that the gravitational waves are transversal waves. In fig. 1.1 are shown the lines of forces of a plane gravitational wave for the two polarization states, and the effect of a gravitational wave over a circular set of masses varying on time.

1.3 Sources of gravitational waves

1.3.1 Gravitational waves generation

In this paragraph we describe the possible sources of gravitational waves in the frequency band (from few Hz to few kHz) of interest for ground based interferometers [5, 6, 7, 8, 9]. Consider the equation 1.7. Under the hypothesis that the source

dimension R are much smaller either than the distance from the observation point, or than the wavelength of the waves emitted, it is possible to perform a multipole expansion like for electromagnetic waves. From the conservation of momentum and angular momentum laws, we obtain that the first non-null term is the quadrupole momentum:

$$h_{jk}^{TT} = \frac{2G}{rc^4}\left(\frac{d^2 I_{jk}^{TT}}{dt^2}\right)_{t-r/c} \tag{1.16}$$

where

$$I_{jk} = \int d^3\overrightarrow{x}\,\rho\left(x_j x_k - \frac{1}{3}|\overrightarrow{x}|^2\right) \tag{1.17}$$

While the power emitted is:

$$\frac{dE}{dt} = \frac{1}{5}\frac{G}{c^5}\sum_{jk}\left|\frac{d^3 I_{jk}}{dt^3}\right|^2 \tag{1.18}$$

Now we can estimate the order of magnitude of the energy emitted by a source as gravitational waves. Consider a body of mass M and dimension R, and suppose that the quadrupole momentum vary on a time scale T. We have:

$$\frac{dE}{dt} \sim \frac{1}{5}\frac{G}{c^5}\left(\frac{MR^2}{T^6}\right)^2 \sim L_0\left(\frac{v}{c}\right)^6\left(\frac{r_{Sch}}{R}\right)^2 \tag{1.19}$$

where $L_0 = 3.6\cdot 10^{59}\, erg\, s^{-1}$ and r_{Sch} is the Schwarzschild radius of the body ($r_{Sch} = GM/c^2$). Even if we obtain this result under the hypotheses of week-field and low velocity, we can deduce that the emission of gravitational waves assume importance for relativistic and compact objects. From eq. 1.19 we understand the impossibility to generate in laboratory gravitational waves of consisting amplitude. Then, the efforts of the physicists community are concentrated on the detection of gravitational

waves generated by astrophysics sources.

The gravitational waves and its sources are typically classified based on its temporal behavior. We have: *impulsive waves* when the duration of the event is smaller than observation time (for example the radiation emitted by a Supernova); *periodic waves* when temporal behavior is sinusoidal with frequency f constant over time of the order of observation time (for example the radiation emitted by pulsars); *stochastic waves* when their amplitude vary casually (for example the cosmic background radiation).

1.3.2 Supernovae

The Supernovae are the result of gravitational collapse of the nuclei of stars enough massive. The collapse bring to the formation of neutron stars which should generate gravitational waves. The amplitude of the waves depend on the velocity and asphericity of the collapse. If f is the characteristic frequency (the inverse of the collapse time) and ΔE_{gw} is the energy emitted as gravitational waves, we have:

$$h \sim 2.7 \cdot 10^{-20} \left(\frac{\Delta E_{gw}}{M_0 c^2}\right)^2 \left(\frac{1kHz}{f}\right) \left(\frac{10Mpc}{r}\right) \tag{1.20}$$

where r is the distance between the source and the Earth and M_0 is the solar mass. Some models with axial symmetry foresee the values $10^{-5} < \Delta E_{gw}/M_0 c^2 < 6 \cdot 10^{-3}$. In our galaxy, that is in a radius of about 10 kpc, it is estimated a Supernova explosion each 40 years. In the Virgo cluster (at about 10 Mpc from the Earth), it is expected some event for year. The Virgo project has been planned with a sensitivity sufficient to detect these signals.

1.3.3 Coalescent binaries

Not all the coalescing systems can represent detectable sources; only the systems composed by strongly compact objects, like neutron stars and black-hole, can produce observable radiation. The coalescent binaries emit, as gravitational waves, a great amount of energy comparable to the Supernovae emissions, but the wave amplitude is much less, since the energy is emitted during many cycles. The characteristic time of the observable impulse is a few of minutes, during this time the frequency changes from some tens of Hz to some kHz, and the estimated amplitude is:

$$h \sim 10^{-23} \left(\frac{\mu}{M_0}\right)^{\frac{3}{2}} \left(\frac{M}{M_0}\right) \left(\frac{f}{100}\right)^{\frac{3}{2}} \left(\frac{100Mpc}{r}\right) \tag{1.21}$$

These coalescences, in a radius of about 100 Mpc, should have a rate of some event for year.

We observe that in our galaxy exists a precursor of a coalescent binary system: the binary PRS 1913+16, which has an estimated lifetime (before the coalescence) of about 10^8 years. This system is very important as an indirect proof of the existence of gravitational waves. In fact, the observed decay velocity is in agreement with the general relativity forecasts.

1.3.4 Pulsars

Some of the most important periodic sources are the rotating neutron stars not symmetric in the axis. In our galaxy these stars are in number of about $n = 10^8$, but the greater part of them rotate so slowly, or are so symmetric, to generate wave too weak to be detected with present technology. The amplitude of the wave depends by the momentum of inertia of the star I_{zz}, by the distance from the Earth,

by the ellipticity ε in the equatorial plane, and by the frequency emission f (which is double the rotation frequency):

$$h \sim 8 \cdot 10^{-19} \varepsilon \left(\frac{I_{zz}}{10^{38}\, Kg\, m^2} \right) \left(\frac{f}{1Khz} \right)^2 \left(\frac{10Kpc}{r} \right) \tag{1.22}$$

Generally, since the ellipticity is small (about $\varepsilon \leq 10^{-5}$), the amplitude is smaller than the sources considered above, but the periodicity allows to integrate over a sufficiently long time. In particular, in our galaxy we already know the pulsars Crab and Vela (neutron stars with non-null magnetic momentum visible through radiotelescopes). The emission frequencies are respectively 64 *Hz* and 22 *Hz*, the estimated amplitude is of the order of $10^{-24} - 10^{-26}$. Considering the Virgo project sensitivity design, it could be possible to observe them by integrating the signal over a time of about one year.

1.3.5 Stochastic background

Another possible source of gravitational waves is the relic stochastic background produced during the early expansion of the universe. The detection of this gravitational radiation can gives informations about the state of the universe at time scales $t \approx 10^{-20} - 10^{-26}\ s$ or equivalent at temperature scales $t \approx 10^7 - 10^{10}$ GeV [10].
The stochastic gravitational radiation is composed by the random superposition of different components and is characterized by the dimensionless parameter:

$$\Omega_{GW}(f) = \frac{1}{\rho_c} \frac{d\, \rho_{GW}(f)}{d\, log f} \tag{1.23}$$

where $\rho_{GW}(f)$ is the energy density of the GW stochastic background and ρ_c is the critical energy density to close the universe.
Most inflationary models predict a flat spectrum for $\rho_{GW}(f)$. The strictest limits on $\rho_{GW}(f)$ are imposed by the COBE observations of CMBR anisotropy [11].

These limits concern frequencies outside the detection frequency band of the GW interferometric detectors, but if we consider these limits valid also in this region we can conclude that it is not possible to detect relic GW radiation with present interferometers. Nevertheless, recent string cosmology models [12] predict a different and more complex spectrum for $\rho_{GW}(f)$ which is compatible with the COBE limits and at the same time predicts gravitational radiation detectable with present GW interferometers.

Chapter 2

GW interferometric detection: the Virgo project

2.1 Interferometric detection of gravitational waves

In this chapter we describe the GW interferometric detection principle with particular care to the Virgo detector [5, 13, 14, 15]. Considering the effect of a gravitational wave over a circular set of masses varying on time (eq. 1.15 e fig. 1.1b), it is natural to think to use a Michelson interferometer as antenna. Looking at fig. 2.1, consider a gravitational wave polarized along the axis x and y (+ polarization) impinging on the Michelson interferometer. If we suppose that the interferometer mirrors are free-fall masses, from the eq. 1.15 follows that the effect of the gravitational wave is an alternated squeezing and stretching of the interferometer arms (see fig. 2.1). From the variation of interference pattern it is possible to reconstruct the pass of the gravitational wave.

The use of an interferometer with free-fall optics on Earth is an ideal case. Consider now the real case of an interferometer with optics suspended by mechanical pendulum with resonance frequency ω_0 and time constant τ. If L is the arm length

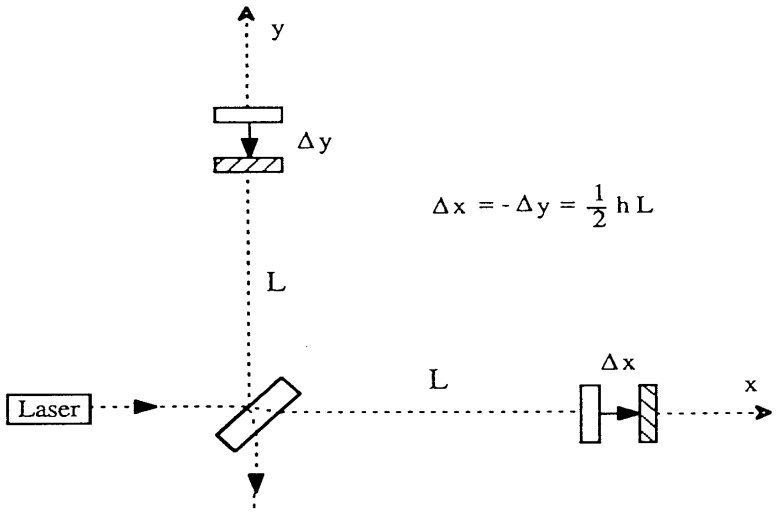

Figure 2.1: Effect of a gravitational wave over a Michelson interferometer, the propagation direction of the wave is perpendicular to the plane of the figure.

of the interferometer, the equations describing the behavior of a mirror are:

$$\ddot{\Delta x} + \frac{1}{\tau}\dot{\Delta x} + \omega_0^2 \Delta x = \frac{1}{2}\ddot{h}_+ L \tag{2.1}$$

$$\ddot{\Delta y} + \frac{1}{\tau}\dot{\Delta y} + \omega_0^2 \Delta y = -\frac{1}{2}\ddot{h}_+ L \tag{2.2}$$

where Δx and Δy are respectively the the length variations of the x and y axis. An analogous equation is worth for the optical paths phase difference $\Delta\phi = 4\pi/\lambda(\Delta x - \Delta y)$:

$$\ddot{\Delta\phi} + \frac{1}{\tau}\dot{\Delta\phi} + \omega_0^2 \Delta\phi = \frac{4\pi}{\lambda}\ddot{h}_+ L \tag{2.3}$$

The solution of this equation in the case of a periodic gravitational wave of frequency Ω, $h(t) = h_0 e^{-i\Omega t}$, is:

$$\Delta\phi = \frac{4\pi L}{\lambda} \frac{-\Omega^2 h_0\, e^{-i\Omega t}}{\omega_0^2 - \Omega^2 + i\Omega/\tau} \tag{2.4}$$

for frequencies $\Omega \gg \omega_0$ we have:

$$\Delta\phi = \frac{4\pi L}{\lambda} h_0 \, e^{-i\Omega t} \tag{2.5}$$

That is, for frequencies Ω much greater than the resonance frequency of the pendulum sustaining the mirror, the mirror behaves like a free-fall mass. By measuring ϕ it is possible to detect the gravitational wave.

Up to now, we supposed that the phase-difference measured by the interferometer is due only to the mirrors position variations. In truth the gravitational wave also interact directly with the photons changing the flight time inside the interferometer. Therefore, the total phase is due by the sum of a spatial contribution (mirrors motion) plus a temporal contribution (variation of flight time of the photons). In a more rigorous approach the phase-difference induced by a gravitational wave in the interferometer is:

$$\Delta\phi = \frac{4\pi L}{\lambda} \frac{\sin \frac{\Omega L}{c}}{\frac{\Omega L}{c}} \, h(t - L/c) \tag{2.6}$$

In the limit $\Omega L/c \ll 1$, that is $L \ll \lambda_{og}$, we find again the equation 2.5.

From eq. 2.5 we observe that the phase-difference $\Delta\phi$ is proportional to the arm length of the interferometer. This is the reason for which, compatible with costs, long-arm gravitational wave interferometers (a few Km) have been designed. Consider an interferometer with arm-length of about 3 Km (like Virgo), if it is crossed by a gravitational wave of amplitude 10^{-21} (typical value at 10 Hz), the motion of the mirror is of the order of 10^{-18} m. The weakness of this signals impose the construction of apparatus extremely sensitive and complex. In the next paragraphs we describe the main characteristics and limitations of these detectors.

2.2 Shot-noise and quantum limit

The interferometric detection of gravitational waves essentially consists in the measurement of phase-difference of the beams in the two interferometer arms. This can be done simply by measuring the intensity at the output port of the interferometer using a photodiode. One of the fundamental noise which limits this kind of measure is the shot-noise, that is the statistic fluctuation of the number of photons coming on the photodiode. In particular, the uncertainty in measuring the phase and the photons number is regulated by the uncertainty relation $\Delta\phi\Delta n \geq 1$. Considering that a coherent state of photons has a poissonian distribution, that is $\Delta n = \sqrt{n}$, it follows an uncertainty on the phase given by:

$$\Delta\phi = \sqrt{\frac{\hbar\omega}{\eta P_0 t}} \tag{2.7}$$

where P_0 is the power of the input laser, $\omega/2\pi$ is the frequency of the laser, η the quantum efficiency of the photodiode and t is the measure time. The shot-noise of the photons has a flat spectrum at level (in phase units):

$$\widetilde{\Delta\phi} = \sqrt{\frac{2\hbar\omega}{\eta P_0}}\,\frac{rad}{\sqrt{Hz}} \tag{2.8}$$

If we confront this noise with the amplitude of gravitational wave signal given by the equations 2.5 and 2.6, we can find a limit for the minimum value of $\widetilde{h}$ allowed:

$$\widetilde{h} = \frac{\lambda}{4\pi L}\sqrt{\frac{2\hbar\omega}{\eta P_0}}\,\frac{1}{\sqrt{Hz}} \tag{2.9}$$

where we supposed $\Omega L/c \ll 1$.

From eq. 2.9 we can see that it is possible to reduce the shot-noise effect by increasing

the input power P_0. But an increase of the power increases the noise induced by the pressure fluctuations on the mirrors. In fact, the mirrors are subject to a force F due to the radiation pressure:

$$F = 2n\frac{\hbar\omega}{c} \tag{2.10}$$

where n is the number of photons which hit the mirror per unit time. Each fluctuation of the photon flux causes a variation of the force F and then a displacement of the mirror. The variation of phase-difference at the output of the interferometer as function of frequency Ω is:

$$\widetilde{\Delta\phi} = \frac{4\pi}{\lambda}\frac{\sqrt{8P_0\hbar\omega}}{M\Omega^2 c} \tag{2.11}$$

where M is the mass of the mirror. In this calculation we supposed the frequency Ω is much greater than the resonance frequency of the pendulum which suspends the mirror. If we sum the two contributions, that is the photons shot-noise and the pressure fluctuations, we have:

$$\widetilde{\Delta\phi}_n = \sqrt{\frac{2\hbar\omega}{\eta P_0} + \left(\frac{4\pi}{\lambda}\right)^2 \frac{8P_0\hbar\omega}{(M\Omega^2 c)^2}} \tag{2.12}$$

From this relation we see that it exists an optimal power for which $\widetilde{\Delta\phi}_n$ has a minimum:

$$\widetilde{\Delta\phi}_n = \widetilde{\Delta\phi}_{Q.L.} = \frac{4\pi}{\lambda}\frac{1}{\eta^{1/4}}\sqrt{\frac{4\hbar}{M\omega^2}} \tag{2.13}$$

The quantity $\widetilde{\Delta\phi}_{Q.L.}$ represents the quantum limit to determination of the phase.

2.3 Fabry-Perot cavities and recycling of light

As we saw in the paragraph 2.1 the phase-difference induced by a gravitational wave at the output of the interferometer is proportional to its arms length. Considering

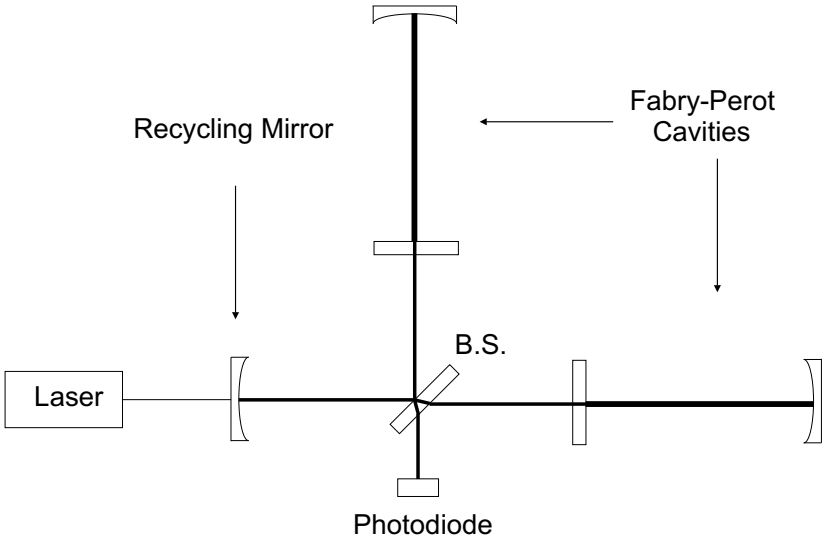

Figure 2.2: Recycled Fabry-Perot Michelson interferometer.

that arms length of a few Km is at the best of present technology (and costs), a way to improve the sensitivity of the detector, without changing the arms length, is to increase the optical path by using delay-lines or Fabry-Perot cavities.
In the case of delay-lines, a mirror is added in each arm near the beam-splitter. The light beam passes through the arm many times before to recombine with the other beam at the beam-splitter. In this way the phase difference induced by a displacement of the mirrors is multiplied by the number of round-trip of the beams inside the delay-lines.

An alternative method, widely used in gravitational wave interferometers, is to implement a Fabry-Perot cavity in each interferometer arm (see fig. 2.2). As in the case of delay-lines, the light before recombining, is stored in the two cavities for a time proportional to their Finesse F. If the cavity is in resonance, the variation Δd of the cavity length produces a phase variation $\Delta\phi$ on the reflected beam given by:

$$\Delta\phi_{F.P.} = \frac{4\pi}{\lambda}\frac{2F}{\pi}\Delta d \tag{2.14}$$

Therefore, a Fabry-Perot cavity of Finesse F is equivalent to a delay-line with $N = 2F/\pi$. The phase-difference induced by a gravitational wave of frequency Ω at the output of a Fabry-Perot Michelson interferometer is:

$$\Delta\phi_{F.P.} = \frac{4\pi}{\lambda}\frac{2F}{\pi}\frac{h\,L}{\sqrt{1+\left(\frac{2F}{\pi}\frac{\Omega L}{c}\right)^2}} \tag{2.15}$$

As we will see in the next paragraph, the position of the mirrors is controlled in real-time through a feed-back system so to keep the interferometer in the condition of destructive interference (also called dark-fringe). The passing of a gravitational wave, or any other effect which try to move the mirror position, induces a reaction signal in the feed-back system which represents the signal of the antenna. In the configuration of dark-fringe the light is almost all reflected back toward the interferometer. It is possible to use this light placing a mirror in front of the laser which reflects back toward the interferometer. This technique is note as *recycling* of the light. In practice, the recycling mirror and the whole interferometer form a new cavity, in which the recycling mirror is the first mirror while the interferometer is the second one, this is called recycling cavity. If the cavity is in resonance with the input laser, the power inside the interferometer (that is the power on the beam-splitter) increases of a factor depending by the Finesse of this new cavity. Consequently, there is a decrease of the shot-noise limit and then an increase of phase sensitivity. The power increasing factor depends by the reflectivity of the recycling mirror and

the reflectivity of the interferometer:

$$P_0 \rightarrow P_0 \frac{t_r^2}{(1 - r_r r_{ITF})^2} \tag{2.16}$$

where r_r and t_r are respectively the reflectivity and the transmittivity of the recycling mirror, while r_{ITF} is the reflectivity of the interferometer. Exactly r_{ITF} represents the portion of light incident upon the beam-splitter which is reflected back toward the laser when the interferometer is in the condition of dark-fringe. Then, the quantity $p_{ITF} = 1 - r_{ITF}^2$ is the light-loss inside the interferometer. It is possible to demonstrate that there is an optimal reflectivity r_r, dependent by the light-loss, for which we obtain the maximum power inside the recycling cavity, that is:

$$P_0 \rightarrow P_0 S = P_0 \frac{1}{p_r + p_{ITF}} \tag{2.17}$$

where S is the recycling factor and p_r are the losses in the recycling mirror. From this we deduce that to obtain an high recycling factor we need to reduce at minimum the losses inside the interferometer.

2.4 Seismic noise

As we saw above, to detect a gravitational wave of amplitude 10^{-21} we need to measure a displacement of the mirrors of about 10^{-18} m. Therefore, any external vibration which propagates to the mirror can introduces spurious signals or can compromise even the functioning of the detector. In particular, the seismic vibrations of the ground are many order of magnitude greater than the displacements which we need to detect.

Typically, above some *Hz*, the spectrum of seismic vibrations is well approximated

by the empirical expression:

$$\widetilde{x}_t = \frac{a}{f^2}\frac{m}{\sqrt{Hz}} \tag{2.18}$$

with $10^{-7} < a < 10^{-6}$. If these vibrations propagate to the mirror, producing a displacement $\widetilde{x}_s$, it will be possible to detect a gravitational wave of amplitude $\widetilde{h}$ only if $\widetilde{h} > \widetilde{x}_s/L$, independently by the use of techniques of optical amplification of the signal (delay-line or Fabry-Perot). It follows that it is possible to reduce the effect of vibrations $\widetilde{x}_s$ induced by seismic noise only by increasing the interferometer arm-length. But since it is not possible to build interferometer with arm-length greater than a few Km, it is necessary to implement very efficient seismic noise attenuation systems.

The typically attenuation systems used consist of a chain of pendula in cascade. Consider a mirror suspended to a pendulum of frequency ω_0 and time constant τ. The mirror displacement x_s, induced by seismic vibrations x_t of the suspension point, is:

$$\widetilde{x}_s = FT(\omega)\widetilde{x}_t = \frac{\omega_0^2}{-\omega^2 + \omega_0^2 + i\omega/\tau}\widetilde{x}_t \tag{2.19}$$

The function $FT(\omega)$ is the transfer function of seismic vibrations from the suspension point to the mirror. $FT(\omega)$ has a maximum (in module) at resonance frequency of the pendulum. For frequencies $\omega \gg \omega_0$ the behavior is:

$$\frac{\widetilde{x}_s}{\widetilde{x}_t} = -\frac{\omega_0^2}{\omega^2} \tag{2.20}$$

that is, for frequency greater than the resonance frequency the seismic vibrations are attenuated by a factor ω_0^2/ω^2. Then a pendulum is a two-pole mechanical low-pass filter with cut-frequency ω_0. Therefore, for a fixed frequency $\omega(> \omega_0)$, we can

increase the attenuation by lowering the resonance frequency of the pendulum and by using several pendula in cascade.

2.5 Thermal noise

The thermal noise is one of the fundamental limits in many mechanical measures. In the case of interferometric gravitational wave detectors there are two fundamental contributes: the first one is the thermal noise associated to the resonance modes of the mirror suspensions, the second one is the thermal noise associated to the resonance normal modes of the mirrors.

The fluctuation-dissipation theorem states that when a physical system presents mechanisms of dissipation there are thermal stochastic forces with power spectral density given by:

$$\widetilde{F}^2(\omega) = 4K_B\,T\,R(\omega) \tag{2.21}$$

where $R(\omega)$ is the real part (damping force) of the mechanical impedance $Z(\omega) = F(\omega)/v(\omega)$ at frequency ω. This stochastic force produces a Brownian motion of the system with power spectral density given by:

$$\widetilde{x}_t^2(\omega) = \frac{4K_B\,T\,R(\omega)}{\omega^2|Z(\omega)|^2} \tag{2.22}$$

In the typical case of an oscillator damped by dissipative force proportional to the velocity, $R(\omega)$ becomes a constant ($R(\omega) = m/\tau$) depending by the mass m and the time constant τ. If the oscillator resonance frequency is $\omega_0 = \sqrt{k/m}$, the power spectral density of the displacement due to the thermal noise is:

$$\widetilde{x}_t^2(\omega) = \frac{4K_B\,T\,m/\tau}{m^2((\omega^2-\omega_0^2)^2 + (\omega/\tau)^2)} \tag{2.23}$$

For the pendulum mode of the suspension, the resonance frequency ω_0 is below the bandwidth ($\omega_0 \ll \omega$) for the detection of gravitational waves, so the eq. 2.23 becomes:

$$\widetilde{x}_t(\omega) = \frac{\sqrt{4K_B\,T\,m/\tau}}{m\,\omega^2} = \frac{1}{\omega^2}\sqrt{\frac{4K_B\,T\,\omega_0}{m\,Q}} \tag{2.24}$$

where $Q = \omega_0\,\tau$ is the suspension quality factor. Then thermal noise effect decreases with increasing the frequency ω. Moreover, by eq. 2.24 we see that the effect of thermal noise can be reduced by increasing the suspension quality factor Q and by increasing the mass of the mirror.

The noise due to the resonance modes of the mirror can be described as a set of oscillators corresponding to its normal modes. In this case the frequencies are of the order of several kHz, then above the bandwidth of detection; so the eq. 2.24 becomes:

$$\widetilde{x}_t(\omega) = \sqrt{\sum_i \frac{4K_B\,T\,m_i/\tau_i}{m_i^2\,\omega_i^4}} = \sqrt{\sum_i \frac{4K_B\,T}{m_i\,Q_i\,\omega_i^3}} \tag{2.25}$$

where m_i is the effective mass of the mirror corresponding to the normal mode i with resonance frequency ω_i. We can see that the thermal noise effect decreases with increasing of the mirror Q factor and with increasing of the resonance frequency ω_i. Finally, we can notice that, as for the seismic noise, also for the thermal noise there is a decreases (with L^{-1}) of the interferometer sensitivity independently by the use of techniques of optical amplification of the signal (delay-line or Fabry-Perot).

2.6 The VIRGO experiment

2.6.1 introduction

The gravitational wave detector VIRGO, supported by CNRS (France) and INFN (Italy), consists mainly of a recycled Michelson interferometer where each arm is replaced by a 3 *km* long Fabry-Perot cavity. VIRGO (see fig. 2.3) is located at the European Gravitational Observatory (EGO), close to Cascina (Pisa, Italy), and is designed to detect gravitational waves with sensitivity in spectral density $\widetilde{h}$ of about $10^{-23}1/\sqrt{Hz} - 3 \cdot 10^{-22}1/\sqrt{Hz}$ in a frequency range near 100 *Hz*. This corresponds, in terms of relative displacements of the test masses, to measure length variations of less than $10^{-19}m/\sqrt{Hz}$. Other detectors presently in action, such as LIGO, TAMA

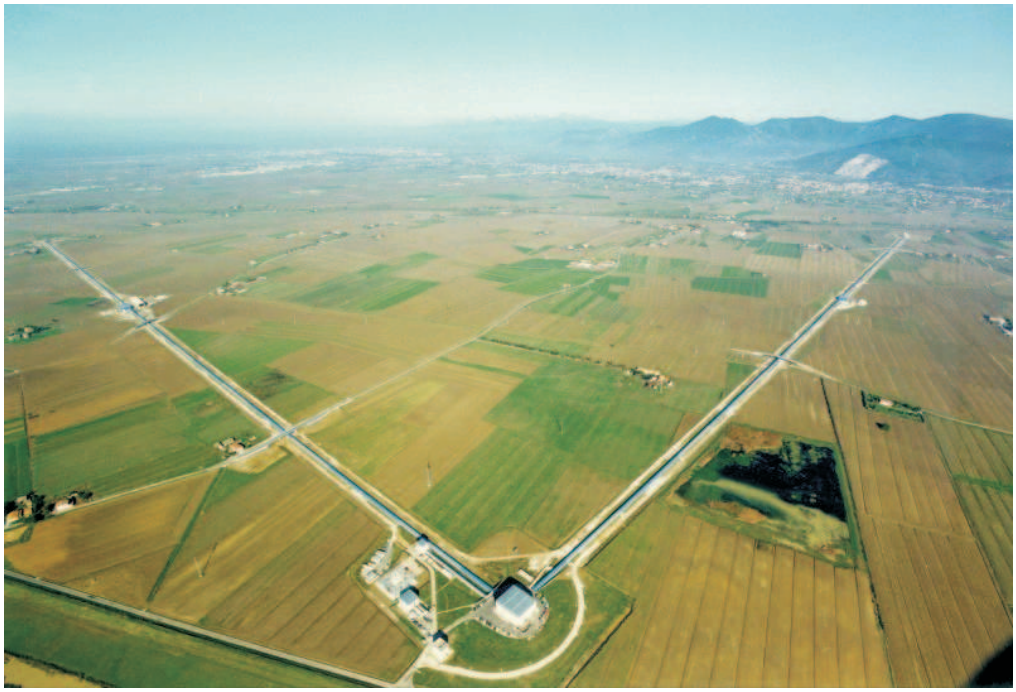

Figure 2.3: Virgo Experiment.

and GEO [16, 17, 18], are based on the same principle. In fig 2.4 is shown the Virgo design sensitivity with the limiting noise sources. The most relevant of them are: seismic noise up to 4 Hz, thermal noise up to 500 Hz and shot noise at higher frequencies.

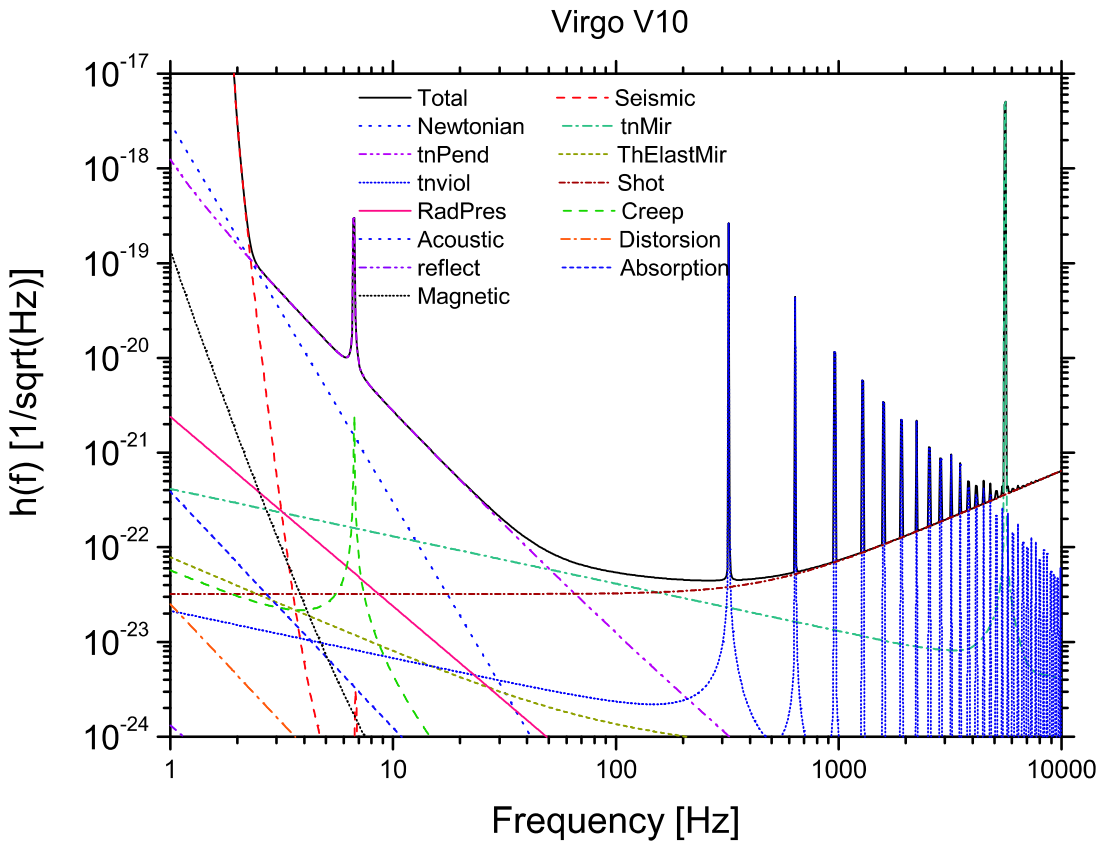

Figure 2.4: Virgo design sensitivity with the limiting noise sources.The most relevant of them are: seismic noise up to 4 Hz, thermal noise up to 500 Hz and shot noise at higher frequencies.

2.6.2 Optical layout

The optical layout of Virgo is shown in figure 2.5. The input laser is a 20 W (at 1064 nm) produced by a $Nd:YVO_4$ high power laser injection, locked to a 1 W Nd:YAG

master laser. A pockels cell is used to modulate the phase of the beam at 6.26 *MHz*. After the modulation the beam enters the vacuum system at the injection bench (IB), then, using a standard Pound-Drever-Hall (PDH) scheme [19, 20], is pre-stabilized by the mode-cleaner (IMC), a triangular Fabry-Perot cavity 144 m long and with Finesse 1000.

The low frequency prestabilization is performed by actively controlling the length of

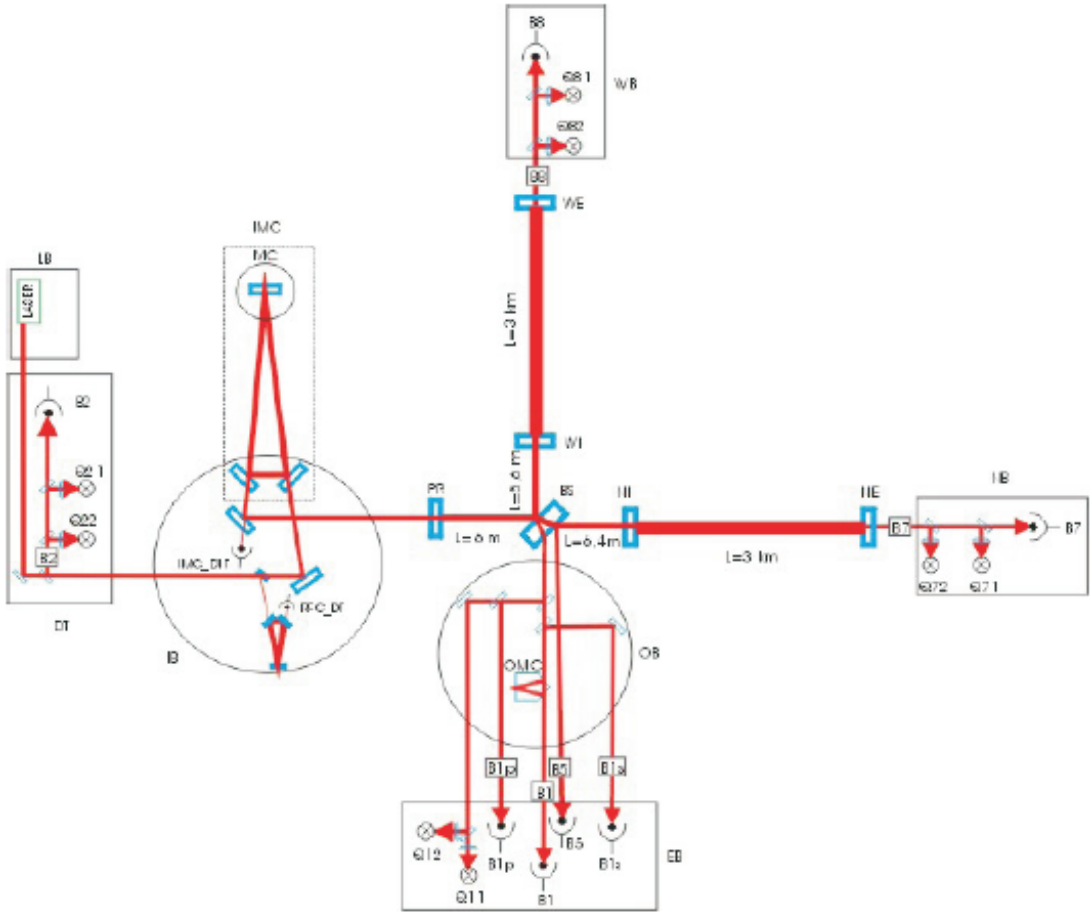

Figure 2.5: Virgo optical layout.

the IMC to lock the laser frequency to the length of a 30 cm monolithic triangular reference cavity (RFC) suspended in vacuum. The beam outgoing the injection system (10 W) enters the interferometer (ITF) through the power-recycling mirror (PR). The beam is split on the beam-splitter mirror (BS), and enters the two 3-Km long Fabry-Perot cavities. The PR mirror and the Michelson ITF form a Fabry-Perot cavity, the power recycling cavity (PRC). When the ITF is at its working point, the optical recycling gain of the PRC is about 50, which corresponds to a power of about 500 W on the the BS. Considering that the 3-Km Fabry-Perot cavities have a Finesse of 50 (which corresponds to an optical gain of about 32), the total power becomes about 8 kW. When the ITF is locked at its working point, the detection signal is extracted at the dark port. The beam is filtered by the output mode-cleaner (OMC), then is acquired by a set of 16 InGaAS photodiodes (B1), by which the dark port signal is reconstructed. Other signals are extracted from the ITF, essentially for control purposes.

2.6.3 Optics

The suspended optics of the Virgo interferometer are characterized by a large diameter (350 mm)and a great mass (20 Kg). The total losses at 1064 nm of each mirror (including absorption, scattering and large-scale wavefront deformation) should not exceed 100 parts per million (ppm). To minimize the noise on the interferometer output there are stringent limits on absorption ($< 5ppm$) and scattering ($< 5ppm$). For these reasons mirrors and beam splitters are super-polished pieces made of a new types of silica (Suprasil 311 SV, Suprasil 312 SV), with very low absorption and scattering, manufactured by the German company Heraeus, developed in collaboration with ESPCI (Paris). The OH content is very low ($<< 50ppm$), the refractive index is

homogeneous in all directions and the birefringence is very low ($< 5 \times 10^{-4} rad/cm$). The bulk absorption of the silica substrates crossed by the VIRGO laser beam has been measured [21] as being less than 0.7 *ppm/cm*. The flatness of these large components is 8 *nm* RMS on 150 *mm*. The limiting factor of the wavefront flatness is the substrate: since the polishers can not guarantee every time better wavefronts, the substrate surface is corrected before deposition by using a Corrective Coating technique [22]. The mirrors, after final coating with reflective quarter wavelength layers of SiO_2 and Ta_2O_5, exhibit a global RMS flatness of the order of 3 *nm* over 150 *mm*, an average absorption of less than 1 *ppm* and a scattering of the order of 5 *ppm*, thus being the most performing existing large optics.

2.6.4 Suspensions

The mirrors (test masses) of the interferometer are located in an ultra-high vacuum system (from 10^{-9} *mbar* for H_2 up to 10^{-14} *mbar* for hydrocarbon) and suspended by a sophisticated seismic isolation system the Superattenuator (SA), see fig. 2.6. The SA is a multistage multipendular suspension (10 *m* tall) which isolates the test masses from the ground motion. The reduction of the seismic noise is performed for frequency higher than a few *Hz* (the pendulum resonance frequency are all confined below a couple of *Hz*). The seismic attenuation system is either passive or active. The passive filtering is provided by the SA, a chain of mechanical filters.

The first stage of the SA [23] is an inverted pendulum (IP) preisolating stage [24]. A chain of five mechanical filters is suspended from the top of the IP. From the last stage of the chain (the so called "filter 7" [25]) an anvil shaped steel stage, the so called "marionette" [26], is suspended by a steel wire. Suspended to the marionette there is the payload system formed by the test mass and by an aluminum reference

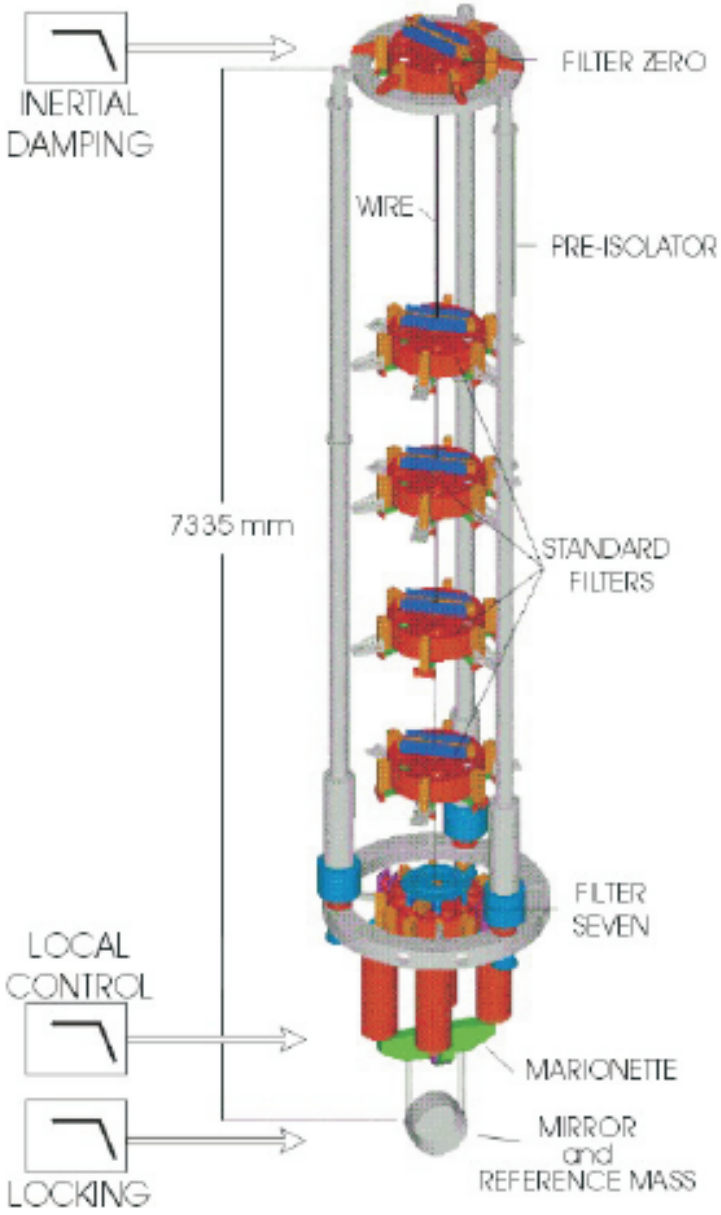

Figure 2.6: Scheme of the Virgo Superattenuator chain: in the CITF the feedback is exerted at three stages: inertial damping is performed at the inverted pendulum stage, local control through the marionette, and the interferometer locking keeping force acts on the mirror through the reference mass.

mass (RM), independently suspended behind the mirror. The passive attenuation of the whole chain is better than 10^{-14} at 10 Hz, corresponding to an expected residual mirror motion of $10^{-18} m/\sqrt{Hz}$ at the same frequency. The whole chain presents resonances, this bring to a residual low frequency motion of tens of microns at the frequency of the normal modes ranging between 40 mHz and 2 Hz with quality factors up to 10^3. To reduce these effects an active control is performed by exerting control forces on three actuation points: at the IP top stage level, performing an inertial active damping of the resonant motions of the SA [27]; using the marionette coils to steer the suspended mirror [26] with respect to the last stage of the chain; and directly on the mirror, through the coils supported by the RM which can act on four magnets mounted on the holder of the mirror. A local control system referred to the ground, is active in the bottom part of each SA in order to keep the longitudinal displacement of the mirrors below $1\mu m$ rms. It uses an optical lever to reconstruct the mirror motion. Two beams emitted by lasers placed on ground outside each tower enter into the tower through an optical window, one is reflected by a mirror placed on the marionetta and the other one by the suspended mirror itself. The reflected beams pass through a dedicated optical systems and reach PSD detectors. By using the PSD signals a feedback correction is performed to damp and control the local angular motion of the mirrors below $1\mu rad$ rms and makes the acquisition of the longitudinal lock of the interferometer possible with a limited actuation force, thus preventing noise reintroduction in the detection band. Since this system is referred to the ground, and therefore limited by the seismic noise, once the longitudinal locking of the interferometer is acquired the local control system is switched off and replaced by the automatic alignment system.

2.6.5 The commissioning of the interferometer

The interferometer locking

After the pre-alignment, the interferometer need to be locked at its working point. This means that the laser beam is in resonance with the Fabry-Perot and recycling cavities and the main output port is on the dark fringe. These conditions can be achieved by fixing relationships between the laser wavelength and four independent lengths of the interferometer: the recycling cavity length, the differential length of the short Michelson arms, the common and differential length of the two long arms (see [28, 29] for the exact definition). These four lengths have to be controlled with a very high accuracy (typical rms of $10^{-12} - 10^{-10}$ m). The longitudinal control is performed by using the Pound-Drever-Hall technique, being the input beam modulated at 6.26 *MHz*. All the four lengths can be reconstructed by mixing the signals coming from photodiodes placed at different output ports of the interferometer. The photodiode signals are digitized and sent via optical links to the global control system [30] that computes at a 10 *kHz* sampling rate the correction signals to be sent to the reference mass coils, converted to an analog signal by the DAC of the suspension electronics.

Mirror Suspension Control

A digital active control of the inverted pendulum top stage (inertial damping) is implemented to damp the SA normal modes [27]. The mirror velocity is reduced down to a few tenths of μm per second. This residual swing is small enough to allow a straightforward locking acquisition. In addition, this active swing reduction makes smaller the compensation force to be applied at the mirror level to maintain the interferometer locked. This allows to reduce the electronic noise induced by

the DAC reference mass coil in the VIRGO band. Indeed this noise is proportional to the range of the force made available at the mirror level. For the same reason the large (hundreds of microns) drifts of the mirror (between DC and a few tens of mHz) are compensated by acting to the suspension top stage (Tidal control). The induced control DAC noise at the top stage is filtered by the suspension chain below. Once the tidal control is implemented, the mirror residual displacement is around 1 μm peak to peak and occurs mainly between tens of mHz and a few Hz. This displacement is compensated acting to the marionette so that the DAC noise is filtered by the mirror pendulum below. Using this hierarchical control, only nanometer displacements (above a few Hz) are compensated by acting directly to the mirror level (from the reference mass coils). The reduction of the reference mass force range makes the DAC noise in the VIRGO band smaller than the other noise mechanisms limiting the antenna sensitivity.

The Automatic Alignment

Once the interferometer is longitudinally locked it is necessary to maintain the mirrors aligned each other and with respect to the incoming beam. The required accuracy (rms close to 10^{-9} rad), not achievable by the ground-based mirror LC, can be reached by the Anderson-Giordano technique [31]. The laser phase-modulation frequency is chosen so that the sidebands of the first order optical transverse mode (TEM01) are resonant in the arm cavities. The light transmitted by the cavities is detected by quadrant photodiodes and signals proportional to the mirror misalignments are generated. The error signals are received by the global control that computes the feedback correction signals sent to the marionette coil-magnet actuators. This is done with a control bandwidth of a few Hz in order to avoid the

injection of noise in the VIRGO band [32].

2.6.6 Status of Virgo

All the VIRGO subsystems were already tested in 2001-2002, during the commissioning of the *Central Interferometer* [33]. This was a 6m-long recycled Michelson interferometer made by the injection system, the beam splitter, the recycling mirror and the two cavity input mirrors (used, in this case, as end mirrors). The optical components were suspended to the same suspensions used in VIRGO. Also the other components were nearly identical to the ones used in the final apparatus.

The VIRGO commissioning started on September 2003, after the completion of the 3-km long arms, with the locking and the characterization of the single Fabry-Perot cavities. In February 2004 the interferometer was locked for the first time in the recombined mode. This means to have the two long cavities locked at the resonance (by acting on the end mirrors), the Michelson locked on the dark fringe (by controlling the BS position) and the PR still misaligned. The automatic alignment was implemented in this configuration in the Spring 2004. In October 2004 the locking of the entire recycled interferometer was acquired for the first time by using the variable finesse technique described in [29].

Seven commissioning runs have been performed so far. The corresponding configurations are reported here below, while the sensitivity curves are displayed in Fig. 2.7.

- C1 (14-17 Nov. 2003): North cavity locked at resonance.
- C2 (20-23 Feb. 2004): North cavity locked at resonance plus automatic alignment.

- C3 (26-27 Apr. 2004): C2 with frequency stabilization servo (23-26 Apr. 2004) and recombined interferometer.

- C4 (24-29 Jun. 2004): Recombined interferometer with automatic alignment, frequency stabilization servo and tidal control.

- C5 (2-7 Dec. 2004): As in C4 with suspension hierarchical control and first data taking with recycled interferometer.

- C6 (29 Jul. -12 Aug. 2005): ITF locked in recycling mode with partially automatic alignment.

- C7 (14-19 Sep. 2005): As in C6, with DAC noise reduction, tidal control on BS, BS coil drivers in low noise configuration, new control of PR mirror, increased modulation depth, and complete automatic alignment.

The data acquisition chain was successfully tested during the commissioning runs. The current data rate is 7 *Mbytes/s* of compressed data. Six data analysis groups (settled up inside VIRGO since 1998) are focused to the reconstruction of the gravitational wave signal from the interferometer channels, to characterize the noise in the apparatus, to detect coalescing binaries [34], bursts [35], periodic sources and stochastic background. The cyan curve in fig. 2.7 concerns the best sensitivity curve ever achieved. The improvement in C7 with respect to C6 is ascribed to the automatic alignment (up to about 30 *Hz*), to the reduction of the beam splitter control noise and of the DAC noise (up to about 200 *Hz*), to the improvement in the PR mirror control (up to about 500 *Hz*) and to some photodiode read-out configuration change (in the high frequency range). In addition to the sensitivity curve measurements, C6 (15 days long) has shown that the interferometer can be

operated in science mode for a long term (maximum lock of 40 hours) with a good duty cycle (about 90%), and C7 run has demonstrated the full functioning of all the components, systems and control loops of the interferometer.

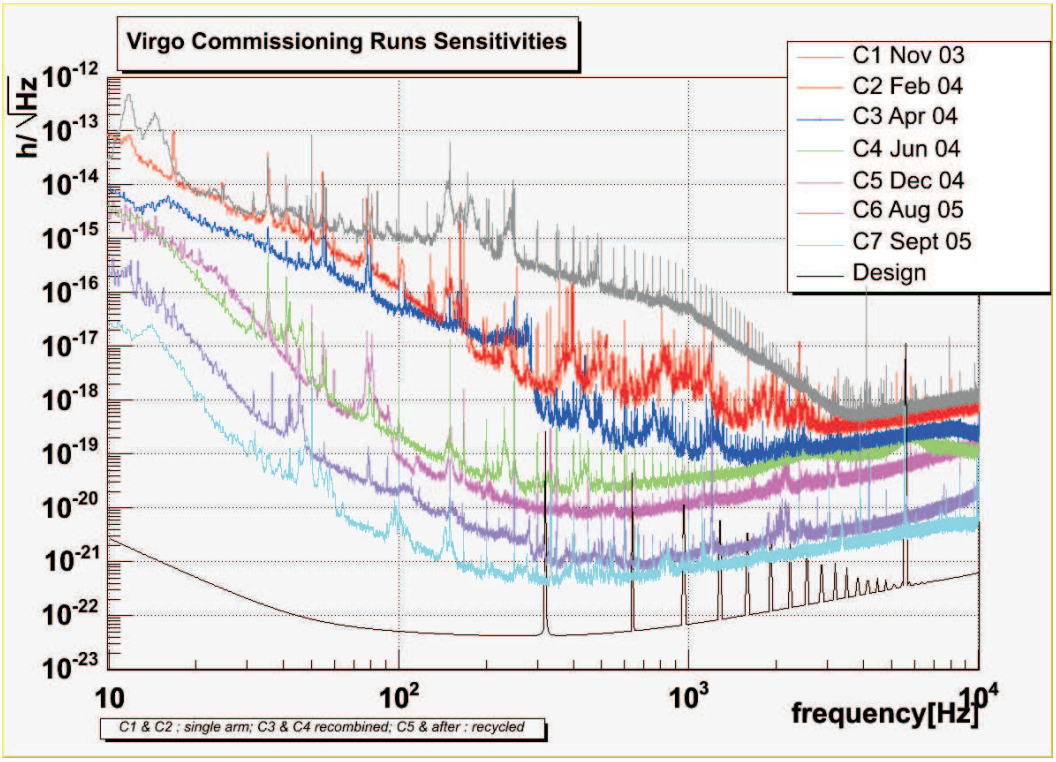

Figure 2.7: VIRGO sensitivity curves in the different runs compared with the designed one.

Chapter 3

Adaptive Optics

3.1 Introduction

The Adaptive Optics (AO) is a technique for the real-time correction of aberrations of light beams [36, 37]. Aberrations are imperfections that blur the image that is formed by an optical system. For example, these aberration can arise when light from astronomical objects travels through the Earth's atmosphere, when light passes through fluid like the human eye, when an optical system is not well aligned or its optics are aberrated themselves. An AO system consist of two main parts, the wavefront sensor which measures the aberrations of the beam, and the actuator which corrects these beam aberrations.

In fig. 3.1 is drawn the general scheme of an AO system. A generic beam of light (light coming from celestial objects or lasers for example) is perturbed by some external source of noise (atmospheric perturbation for example), a portion of the beam is taken and analyzed by a wavefront sensor, the informations acquired on beam distortions are then computed and correction signals are generated and sent to the actuator which corrects the main beam.

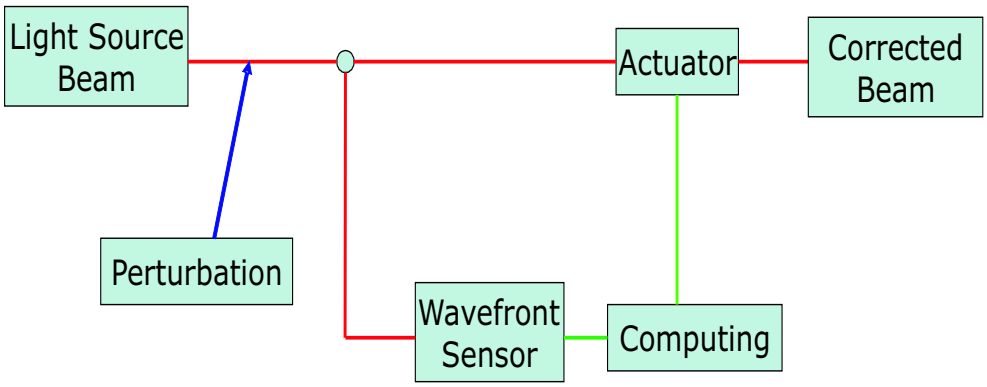

Figure 3.1: An Adaptive Optics system consist of two main parts, the wavefront sensor which measures the aberrations of the beam, and an actuator which corrects these beam aberrations.

3.2 Wavefront sensing

Several wavefront sensors technique (WFS) have been developed, the most used of them are: Shack-Hartmann, curvature sensor, pyramid sensor, phase-diversity and sharing interferometer [38, 39, 40, 41].

Shack-Hartmann technique- The beam to analyze is sent to an array of small identical lenses (fig. 3.2). Each lens takes a small part of the beam and focus it (producing a spot) on a detector (typically a CCD). All the spots are formed on the same detector. When an incoming wave-front is plane, all the spots are located in a regular grid defined by the lens array geometry. If the wave-front is distorted, the spots displace from their nominal positions. Displacements of the spots (or image centroids) in two orthogonal directions x-y are proportional to the average wave-front slopes in x-y over the lens sub-apertures. By measuring the displacements of the different spots it is possible to reconstruct the total wave-front slope up to a constant which is of no importance for imaging.

Curvature sensor- The beam to analyze is focused by a lens (fig. 3.3). The

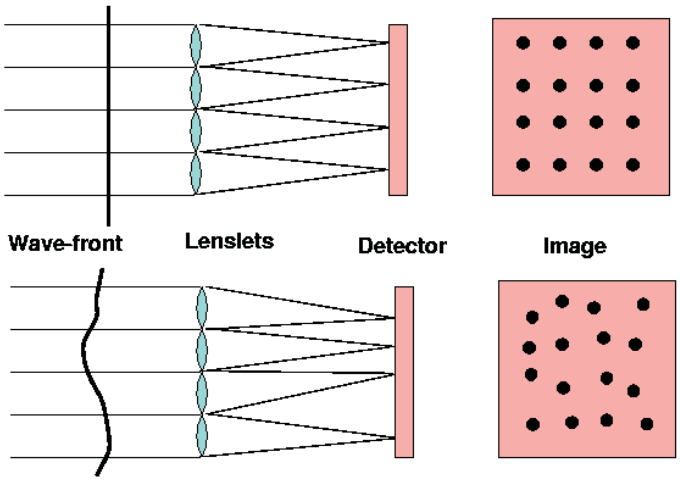

Figure 3.2: Shack-Hartmann wavefront sensor.

intensity distribution is measured in two planes, at a distance l before and after the the image plane. If the wave-front is distorted the intensity distribution in the two planes is different, from these intensity differences can be reconstructed the wavefront slope. Another technique similar to the curvature sensor is the phase diversity technique. The main difference is that the in the case of curvature sensor

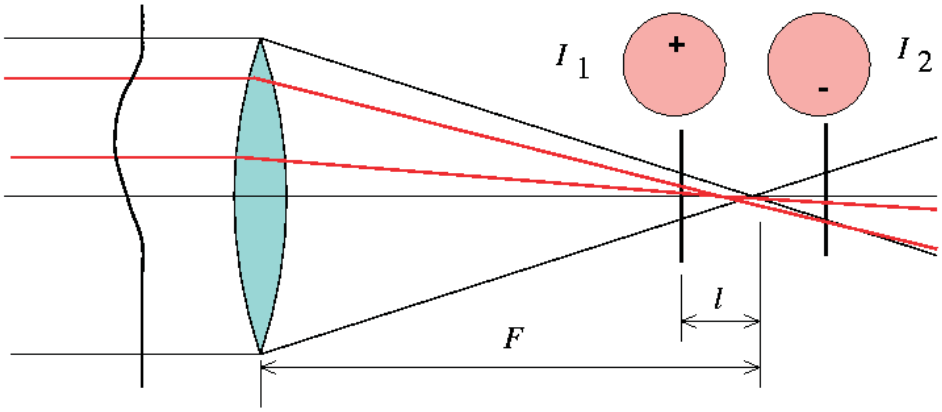

Figure 3.3: Curvature sensor.

the two images are taken symmetrically about the pupil plane, while in the case of phase diversity the two images are taken symmetrically about the image plane.

Pyramid sensor- The beam is focused on a transparent pyramid (fig. 3.4), which divides the image into four parts. The four beams are deflected forming four images on the same CCD detector. Thus, each sub-aperture is detected by 4 CCD pixels. A wave-front slope at some sub-aperture changes the source position on the pyramid, hence changes the light power detected by the 4 pixels which would otherwise be equal. By computing the normalized intensity differences it is possible to get two signals proportional to the wave-front slopes in two directions.

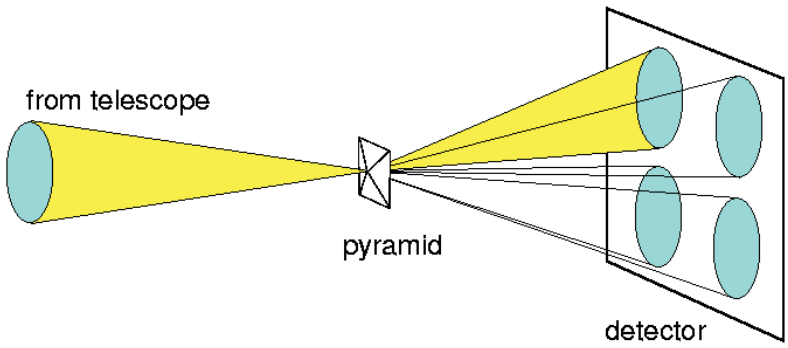

Figure 3.4: Pyramid sensor.

Shearing interferometer- In the common optics the technique used to measure wavefront distortions typically is the interferometry. There are three main reasons for which the interferometry has not been a lot applied in the AO techniques. Especially, considering that the AO has been developed early for astronomical applications (and now is still the major field of application). First, an astronomical AO system analyzes the light of stars passing through the turbulent atmosphere, hence use incoherent (and sometimes non-point) sources. Even the laser guide stars are not

coherent enough to work in typical interferometers. Wavefront sensors must work on white-light incoherent sources. Second, the interference fringes are chromatic. It is not possible to filter the stellar light, because we need to sense faint stars, so wavefront sensors must use the photons very efficiently. Third, interferometers have an intrinsic phase ambiguity of 2π, whereas atmospheric phase distortions typically exceed 2π. The WFS must be linear over the full range of atmospheric distortions. There are algorithms to un-wrap the phase and to remove this ambiguity, but they are slow, while atmospheric turbulence evolves fast, so wavefront sensors must be fast.

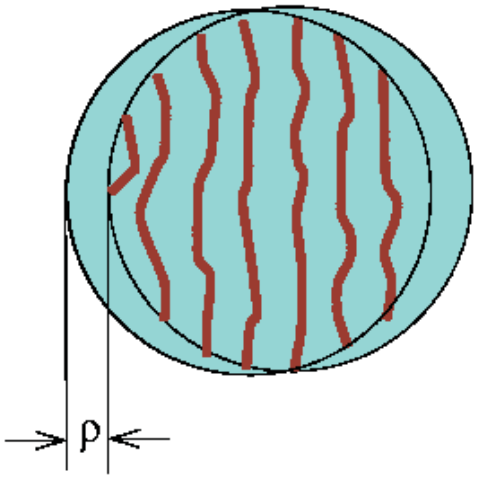

Figure 3.5: Shearing interferometer.

The problems of interferometric wave-front measurement can be overcome when the interfering beams represent wave-fronts with a small lateral shift ρ (this is called shearing interferometer). If the shear is less than r_0 (r_0 is a parameter proportional to the wavelength), the phase differences are less than one wavelength, and there is no 2π ambiguity. The interference pattern intensity is proportional to the first

derivative of the phase difference (for small shifts), hence the signal of a shearing interferometer is similar to that of a Shack-Hartmann sensor.

3.3 Wavefront control

The typical actuators used in AO to control wavefront aberrations are deformable mirrors. The technology in building such mirrors has know a great progress in last years bringing to the development of various kind of deformable mirrors. Early deformable mirrors (segmented mirrors) consisted of discreet segments, each controlled by 3 piezoelectric actuators. Nowadays, the typically used mirrors consist of a continue reflecting surface deformed by using different technology. In particular, the most developed are: micromachined membrane deformable mirror (MMDM), piezoelectric deformable mirror (PZT) and bimorph mirror (BM) [42].

In fig. 3.6 is shown the scheme of a typical MMDM mirror (produced by OKOtech).

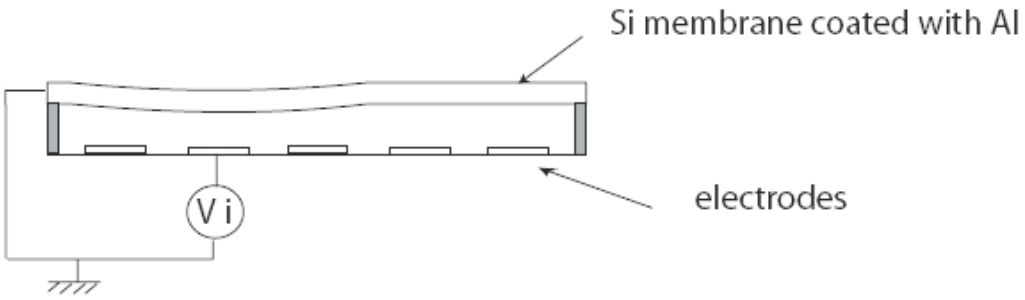

Figure 3.6: Scheme of micromachined membrane deformable mirror (OKOtech).

It consists of a silicon nitride membrane suspended over an array of electrodes. The 37 electrodes, hexagonally arranged, enable to locally deform the membrane. The membrane is electrostatically attracted toward the electrodes when a voltage is

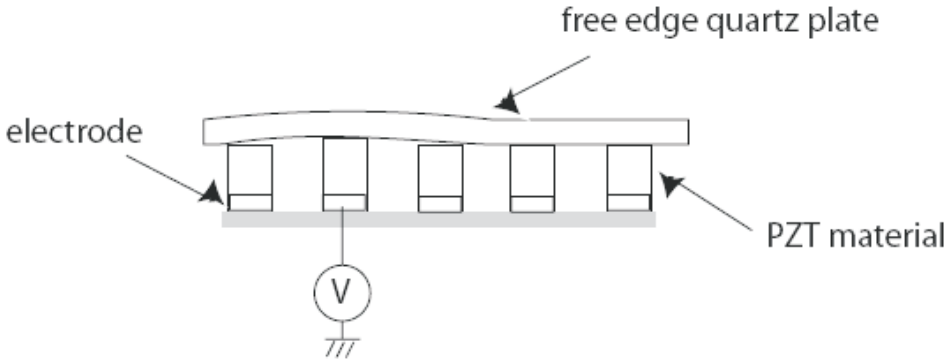

Figure 3.7: Scheme of piezoelectric deformable mirror (OKOtech).

applied to them. In fig 3.7 is shown the scheme of a PZT mirror (produced by OKOtech). It consist of a reflective quartz plate which has free edge and is piston-like deformed by the lead zirconium titanate actuators when a voltage is applied. Finally, in fig. 3.8 is shown the scheme of a BM mirror (produced by AOptics). It consist of two layers of ceramic lead magnesium niobate (PMN) which are directly actuated by the electrodes bonded on the materials. When an electric field is applied to PMN material it deforms independently of the polarity of the field.

Moreover, we must remark another recent technology to control the wavefront of light which consists in using liquid crystals (LC). There are two basic types of liquid crystals used as phase modulators: Nematic LC and ferroelectric LC. Nematic LC (are the most common used) are optically equivalent to a linear waveplate whose optical axis is fixed, but whose birefringence is a function of the applied voltage. When the applied voltage varies the birefringence changes, resulting in a change of the optical path length for a linearly polarized beam propagating parallel to the extraordinary axis. The ferroelectric LC are optically equivalent to a linear wave-plate whose retardance is fixed, but whose optical axis is a function of the applied

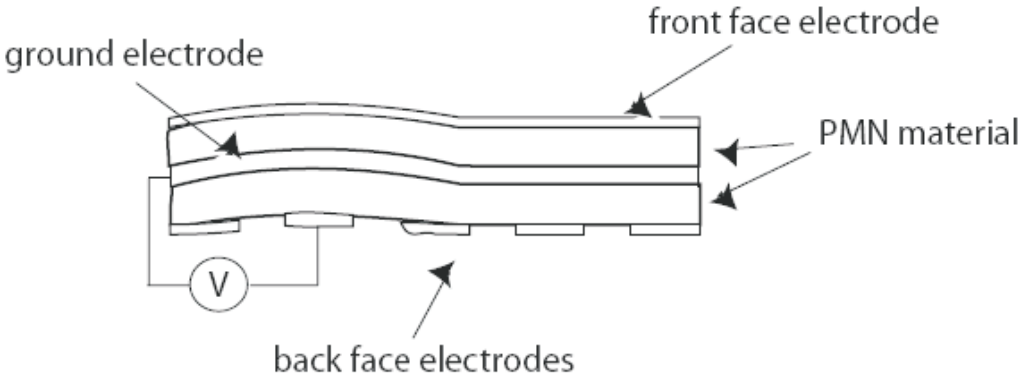

Figure 3.8: Scheme of bimorph mirror (AOptics).

voltage. Phase modulation is more complicated with a ferroelectric LC than with a nematic device. Typically is achieved by placing LC, with a retardance of half a wave, between two co-aligned fixed quarter-wave plates. Applying a voltage to the LC it rotates and the incident light is phase shifted by twice the angle of rotation.

3.4 Adaptive Optics applications

Adaptive Optics has been developed in the framework of both the astronomical and military communities. Nowadays the AO techniques are used in several fields of application, the most important of them are: astronomy, ophthalmology and vision science, free space optical communications, laser beam shaping, industry, defense.
AO is typically applied in astronomy to correct the blurring of the telescopes images due to the turbulence of the atmosphere which distorts the wavefront of the light coming from astronomical objects. For example, the resolution at infrared wavelengths of an 8-10 m telescope (like the VLT or Keck) without AO correction is of the order of *1 arcsec*. By using an AO correction system the resolution can be stressed up to *30-60 milliarcsec*. Considering that a science target is often too faint

to be used as a reference star a nearby brighter guide star can be used instead. The light from the science target passes through approximately the same atmospheric turbulence as the reference star light and so its image can also be corrected.
The necessity of a nearby reference star of sufficient luminosity severely limits the application of this technique for astronomical observations. To overcome these problems it can be used a laser guide star (LGS), that is a laser beam which generates an appropriated target in the atmosphere, it can then be used as a wavefront reference in the same way as a natural guide star. Another technique recently developed is the multi-conjugated adaptive optics. Essentially, it is based on the use of several deformable mirrors and wavefront sensors optically matched to different altitudes so to build a three-dimensional picture of the wavefront distortions.
In recent years they have been developed several instruments based on Adaptive Optics for ophthalmology and vision science. For example the Adaptive Optics has been implemented in the confocal scanning laser ophthalmoscopes used for imaging the retina. The resolution of these instruments can be improved by implementing AO systems to reduce the aberrations in the cornea and lens of the eye. This improvement allows to study the fine structure of the eye. In the same way the performances of the Optical Coherence Tomography technique, which allows to achieve a fine depth resolution within the retina, can be improved by AO corrections in order to reach a fine spatial resolution. Moreover, studies with adaptive-optics corrected instruments suggest that even sharper resolution can be obtained by correcting higher-order aberrations in the eye. Adaptive optics systems offer the possibility of accurately measuring high-order aberrations in individuals and customizing the correction to each person. Methods for implementing this are currently under study(customized contact lenses, intraocular lenses, or customized laser refractive

surgery).

Another application of AO is in the field of free-space optical communications. This technique uses laser telemetry to communicate through air between two optical fiber networks. Their main shortcomings are in dealing with variable atmospheric conditions. Current systems deal with these issues by broadening the beam size, and hence having to increase the laser power and suffer the corresponding reduction in transmission range. Adaptive optics offers the potential for overcoming these limitations by adaptive tracking of the beam and correction of atmospherically-induced aberrations.

The AO techniques are also used for laser shaping to improve the beam collimation and reduce the geometrical aberrations. The beam shaping can be used in applications like intracavity beam corrections, laser micromachining, high power laser for cutting and welding, low-power compact systems for optical storage devices. Finally, AO can be used in defense to improve the performances of target tracking systems and satellite communications.

Chapter 4

Adaptive optics system for the correction of aberrations of input laser beam in gravitational wave interferometers

4.1 Introduction

In previous chapters we saw the fundamental noises which limit the sensitivity of Virgo interferometer. To reach such extreme sensitivity other kinds of noises must be suppressed; among them, there is the noise generated by the coupling between the interferometer asymmetries and the geometrical fluctuations of the input laser beam. The interferometer asymmetries can be considered as different fundamental modes of the cavities in each arm. In fact, the fundamental mode of each arm can be represented as the sum of the fundamental Hermite-Gauss mode TEM_{00} and higher order modes TEM_{mn} of an ideal cavity. In the same way, the geometrical fluctuations of the input beam can be represented as fluctuations of higher order modes of a pure TEM_{00} beam perfectly matched to an ideal interferometer. In this analysis we consider only higher order modes up to second order, because, at this level, modes of order higher than two can be neglected. As we will see below,

the interferometer asymmetries corresponding to higher order modes couple to the geometrical fluctuations of input laser beam corresponding to the same modes, generating a phase-noise. If the geometrical fluctuations of the laser are not reduced, the resulting noise imposes very stringent limits to the tolerated interferometer asymmetries.

Presently, in Virgo, the reduction of geometrical fluctuations of the input laser beam is performed passively by the mode-cleaner, a triangular Fabry-Perot cavity with Finesse 1000 used in transmission. The geometrical fluctuations are seen by the cavity as higher order modes which are not resonant and then are reflected back. The noise reduction is of the order of the cavity Finesse. Despite the use of mode-cleaner, the residual fluctuations impose very stringent limit to the tolerated asymmetries. In this contest, an adaptive optics system could be used in cascade with the commonly used passive mode-cleaner cavity, to have an active control. In particular AO could be used to correct the expected thermally induced aberrations in the next generation high power interferometers, so to assure suitable beam matching with mode-cleaner [43, 44], as well as to perform a pre-mode-cleaning fast correction so to add a safety factor to the mode-cleaner performances [45, 46, 47]. For example, the thermal effects, especially for second generation interferometers where laser power of about 200 W are expected to be used, are known to greatly reduce the power coupled with the passive cavity (about 90% of power lost). This can be due to distortion caused by absorbing media in intermediate optics, like for example the Faraday isolator; a compensation can be obtained using negative expansion coefficient materials [48], but residual aberrations, of the order of 10% on low order Gaussian modes, impose a further reduction with 40 db gain at low frequency, in order to lower the power lost into higher order modes under the 1%.

4.2 Effects of coupling between the interferometer asymmetries and the input beam jitters

In this paragraph, we consider which are the effects of the coupling between the interferometer asymmetries and the geometrical fluctuations of input laser beam, also called beam jitters [45, 47, 49].

Consider a recycled Fabry-Perot Michelson interferometer (fig. 4.1). We can consider small misalignments of a cavity as perturbations to the fundamental mode (for simplicity we are in the waist plane) [31]. if we fix the position of the recycling mirror the asymmetries of whole interferometer depend by the asymmetries of the cavities.

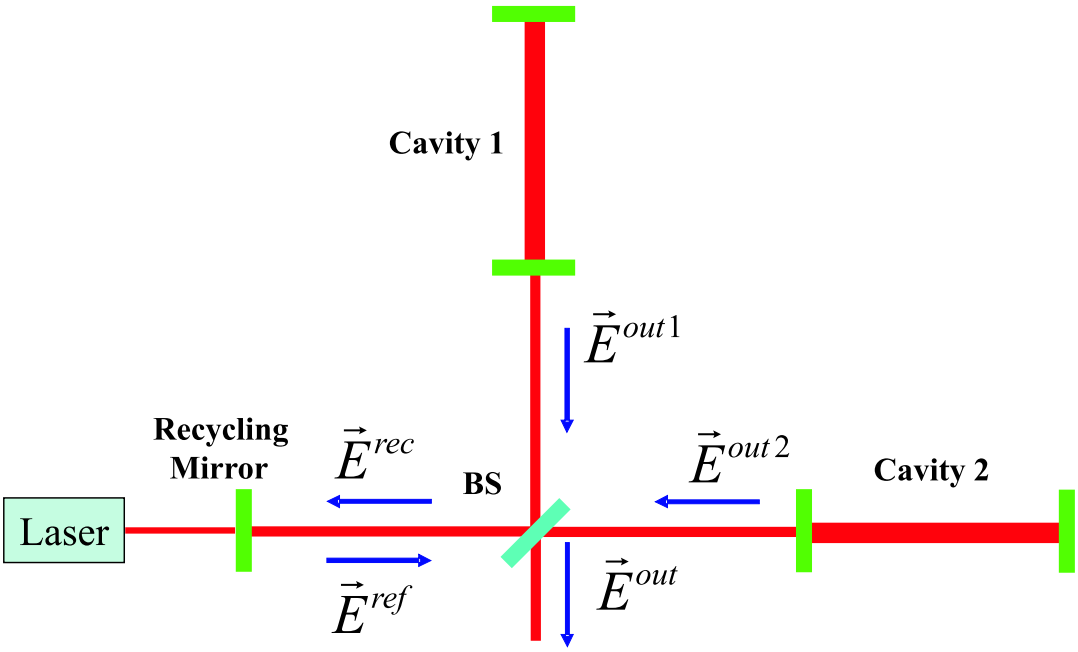

Figure 4.1: Recycled Fabry-Perot Michelson interferometer.

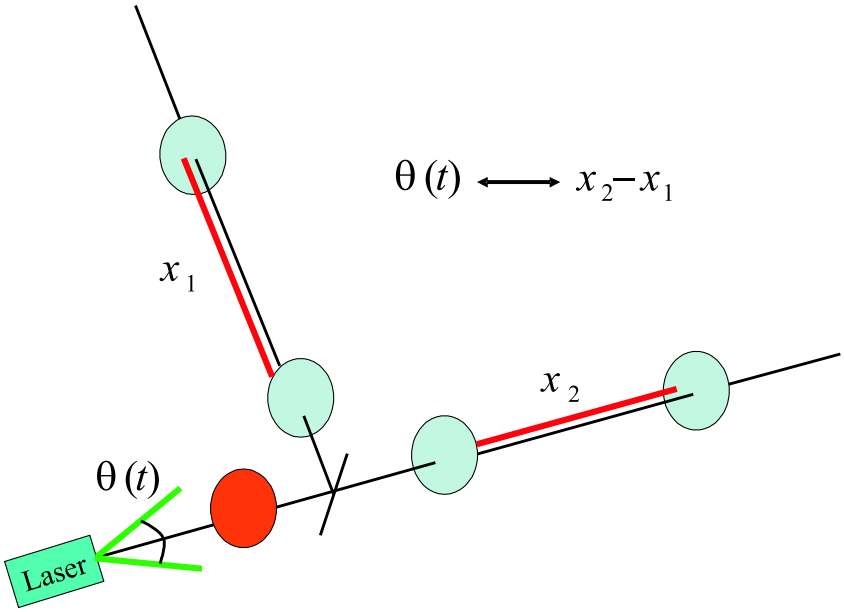

Figure 4.2: Example of coupling between the geometrical fluctuations of input beam and cavities asymmetry. The optical axis of the two cavities are translated by x_1 and x_2 respect to the interferometer axis and the direction of input beam oscillates with an angle $\theta(t)$ and a frequency ω in the interferometer plane.

For example we consider a simple case (see fig 4.2). The optical axis of the two cavities are translated by x_1 and x_2 respect to interferometer axis and the direction of input beam oscillates with an angle $\theta(t)$ and a frequency ω in the interferometer plane. The fundamental modes of the cavities Ψ_1^0 and Ψ_2^0 can be written at first order as:

$$\Psi_{1,2}^0 \approx \Psi^0 + \epsilon_{1,2}\Psi^1 \tag{4.1}$$

where $\epsilon_{1,2}^t = x_{1,2}/w_0$ and Ψ^m are the usual Hermite-Gauss modes [50, 51].

The input beam can be written at first order as:

$$\mathbf{E}^{in} \approx A[\Psi^0 + \beta(t)\Psi^1]\exp(i\omega_0 t) \tag{4.2}$$

where $\beta(t) = i\theta(t)(\pi w_0/\lambda)$. If we impose $\beta(t) = \frac{1}{2}\beta_0(e^{i\omega t} + e^{-i\omega t})$, with $\beta_0 = i\theta_0(\pi w_0/\lambda)$, the incident field can be written as the sum of two fields with components at different frequencies:

$E^0 = A\Psi^0 \exp(i\omega_0 t)$ having components in Ψ^0 mode, with frequency ω_0;

$E^1 = A\Psi^1 i(\beta_0/2) \exp[i(\omega_0 \pm \omega)t]$ having components in Ψ^1 mode, with frequencies $\omega_0 \pm \omega$.

The misalignment of the interferometer mixes up these modes, so its internal field E^{rec}, at frequencies $\omega_0 \pm \omega$, can be written as:

$$\mathbf{E}^{rec}(\omega_0 + \omega) = M(\omega_0 + \omega)\mathbf{E}^{in}(\omega_0 + \omega) \tag{4.3}$$

where $\mathbf{E}(\omega)$ is a two-element vector having as components the projections of the electric field onto Ψ^0 and Ψ^1modes. The matrix M, taking into account only the first-order terms in the misalignments, can be calculated as a sum of all the reflections of the beam going forth and back in the interferometer.

In the more general case the electric field circulating in the recycling cavity can be obtained by superposing the incident fields transformed by the matrix M:

$$E^{rec} = [M(\omega_0)(1;0) + M(\omega_0 \pm \omega)(0;\frac{1}{2}i\beta_0)e^{\pm i\omega t}]Ae^{i\omega_0 t} \tag{4.4}$$

From eq. 4.4 we can obtain the two fields outgoing the cavities:

$$E_1^{out} = \frac{1}{2}(\langle \mathbf{E}^{rec}|\Psi_1^0\rangle \hat{r}_1^0 \Psi_1^0 + \langle \mathbf{E}^{rec}|\Psi_1^1\rangle \hat{r}_1^1 \Psi_1^1) \tag{4.5}$$

$$E_2^{out} = \frac{1}{2}(\langle \mathbf{E}^{rec}|\Psi_2^0\rangle \hat{r}_2^0 \Psi_2^0 + \langle \mathbf{E}^{rec}|\Psi_2^1\rangle \hat{r}_2^1 \Psi_2^1) \tag{4.6}$$

and their phase-difference:

$$\delta\psi = Re\left((\epsilon_1 - \epsilon_2)\beta_0 \frac{r_1 + r_0 f(\omega)e^{i\varphi}}{r_0} \frac{1 - r_0 r_R}{1 + r_1 r_R}\right) \tag{4.7}$$

From eq. 4.7 we note that the phase-difference between the two beams is proportional to the term of angular fluctuation of the input beam β_0 and to the term $(\epsilon_1 - \epsilon_2)$ which expresses the difference (and then the asymmetry) between the translations of the two cavity optical axis to respect the interferometer axis. If the interferometer is symmetric, that is if the cavity axis are translated by the same amount to respect the interferometer axis, we have $\epsilon_1 = \epsilon_2$, then a null effect.

In the same way, translation fluctuations of the input beam couple with asymmetry in angular tilt of cavity axis respect to the interferometer axis. At the second order there are the following couplings: fluctuations of input beam waist diameter and asymmetry in waist positions of the two cavities; fluctuations of input beam position and asymmetry of waist diameter of the two cavities; fluctuations in difference of waist diameter (along x-y axis) of input beam and asymmetry in difference of waist position along x-y axis (and along the 45° rotated x'-y' reference system) of the two cavities; fluctuations in difference of waist position along x-y axis (and along the 45° rotated x'-y' reference system) of the input beam and asymmetry in difference of waist diameter (along x-y axis) of the two cavities.

Therefore, in general way, the laser beam before the mode-cleaner can fluctuate in translation $\delta x(t)$, in angle $\delta\theta(t)$, in waist dimension $\delta w(t)$, in waist position $\delta z(t)$ (defocusing terms), in difference of waist dimensions and waist position along x-y axis and along the 45° rotated x'-y' reference system respectively indicated as $\delta w(t)_{A90}$, $\delta z(t)_{A90}$, $\delta w(t)_{A45}$, $\delta z(t)_{A45}$, which correspond to the astigmatisms in the classical theory of aberrations [52]. If the fluctuations (or jitters) are sufficiently small, they can be described as perturbations to the fundamental Gaussian mode by higher order modes:

$$\Psi_{in} \cong \Psi_{00} + \left[\frac{\delta x(t)}{w_0} + i\frac{\pi w_0 \delta\theta_y(t)}{\lambda}\right]\Psi_{10} + \left[\frac{\delta y(t)}{w_0} + i\frac{\pi w_0 \delta\theta_x(t)}{\lambda}\right]\Psi_{01} +$$

$$+ \left[\frac{\delta w(t)}{w_0} + i\frac{\delta\lambda z(t)}{2\pi w_0^2}\right]\frac{1}{\sqrt{2}}(\Psi_{20} + \Psi_{02}) + \left[\frac{\delta w(t)_{A90}}{w_0} + i\frac{\delta\lambda z(t)_{A90}}{2\pi w_0^2}\right]\frac{1}{\sqrt{2}}(\Psi_{20} - \Psi_{02}) +$$

$$+ \left[\frac{\delta w(t)_{A45}}{w_0} + i\frac{\delta\lambda z(t)_{A45}}{2\pi w_0^2}\right]\Psi_{11} \tag{4.8}$$

Where Ψ_{mn} are the standard Hermite-Gauss modes. The above expression can be written in a more compact form:

$$\Psi_{in} \cong \Psi_{00} + A_x\Psi_{10} + A_y\Psi_{01} + A_{def}\frac{1}{\sqrt{2}}(\Psi_{20} + \Psi_{02}) +$$

$$+ A_{A90}\frac{1}{\sqrt{2}}(\Psi_{20} - \Psi_{02}) + A_{A45}\Psi_{11} \tag{4.9}$$

As we saw, the coupling coefficients are the products of the coefficients $\tilde{A}_{mn}$ times the static coefficients of asymmetries. Considering that the typical values for asymmetry coefficients are about 10^{-3} and that the shot-noise limited phase sensitivity of Virgo is about $10^{-11} rad/\sqrt{Hz}$ we obtain the constrain $\tilde{A}_{mn} < 10^{-8}\frac{1}{\sqrt{Hz}}$ at the input of the interferometer. If we take into account that the modes suppression factor of the mode-cleaner is about 10^{-3}, the requirements before the mode-cleaner become $\tilde{A}_{mn} < 10^{-5}\frac{1}{\sqrt{Hz}}$. This means that the eventually jitters noise reintroduced by the AO system before the mode-cleaner must satisfy: $\tilde{A}_{mn} < 10^{-5}\frac{1}{\sqrt{Hz}}$.

4.3 Implementation of an Adaptive Optics system in gravitational wave interferometers

In Fig. 4.3 is shown a possible implementation of an AO system in a gravitational wave interferometer. The system consists of two deformable mirrors acting on the beam before the mode-cleaner. As error signal for the feed-back can be used the beam reflected by the mode-cleaner which contains all the higher order modes reflected back. A pixellated photodiode is used to sense the different components of higher order modes using the classical Ward technique [53].

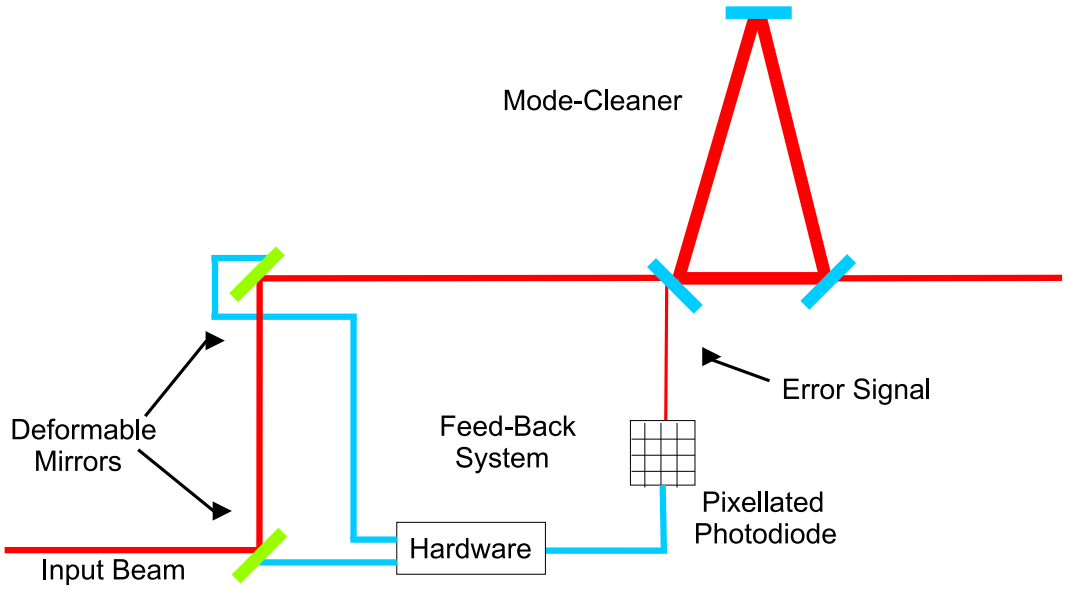

Figure 4.3: Scheme showing a possible implementation of AO system in gravitational wave interferometer.

If used for mode matching the system should be capable to correct fluctuations with gain of the order of 40 dB at low frequency (less than 1 Hz). Moreover, the upper limits on reintroduced noise must be of the order of $\tilde{A}_{mn} < 10^{-5}\frac{1}{\sqrt{Hz}}$ in the gravita-

tional wave measurement band extending from 10 *Hz* to 10 *kHz*.

Otherwise, if used in high frequency bandwidth, the unity gain of the loop should be above some tens of *Hz*, with the same constraint of $\tilde{A}_{mn} < 10^{-5}\frac{1}{\sqrt{Hz}}$ for reintroduced noise at higher frequency: as an example the Virgo interferometer presently uses an Automatic Beam Positioner (ABP) to correct beam tilts with a bandwidth up to 40 *Hz* [54].

Various actuators for the correction of wavefront have been proposed: systems based on thermal deformation of mirrors or lenses as well as systems based on deformable mirrors. While thermally based corrections have been proved to be useful and efficient [55], in this work it has been investigated an AO system based on deformable mirrors because it warrants a much simpler optical scheme, avoids the use of auxiliary high power lasers and preserves the possibility to use the system also to correct fluctuations at higher frequency, as it could be useful in next generation interferometers.

It is important to point out that the application of Adaptive Optics to the gravitational wave interferometer is enough different from the typical applications, as for example Astronomy. First we need to correct very small aberrations of an high quality laser beam which is already very cleaned up (in particular there are not 2π ambiguities). Second we need to correct only low order aberrations, up to second order in Hermite-Gauss modes, and relatively high bandwidth. Third we have much light power to use for the sensing, so we have less problems of saving photons. Motivated by these considerations it has been developed an AO system based on interferometric detection of wavefront aberrations.

4.4 Adaptive Optics system based on interferometric wave-front sensing and membrane deformable mirror

4.4.1 Experimental Apparatus

A scheme of the experimental apparatus is drawn in fig. 4.4. The beam of a 10 mW He-Ne laser is split in the two arms of a bench-top Michelson interferometer. In order to check the technique, the efficiency and the noise reintroduced by the AO system, the beam of one arm is used as the reference beam while the beam in the second arm, which is equipped with a membrane deformable mirror, is the corrected beam. The bench is seismically isolated by means of commercial isolation system (Newport).

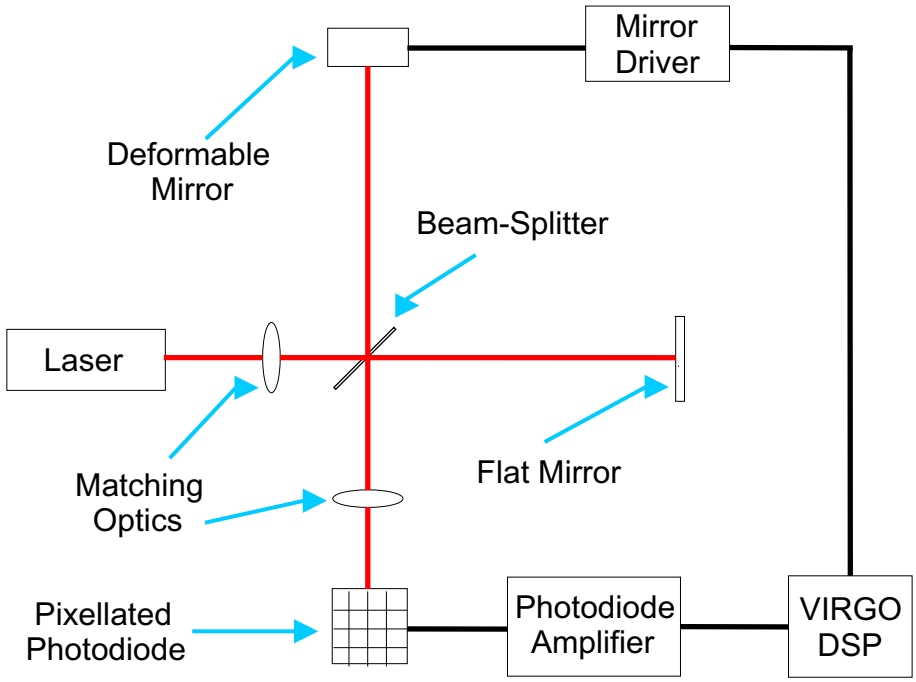

Figure 4.4: Optical scheme showing the experimental apparatus.

At the output of the Michelson the phase difference is read by a pixellated rectangular (4x4) photodiode. The phase difference is detected in the middle fringe working point; the typically small laser perturbations do not introduce 2π ambiguities in the wavefront, so that the signal on each pixel is directly proportional to the phase difference of the beams in that wavefront area. The error signals are calculated projecting the 16 wavefront signals on the first and second order Hermite-Gauss modes, then the control signals are obtained by projecting each mode on the corresponding Zernike polynomial to produce the mirror deformation [3,6]. The digital electronics of the system is based on Virgo DSP (Digital Signal Processing) cards, developed within the Virgo gravitational wave experiment: each channel is sampled at 10 *kHz*, and all matrix operations for error signals extraction and correction signals generation are carried out digitally within the DSP.

4.4.2 Wavefront sensing

The wavefront sensor of the system consist of a 5x5 Si PIN photodiode array (produced by Hamamatsu Photonics) used in the 4x4 configuration (fig. 4.5). Each pixel is 1.3×1.3 mm. The sensor is placed at the waist position of the interfering beams. If we consider the first beam as reference beam, and the second beam as perturbed beam, we can write (remembering that in the middle fringe working point the phase-difference between the two beams is $\pi/2$):

$$\mathbf{E}_1 = Ai\Psi_{00} \tag{4.10}$$

$$\mathbf{E}_2 = A\left[(1+i\phi)\Psi_{00} + \mathbf{a}_x\Psi_{10} + \mathbf{a}_y\Psi_{01} + \mathbf{a}_{45}\Psi_{11} +\right.$$

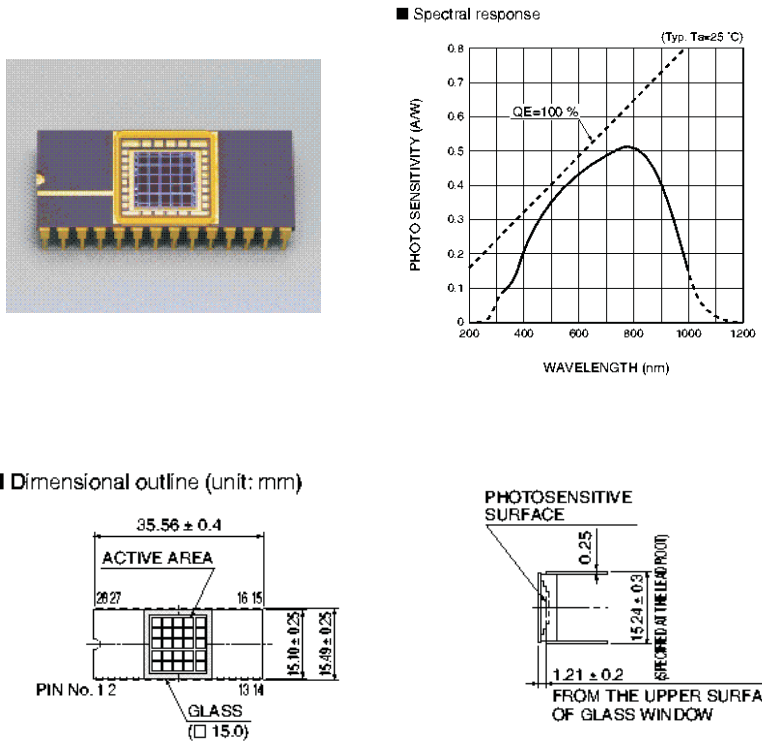

Figure 4.5: 5x5 Si PIN photodiode array: geometry and spectral response.

$$+\mathbf{a}_{90}(\Psi_{20}-\Psi_{02})/\sqrt{2}+\mathbf{a}_D(\Psi_{20}+\Psi_{02})/\sqrt{2}\Big] \tag{4.11}$$

where the coefficients $\mathbf{a}_i$ are complex numbers and ϕ is the phase-difference between the two beams.

The total intensity at the output, at the first order in a_i and ϕ, is:

$$|\mathbf{E}_{tot}|^2/2A^2 = |\mathbf{E}_1+\mathbf{E}_2|^2/2A^2 = (1+\phi)|\Psi_{00}|^2 + \mathbf{a}^*{}_x\Psi_{00}\Psi_{10}+$$

$$+\mathbf{a}^*{}_y\Psi_{00}\Psi_{01} + \mathbf{a}^*{}_{45}\Psi_{00}\Psi_{11}+$$

$$+\mathbf{a}^*{}_{90}\Psi_{00}(\Psi_{20}-\Psi_{02})/\sqrt{2} + \mathbf{a}^*{}_D\Psi_{00}(\Psi_{20}+\Psi_{02})/\sqrt{2} \tag{4.12}$$

where $\mathbf{a}_i^* = (\mathbf{Re}a_i + \mathbf{Im}a_i)$.

Considering particular combinations of the 16 photodiode signals it is possible to measure the coefficients $\mathbf{a}^*{}_i$ and ϕ (Fig. 4.6). The system can be represented by a *6x6* matrix $\mathbf{C}_{nm}$ which satisfies the equation:

$$\begin{pmatrix} \mathbf{S}_1 \\ \mathbf{S}_2 \\ \mathbf{S}_3 \\ \mathbf{S}_4 \\ \mathbf{S}_5 \\ \mathbf{S}_6 \end{pmatrix} = \begin{pmatrix} c_{11} & c_{12} & c_{13} & c_{14} & c_{15} & c_{16} \\ c_{21} & c_{22} & c_{23} & c_{24} & c_{25} & c_{26} \\ c_{31} & c_{32} & c_{33} & c_{34} & c_{35} & c_{36} \\ c_{41} & c_{42} & c_{43} & c_{44} & c_{45} & c_{46} \\ c_{51} & c_{52} & c_{53} & c_{54} & c_{55} & c_{56} \\ c_{61} & c_{62} & c_{63} & c_{64} & c_{65} & c_{66} \end{pmatrix} * \begin{pmatrix} \phi \\ \mathbf{a}^*{}_x \\ \mathbf{a}^*{}_y \\ \mathbf{a}^*{}_{45} \\ \mathbf{a}^*{}_{90} \\ \mathbf{a}^*{}_D \end{pmatrix} + \begin{pmatrix} \mathbf{H}_1 \\ \mathbf{H}_2 \\ \mathbf{H}_3 \\ \mathbf{H}_4 \\ \mathbf{H}_5 \\ \mathbf{H}_6 \end{pmatrix} \tag{4.13}$$

were $\mathbf{H}_i$ are geometrical constants of the system, and $\mathbf{S}_i$ are the error signals proportional to the aberrations expressed in terms of higher order modes. Considering that we are developing the aberrated beam up to second order, we have six terms: longitudinal, tiltX, tiltY, astigmatism45, astigmatism90, defocus. The signals $\mathbf{S}_i$ can be calculated by integration of $|\mathbf{E}_{tot}|^2$ on each pixel of the photodiode array with the signs indicated in fig. 4.6. Then for the longitudinal term $\mathbf{S}_1$ we have:

$$\mathbf{S}_1 = \int_{-2l}^{2l} dx \int_{-2l}^{2l} dy |\mathbf{E}_{tot}|^2 = \int_{-2l}^{2l} dx \int_{-2l}^{2l} dy \Big[(1+\phi)|\Psi_{00}|^2 +$$

$$+ \mathbf{a}_D^* \Psi_{00}(\Psi_{20} + \Psi_{02})/\sqrt{2} \Big] = \mathbf{c}_{11}(l, w_0)[1+\phi] + \mathbf{c}_{16}(l, w_0)\mathbf{a}_D^* \tag{4.14}$$

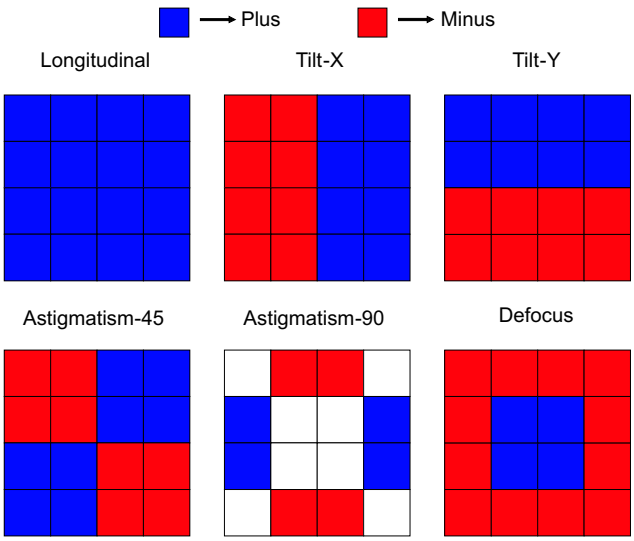

Figure 4.6: Photodiode array signal extraction. The array consists of 16 pixels, particular combinations of the pixel signals give directly the measurement of aberrations in terms of higher order modes up to second order. The blue boxes are taken with plus sign while the red boxes are taken with minus sign.

For the tiltX term $\mathbf{S}_2$ we have:

$$\mathbf{S}_2 = \int_{-2l}^{2l} dy \left[\int_0^{2l} dx |\mathbf{E}_{tot}|^2 - \int_{-2l}^{0} dx |\mathbf{E}_{tot}|^2 \right] =$$

$$= \mathbf{a}_x^* \int_{-2l}^{2l} dy \left[\int_0^{2l} dx \Psi_{00}\Psi_{10} - \int_{-2l}^{0} dx \Psi_{00}\Psi_{10} \right] = \mathbf{c}_{22}(l, w_0)\mathbf{a}_x^* \tag{4.15}$$

For the tiltY term $\mathbf{S}_3$ we have:

$$\mathbf{S}_3 = \int_{-2l}^{2l} dx \left[\int_0^{2l} dy |\mathbf{E}_{tot}|^2 - \int_{-2l}^{0} dy |\mathbf{E}_{tot}|^2 \right] =$$

$$= \mathbf{a}_y^* \int_{-2l}^{2l} dx \left[\int_0^{2l} dy \Psi_{00}\Psi_{01} - \int_{-2l}^{0} dy \Psi_{00}\Psi_{01} \right] = \mathbf{c}_{33}(l, w_0)\mathbf{a}_y^* \tag{4.16}$$

For the asitgmatism45 term $\mathbf{S}_4$ we have:

$$\mathbf{S}_4 = \int_0^{2l} dx \int_0^{2l} dy |\mathbf{E}_{tot}|^2 + \int_{-2l}^{0} dx \int_{-2l}^{0} dy |\mathbf{E}_{tot}|^2 - \int_0^{2l} dx \int_{-2l}^{0} dy |\mathbf{E}_{tot}|^2 +$$

$$- \int_{-2l}^{0} dx \int_0^{2l} dy |\mathbf{E}_{tot}|^2 = 4 \int_0^{2l} dx \int_0^{2l} dy \Psi_{00}\Psi_{11} = \mathbf{c}_{44}(l, w_0)\mathbf{a}_{45}^* \tag{4.17}$$

For the astigmatism90 term $\mathbf{S}_5$ we have:

$$\mathbf{S}_5 = -\int_l^{2l} dy \int_{-l}^{l} dx |\mathbf{E}_{tot}|^2 - \int_{-2l}^{-l} dy \int_{-l}^{l} dx |\mathbf{E}_{tot}|^2 + \int_l^{2l} dx \int_{-l}^{l} dy |\mathbf{E}_{tot}|^2 +$$

$$+ \int_{-2l}^{-l} dx \int_{-l}^{l} dy |\mathbf{E}_{tot}|^2 = -4 \int_l^{2l} dy \int_{-l}^{l} dx \Psi_{00}(\Psi_{20} - \Psi_{02})/\sqrt{2} = \mathbf{c}_{55}(l, w_0)\mathbf{a}^*_{90} \quad (4.18)$$

Finally for the defocus term $\mathbf{S}_6$ we have:

$$\mathbf{S}_6 = -\int_{-l}^{l} dx \int_{-l}^{l} dy |\mathbf{E}_{tot}|^2 + \int_{-2l}^{2l} dx \int_l^{2l} dy |\mathbf{E}_{tot}|^2 + \int_{-2l}^{2l} dx \int_{-2l}^{-l} dy |\mathbf{E}_{tot}|^2 +$$

$$+ \int_{-l}^{l} dy \int_l^{2l} dx |\mathbf{E}_{tot}|^2 + \int_{-l}^{l} dy \int_{-2l}^{-l} dy |\mathbf{E}_{tot}|^2 = \mathbf{c}_{61}(l, w_0)(1+\Phi) + \mathbf{c}_{66}(l, w_0)\mathbf{a}^*_D \quad (4.19)$$

The coefficients $\mathbf{c}_{ij}$ are functions of l (pixel side) and w_0, obtained by scalar products of Hermite-Gauss modes over particular domains characterized by the geometry of the photodiode (see appendix A). From eq. 4.14-4.19 we can see that there is a coupling between the signals $\mathbf{S}_1$ and $\mathbf{S}_6$, while the other signals are decoupled. Moreover, we have only the term $\mathbf{H}_1 = \mathbf{c}_{11}$ and $\mathbf{H}_6 = \mathbf{c}_{61}$ the others being null. Therefore, with these combinations of pixels the equation 4.13 become:

$$\begin{pmatrix} \mathbf{S}_1 \\ \mathbf{S}_2 \\ \mathbf{S}_3 \\ \mathbf{S}_4 \\ \mathbf{S}_5 \\ \mathbf{S}_6 \end{pmatrix} = \begin{pmatrix} c_{11} & 0 & 0 & 0 & 0 & c_{16} \\ 0 & c_{22} & 0 & 0 & 0 & 0 \\ 0 & 0 & c_{33} & 0 & 0 & 0 \\ 0 & 0 & 0 & c_{44} & 0 & 0 \\ 0 & 0 & 0 & 0 & c_{55} & 0 \\ c_{61} & 0 & 0 & 0 & 0 & c_{66} \end{pmatrix} * \begin{pmatrix} \phi \\ \mathbf{a^*}_x \\ \mathbf{a^*}_y \\ \mathbf{a^*}_{45} \\ \mathbf{a^*}_{90} \\ \mathbf{a^*}_D \end{pmatrix} + \begin{pmatrix} \mathbf{H}_1 \\ \mathbf{0} \\ \mathbf{0} \\ \mathbf{0} \\ \mathbf{0} \\ \mathbf{H}_6 \end{pmatrix} \quad (4.20)$$

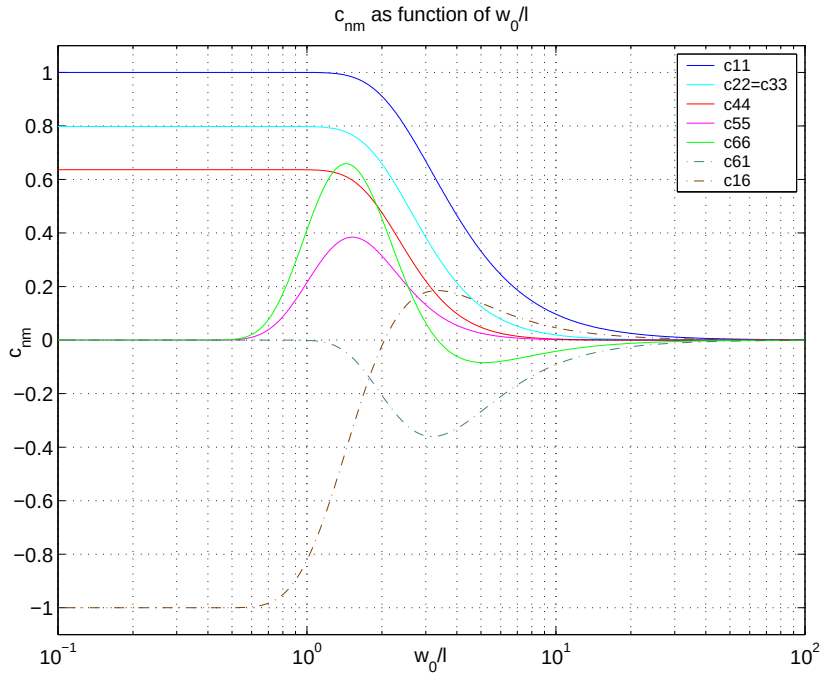

Figure 4.7: $\mathbf{c}_{nm}$ coefficients as function of w_0/l.

In fig. 4.7 are plotted all the non-null coefficients $\mathbf{c}_{ij}$. We can see that the coefficients $\mathbf{c}_{11}$, $\mathbf{c}_{22}$, $\mathbf{c}_{33}$, $\mathbf{c}_{44}$ have a similar behavior. In particular, for high w_0/l, that is when the beam is much greater than the photodiode, they go to zero. While when w_0/l goes to zero, that is when the beam is focused at the center of the matrix (in this case the beam cover only the four central pixels), the coefficients become constant. So for these signals it would be better to focus the beam in the center of the array (in practice it can be used a 2x2 array). Nevertheless, the signals $\mathbf{c}_{55}$, $\mathbf{c}_{66}$ are different because they become null when w_0/l goes to zero. So we can find an optimal value for the parameter w_0/l.

In fig. 4.8 we have a zoom of the plot of fig. 4.7 in the interval $[0, 3]$. We can see that if we choose $1.4 < w_0/l < 1.6$ all the coefficients $\mathbf{c}_{ii}$ are near their maxima and vary slow with w_0/l. Moreover the coefficient $\mathbf{c}_{61}$ can be neglected, and the matrix

$\mathbf{C}_{nm}$ becomes quasi-diagonal, only a term out-diagonal remains of relative amplitude of 30%. Anyway, in these conditions the loop can be closed with robustness and efficiency, as is the case for triangular feedback systems (multi-dimensional feedback systems having the transfer function matrix triangular)[56]. Indeed, in this case, the loop stability is determined by the diagonal elements; the off diagonal elements contribute to the residual error signal, divided by the diagonal element gains. If these gains are chosen sufficiently high, compatibly with stability, the feedback controls are efficient in all degrees of freedom of interest.

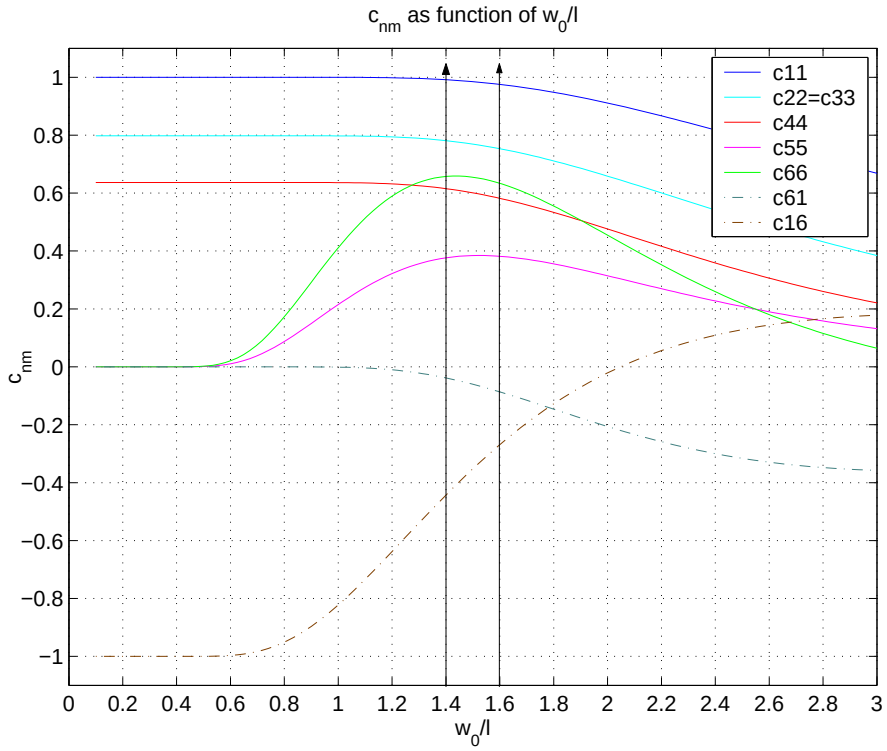

Figure 4.8: $\mathbf{c}_{nm}$ coefficients as function of w_0/l in the interval $[0, 3]$.

4.4.3 Actuation

The actuator of the system is a micromachined membrane deformable mirror produced by OKOtech (Fig. 4.9). The mirror, consists of a silicon chip mounted over a PCB holder. The chip contains a silicon nitride membrane, which is coated to form a mirror. The PCB contains the control electrode structure, spacer and connector. It also serves as mirror package. The shape of the reflective membrane is controlled by voltages applied to the control electrodes with the membrane grounded (fig. 4.10).

Figure 4.9: Micromachined membrane deformable mirror produced by OKOtech.

The reflecting membrane is circular with diameter of 15 *mm*, the center-to-center distance between the electrodes is 1.75 *mm*, the control voltage is 0-250 V for each actuator. In fig. 4.11 is shown the actuators map, it consists of 37 electrodes distributed in hexagonal geometry. The whole actuator structure is located within 12 *mm* circle under the mirror membrane.

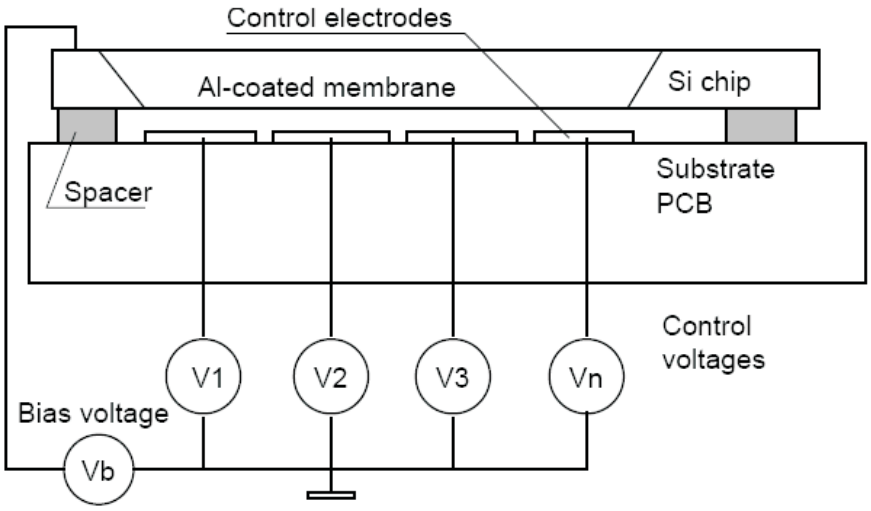

Figure 4.10: Section of the deformable mirror.

Mirror socket consists of a PCB holder with PGA-compatible connector on the front side and two band cable connectors on the back side. The first (close to the socket) bandcable connector controls central 19 actuators of the hexagonal structure and provides connection to the ground. The second connector controls 18 peripheral electrodes (two pins are not connected). The mirror is used with only one control board (19-channel variant).

The six aberrations measured by the photodiode array as higher order modes are projected on the Zernike polynomials base. The coefficients obtained are filtered and sent to the mirror electrodes to drive the mirror surface for the feed-back. In particular, If the waist of the beam is used as the unit circle for wave front perturbations expansion in Zernike polynomials, there is a direct correspondence between Hermite-Gauss modes and Zernike polynomials [44]. This correspondence allows for an easy calculation of the higher-order Hermite-Gauss modes by calculation of the scalar product of the wavefront with the corresponding Zernike polynomials on the

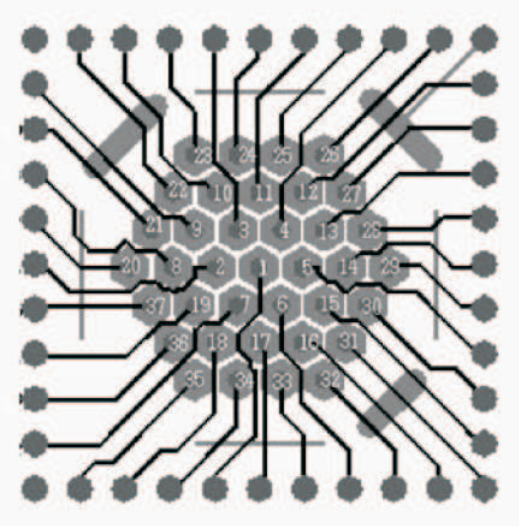

Figure 4.11: Actuators map.

circle of radius equal to beam waist (i.e. the integral on the area of the circle having a radius equal to the waist). Consequently, a feedback system can be made generating the error signals for the feedback as the corresponding Zernike polynomials on the mirror, and an estimate of efficiency of the feedback system can be done directly in terms of Hermite-Gauss modes.

The modal feedback scheme is completed by the diagonalization of actuator matrix. Due to the low number of degrees of freedom and to the low coupling between them (about 10%), the diagonalization can be obtained using an iterative method. A control signal relative to the aberration A_i is sent to the mirror and the aberrations a_n induced is measured by the interferometer. If only the corresponding aberration a_i is measured the iteration stops. If there is a coupling ($> 1\%$) with the aberration a_j, the measured aberration signal is used to correct the control signal A_i. The iteration goes on as long as the coupling is less than 1%.

4.4.4 Signal processing

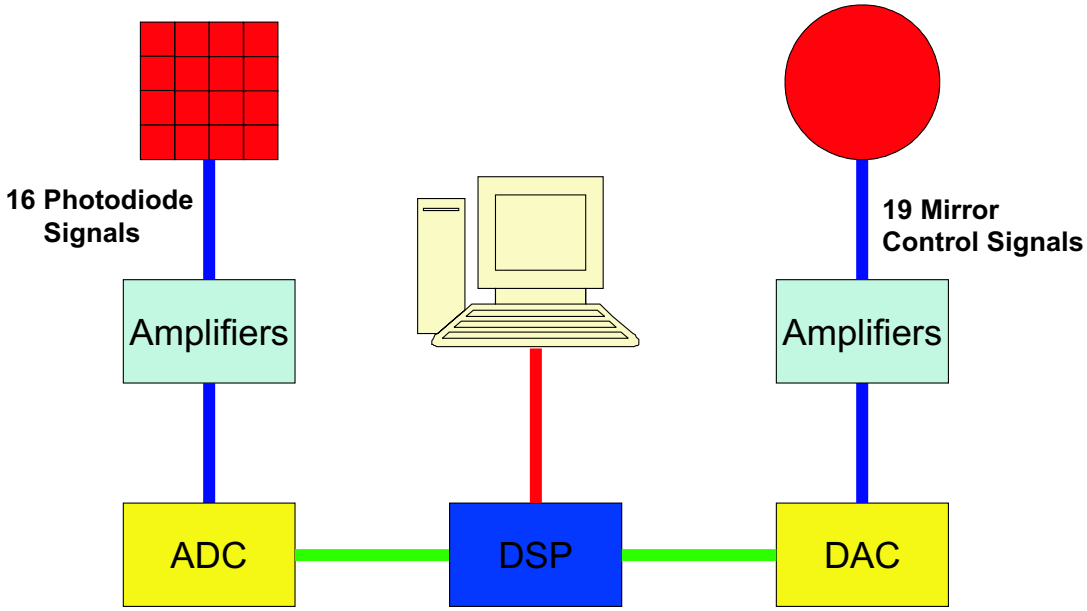

Figure 4.12: Signal processing scheme.

The signal processing is performed digitally by using a DSP (digital signal processor) developed in the framework of Virgo experiment. In Fig. 4.12 is shown the scheme of the signal processing system. The processing steps can be resumed as follow:

- the 16 signals outgoing the photodiode array are amplified and sent to the ADC system;
- each signal is sampled at 10 kHz by a 16-bit ADC with a dynamic of $\pm 5V$;
- through a dedicated BUS the signals are sent to the DSP;
- the DSP combines the input signals to obtain the six aberration error signals;

- the six aberration error signals are digitally filtered and combined to obtain the 19 mirror control signals;
- each of 19 control signals is sent trough a dedicated BUS to a 20-bit DAC with a dynamic of $\pm 5V$;
- the 19 analog signals are amplified and sent to the deformable mirror electrodes.

The DSP is programmed in assembler by a PC. The operations of combination and filtering are implemented through a user-friendly program written in C running on PC. The parameters to set are the sampling frequency, the ADC input addresses, the filter parameters (poles and zeros) for each signal, the output DAC addresses. At each signal can be associated an internal variable to perform arbitrary combinations and filtering.

4.4.5 Experimental results

The interferometer has been locked with all degrees of freedom simultaneously controlled. In particular, they have been tested two different control bandwidths, corresponding to a low frequency thermal compensation bandwidth (unity gain of about 1 Hz) and a higher bandwidth corresponding to active dynamical perturbation prefiltering, of the order of 80 Hz. In the first case the electronic servo-loop, performed by the DSP, is simply a real pole at frequency $f = 0.01$ *Hz* and the open loop gain is chosen to be unity at 1 *Hz*. In the second case two real poles are added at 0.01 *Hz* in order to have high efficiency at low frequency, and three zeros are added respectively at 20 *Hz*, 30 *Hz* and 60 *Hz* (followed by another real pole at 200 *Hz*), so to compensate for phase rotation due to anti-aliasing filters and extending the

closed-loop bandwidth of the system up to 200 *Hz*. The open loop gain is chosen to be unity at about 50-60 *Hz* for all the six degrees of freedom controlled.

The relevant results are presented in fig. 4.13-4.17, where the open and closed loop error signals are shown for the two tilts, the two astigmatisms and the defocus. It is important to point out that the results on an error signal (which is an in-loop measurement) have different meanings depending on the frequency region considered.

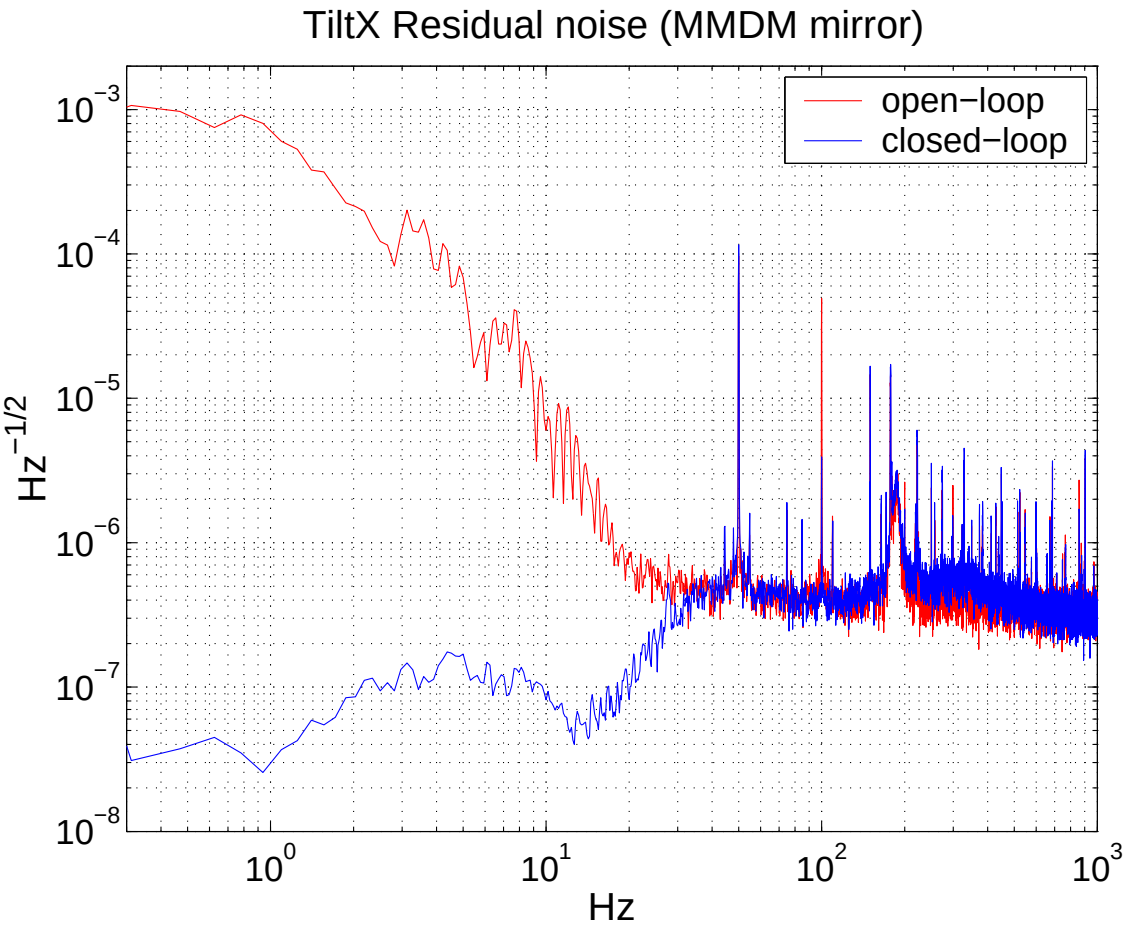

Figure 4.13: Open and closed loop residual noise of the mode TEM_{10}, corresponding to a tilt on x axis.

In the frequency region over the unity gain frequency, the error signal is equivalent to an out-loop signal, because it measures the (uncorrected) signal in that frequency region. Thus, in this region the difference between open and closed loop signals measures just the eventual noise reintroduced by the system. In our case the feed-back unity gain can be varied from 0.1 *Hz* to several tens of *Hz*. In all cases no difference

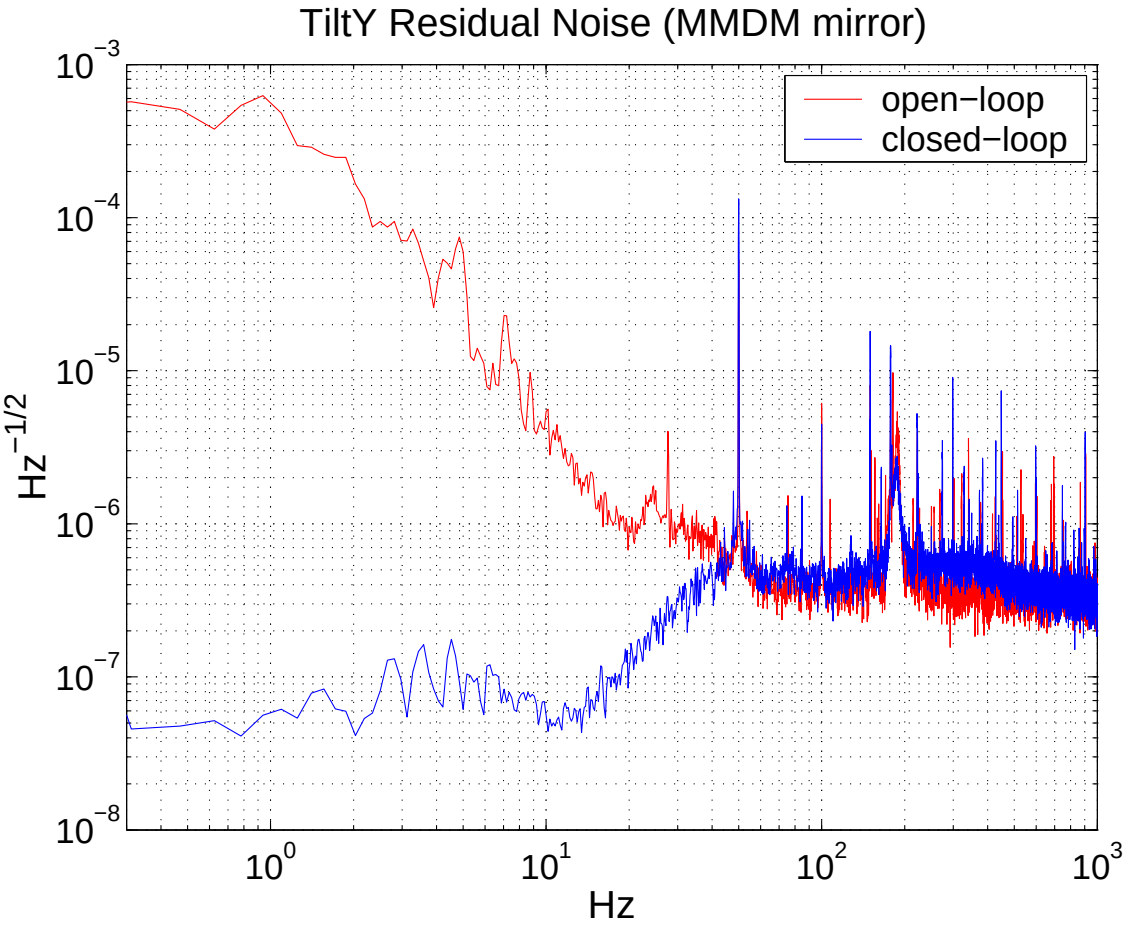

Figure 4.14: Open and closed loop residual noise of the mode TEM_{01}, corresponding to a tilt on y axis.

between open-loop and closed-loop signals is measured, residual noise being always below the limit of $\tilde{A}_{mn} < 10^{-5}\frac{1}{\sqrt{Hz}}$ for frequency higher than some tens of *Hz*. The closed loop error signals shown in fig. 4.13-4.17 present unity gain frequency of about 50-60 *Hz*. The unity gain has been chosen to be comparable with the present Virgo tilt actuators, called ABP (Automatic Beam Positioner), which correct the

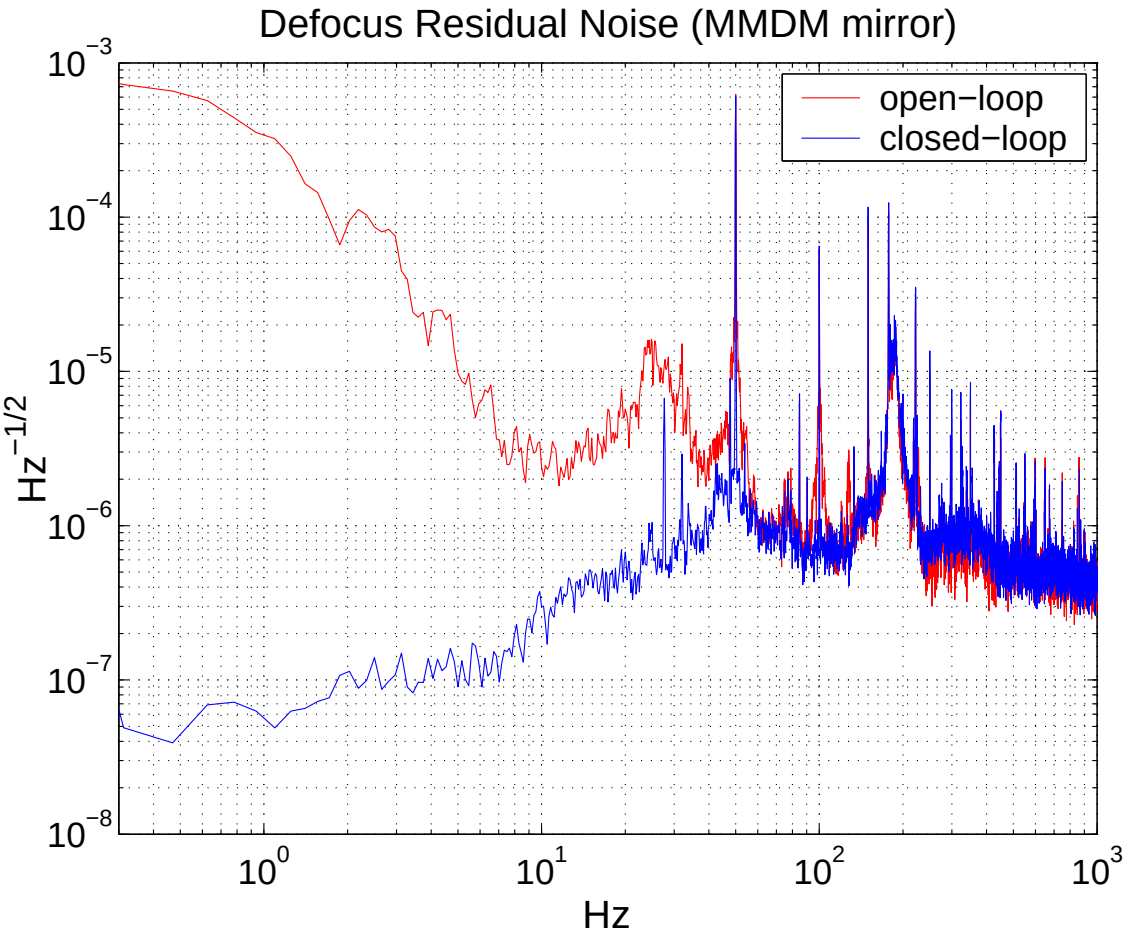

Figure 4.15: Open and closed loop residual noise of the mode $\frac{1}{\sqrt{2}}(TEM_{20} + TEM_{02})$, corresponding to a defocus.

beam tilts with a 40 *Hz* unity gain [14]. Similar results can be obtained, of course, relaxing the unity gain specification to lower frequencies. In the region below the unity gain frequency, the error signal is an in-loop signal, this is not usable as a measurement of the residual noise. In this case, the measurement demonstrates that given an error signal, the control system can correct the geometrical aberrations

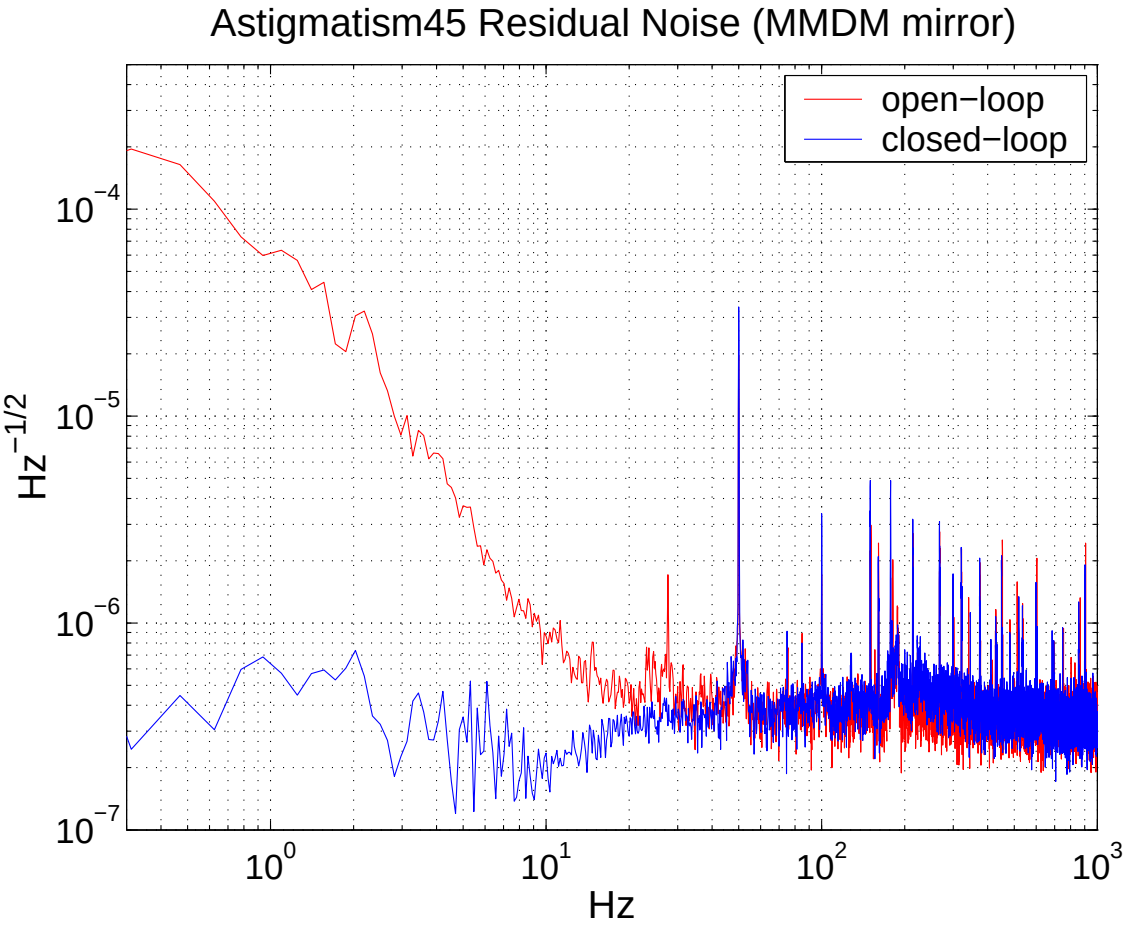

Figure 4.16: Open and closed loop residual noise of the mode TEM_{11}, corresponding to the astigmatism45.

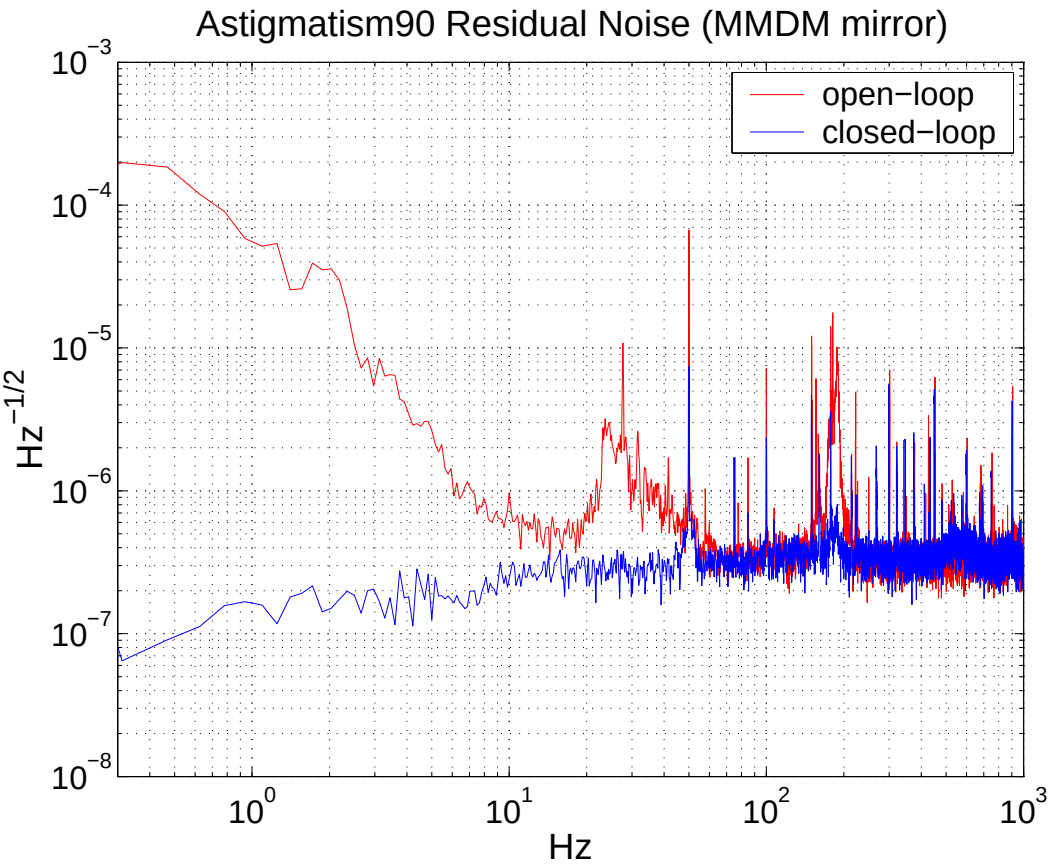

Figure 4.17: Open and closed loop residual noise of the mode $\frac{1}{\sqrt{2}}(TEM_{20} - TEM_{02})$, corresponding to the astigmatism90.

of several tens dB (at minimum 40 dB at low frequency), an efficiency required by Virgo specifications.

Therefore, this AO system is capable, once given an error signal, to correct it with the following required specifications:

- all degrees of freedom (up to second order) controlled;
- about 60 dB efficiency at low frequency;
- bandwidth of about 50-60 *Hz*;

- noise reintroduced at high frequency under the constraint $\tilde{A}_{mn} < 10^{-5}\frac{1}{\sqrt{Hz}}$ for each degree of freedom.

Nevertheless, the use of membrane deformable mirror presents two relevant problems. The first one is that this mirror has not high optical quality to be consider for implementation in a complex and high quality optical system like a gravitational wave interferometer. Moreover, it shows intrinsic aberrations when pretensioned, mainly due to the fact the membrane is clamped to the edge. The second and fundamental problem is that this mirror cannot sustain the high power laser (hundred of Watts) foreseen for advanced gravitational wave detectors. For these reasons, as described below it has been tested another kind of deformable mirror, based on piezoelectric actuation which can overcome these problems.

4.5 Implementation of a piezoelectric deformable mirror as actuator

4.5.1 Piezoelectric deformable mirror

The correction actuator is a piezoelectric deformable mirror produced by OKO-Flexible Technology, 3 *cm* in diameter and actuated with 19 piezo-actuators. The mirror is shown in fig. 4.18, it consists of 19 piezoelectric column actuators bonded to the base holder. The reflective plate is bonded to the top of the actuator structure and coated to form the mirror. The shape of the faceplate is controlled by the voltages applied to the actuators. The electrodes geometry is again hexagonal and the control voltage is 0-400 V for each actuator. This mirror has been chosen in order to have high band-pass, high optical quality, and especially it can sustain high power lasers.

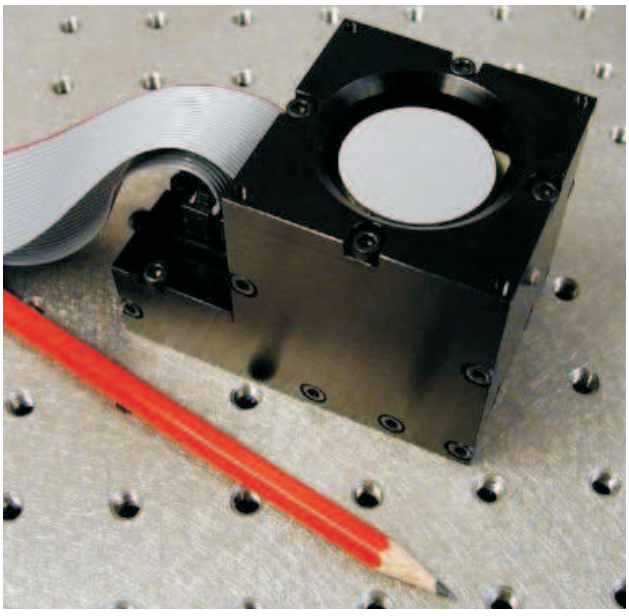

Figure 4.18: Piezoelectric deformable mirror produced by OKOtech.

4.5.2 Experimental results

The piezoelectric deformable mirror, as indicated in Fig. 4.19-4.21, has shown a similar behavior with respect to the membrane deformable mirror. The system present again an unity gain of about 50-60 Hz, and the reintroduced noise is under the limit $\tilde{A}_{mn} < 10^{-5}\frac{1}{\sqrt{Hz}}$.

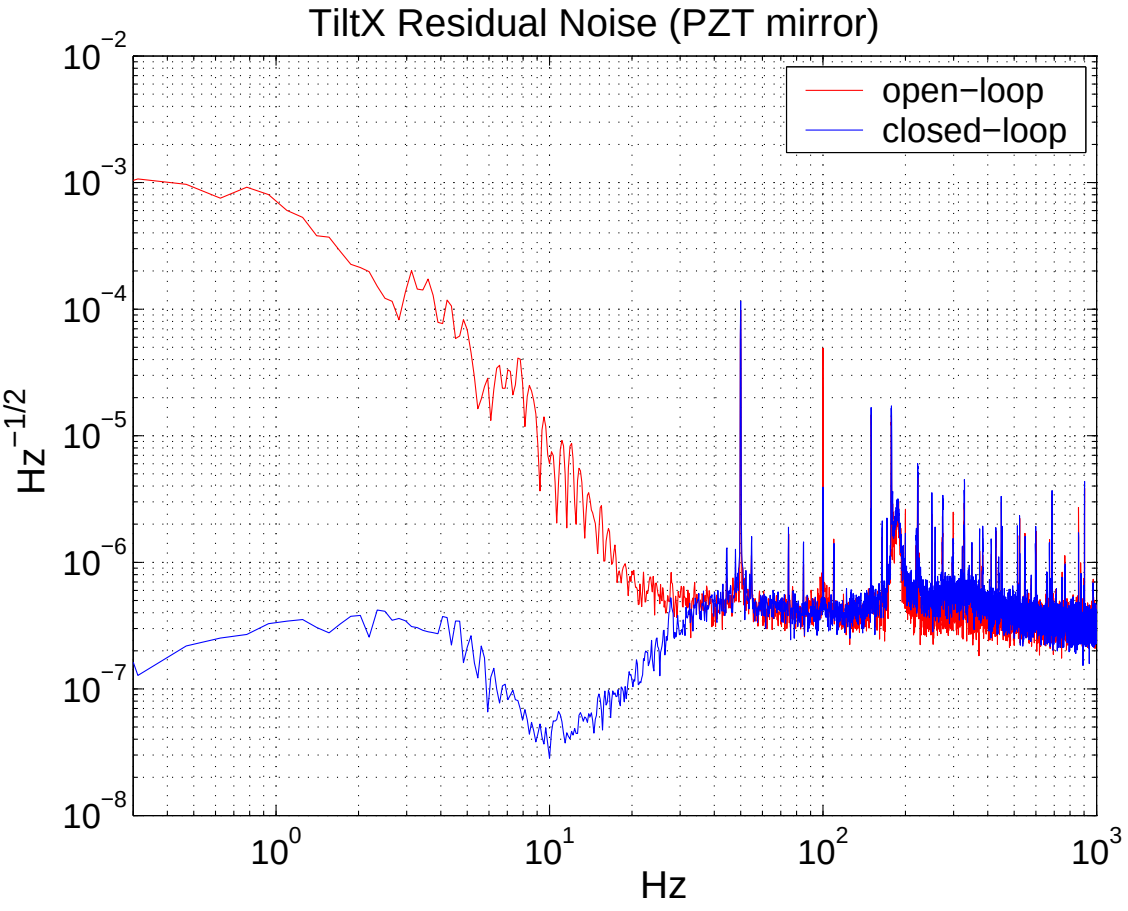

Figure 4.19: Open and closed loop residual noise of the mode TEM_{10}, corresponding to a tilt on x axis (using PZT mirror).

It is important to point out that with respect to the MMDN mirror, the PZT mirror has higher optical quality. Moreover, the MMDM mirror presents intrinsic aberrations when pretensioned, mainly due to the fact the membrane is clamped to the edge. This problem is strongly reduced by using PZT mirror which also must be pretensioned but has free edge reflective surface. Finally, the PZT mirror can sustain the high power lasers foreseen for advanced gravitational wave detectors.

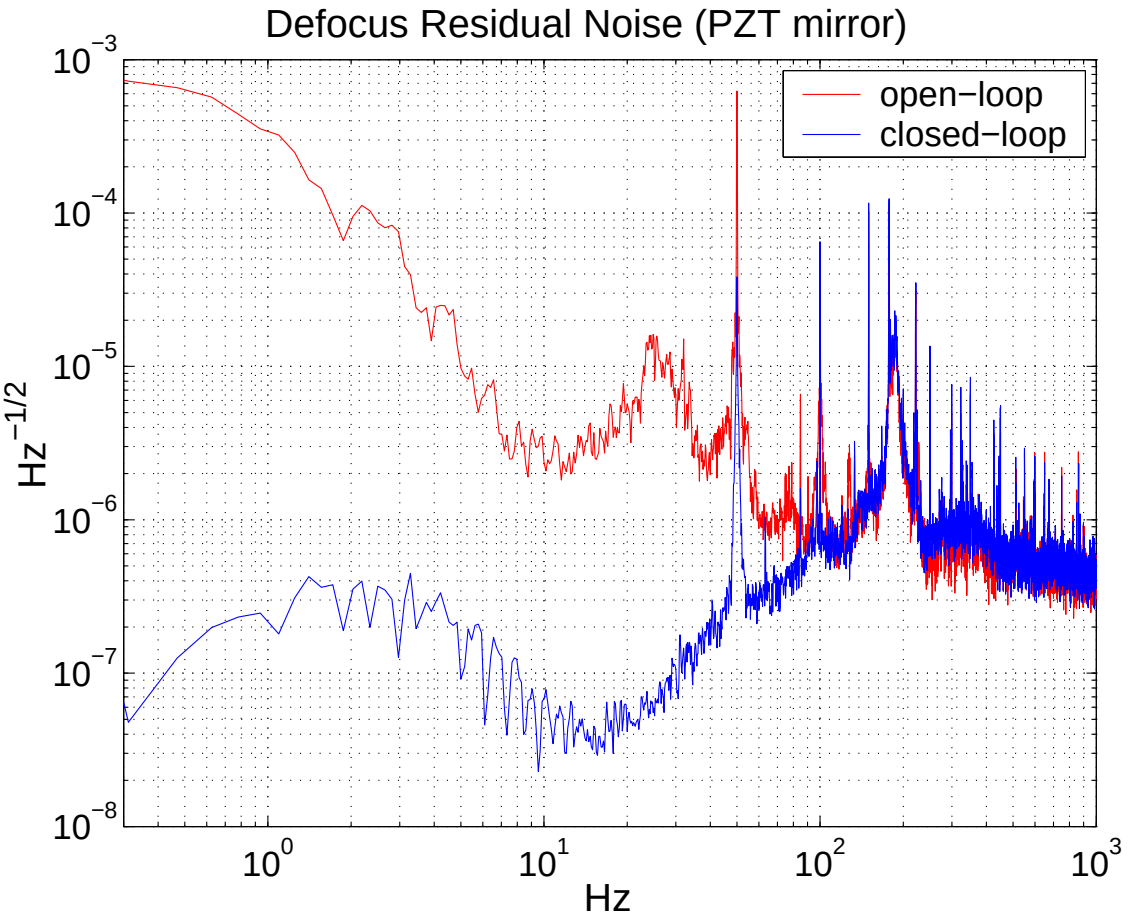

Figure 4.20: Open and closed loop residual noise of the mode $\frac{1}{\sqrt{2}}(TEM_{20} + TEM_{02})$, corresponding to defocus (using PZT mirror).

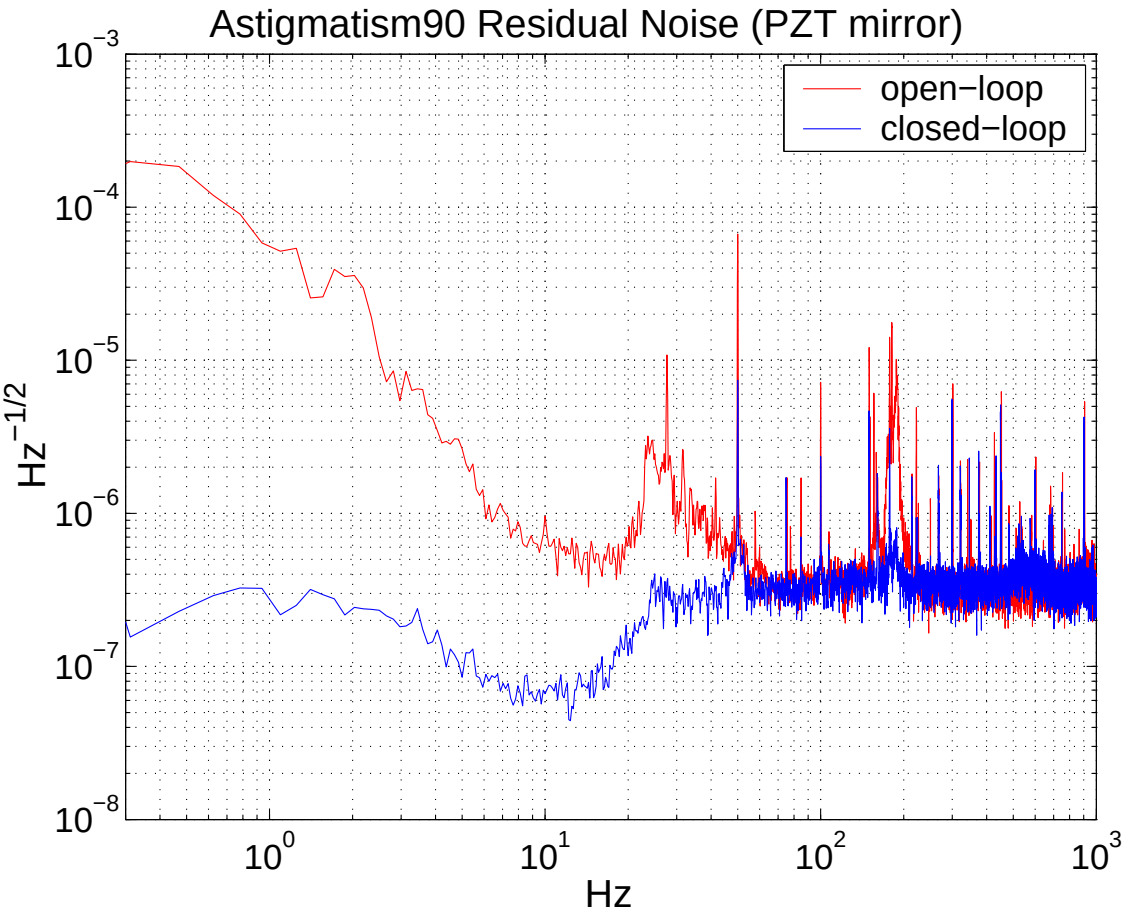

Figure 4.21: Open and closed loop residual noise of the mode $\frac{1}{\sqrt{2}}(TEM_{20} - TEM_{02})$, corresponding to 90-astigmatism (using PZT mirror).

4.6 Discussion

In this work it has been realized a Michelson interferometer controlled with Adaptive Optics. In particular it has been developed a particular signal extraction technique based on interferometric wavefront detection using a photodiodes array. By using this technique it is possible to extract directly (through simple combinations of array

signals) the coefficient of aberrations of the laser in terms of Hermite-Gauss higher order modes.

Two deformable mirrors have been tested for the actuation: a membrane deformable mirror and a piezoelectric deformable mirror. The mirrors have shown a similar behavior in terms of efficiency, bandwidth and noise reintroduction. In particular, the control system presents an efficiency of about 60 dB at low frequency, the unity gain is about 50-60 Hz and the noise reintroduction at high frequency is under the limit $\tilde{A}_{mn} < 10^{-5}\frac{1}{\sqrt{Hz}}$ foreseen for the application in the Virgo interferometer.

It is important to point out that, the PZT mirror present higher optical quality than the MMDM one. Moreover, the PZT mirror can sustain high power laser foreseen for next generation interferometers while the MMDM mirror did not. For these reasons the PZT mirror could be a real candidate for the implementation in a gravitational wave interferometer. In particular, as shown in fig. 4.3 an Adaptive Optics system could be implemented in a gravitational wave interferometer by using two deformable mirrors acting on the beam before the mode-cleaner. As error signal for the feed-back can be used the beam reflected by the mode-cleaner which contains all the higher order modes reflected back. A pixellated photodiode can be used to sense the different components of higher order modes using the classical Ward technique [53].

In conclusion, this AO system based on PZT deformable mirror could be used to correct the thermally induced aberrations as well as to perform a fast pre-mode-cleaning of the input laser beam already in the present detectors if necessary, or surely in the next generation high power interferometers.

Chapter 5

Generation of non-Gaussian flat laser beams

5.1 Introduction

The adaptive optics system described in previous chapter, can be used, with some modification, for a particular application: the generation of non-Gaussian flat laser beam. The use of flat-beam has been proposed to reduce the thermoelastic noise in advanced gravitational wave interferometers.

5.2 thermoelastic noise

As we saw in chapter 2 the sensitivity of a gravitational wave interferometer can be limited by different kinds of fundamental noises. One of the most important noise, which limits the interferometers in the region of maximum sensitivity (from about 50 Hz to about 500 Hz), is the mirror thermal noise [57].
There are different contributions to the mirror thermal noise. The *classical* mirror thermal noise (also called Brownian mirror thermal noise) is generated by the vibrations of the surfaces of the mirrors due to the internal modes of resonances, each one having energy proportional to the equilibrium temperature. The effects of the

random mirror surface vibrations on the sensitivity of gravitational waves detectors can be calculated by using the fluctuation-dissipation theorem and is widely studied and discussed in literature [58]. More recently, other effects to the mirror thermal noise have been considered, the most important of them is the so called thermoelastic noise [59, 60, 61].

The thermoelastic noise is due essentially to local fluctuations of temperature on the mirror surfaces. These temperature fluctuations can be generated by thermodynamical fluctuations or by laser power absorption in the mirrors [59]. Due to the non-zero thermal expansion coefficient of the mirrors material, the local regions of the mirrors with different temperatures expand differently. This effect, on time scale of random heat flow ($\approx 0.01s$), generates fluctuations of the surfaces of the mirrors. In particular, hot bumps expand while could bumps contract. The laser beam averages imperfectly these surfaces fluctuations, due to the gaussian amplitude profile [62].

In order to reduce these effects, for advanced detectors, it has been proposed to use non-gaussian flat beams (or *Mesa* beam) and to change the spherical mirrors of the Fabry-Perot cavities with Mexican-Hat mirrors [63, 64, 65].

5.3 Mexican-Hat cavities and generation of flat-beam

A flat beam (FB) is, essentially, a laser beam with a flatter amplitude profile than a Gaussian beam. By using FB the thermoelastic noise is reduced respect to the Gaussian one since a flatter amplitude profile averages better the thermal fluctuations of the mirror surfaces. For example, in the case of advanced LIGO (with sapphire mirrors), by replacing Gaussian beams with FB, the thermoelastic noise

power can be reduced of about a factor 3, which corresponds to an increase of the interferometer sensitivity of about a factor 2.5 in the frequency region of inspiraling neutron star binaries [65].

A non-gaussian flat beam can be represented as a superposition of gaussian modes (fig. 5.1) over a disc of radius p [63]. At waist position the flattest intensity profile we want to represent (a step function) is given by the field:

$$u_f(x,y) = \begin{cases} \frac{1}{\sqrt{\pi p^2}} \quad for \quad x^2+y^2 \leq p^2 \\ \\ 0 \quad for \quad x^2+y^2 > p^2 \end{cases} \tag{5.1}$$

By overlapping gaussian functions we obtain:

$$u_f(x,y) = \int\int_{x_0^2+y_0^2 \leq p^2} dx_0 dy_0 \quad \times$$

$$\times \sqrt{\frac{2}{w_0^2 \pi}} \quad e^{-(1/w_0^2)[(x-x_0)^2+(y-y_0)^2]} \tag{5.2}$$

$$with \quad \frac{w_0}{p} \to 0$$

where $w_0 = \sqrt{\lambda L/2\pi}$ is the minimum waist of a gaussian mode in a Fabry-Perot cavity of length L. If we choose w_0 too small respect to p, the field of each gaussian beam spreads too much in the propagation, while for w_0 too large, the flat beam generated by superposition will be too spread out. Therefore, depending by the

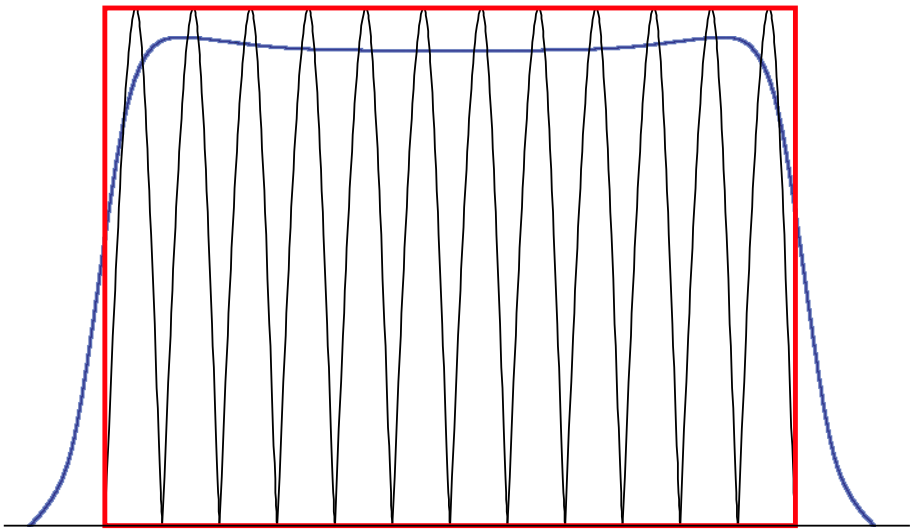

Figure 5.1: Flat-beam as overlapping of gaussian functions. The red curve shows the limit case $\frac{w_0}{p} \to 0$, while the blue curve is obtained by choosing a finite value for $\frac{w_0}{p}$.

cavity geometry, by the laser wavelength and by the limits on the diffraction losses, it is possible to find an optimal value for the ratio w_0/p [63].

The technique proposed [64, 65] to generate a FB is to build a Fabry-Perot cavity composed by mirrors of particular shape called Mexican-Hat mirrors. This kind of cavity can generate a FB by transforming an incoming Gaussian beam whose parameters are opportunely optimized in order to have the largest overlap with the FB desired. These technique are now under test [66]. The Mexican-Hat mirrors has been already built, and a cavity prototype has been realized. The technique seem to be very promising but some problem still need to be resolved about the cavity control and the generation of fundamental flat-beam mode.

5.4 Generation of flat-beam by using deformable mirrors

In order to use deformable mirrors to generate FB, it is useful to approximate the FB by using the usual Hermite-Gaussian modes [50, 51]. In fact, as demonstrated in previous chapter it is possible to correct laser geometrical aberrations, represented as higher order Hermite-Gauss modes, by using deformable mirrors (usually described by the Zernike Polynomials). In this application, the same technique has been used inversely, that is, a couple of deformable mirrors have been used to shape a gaussian fundamental mode by adding higher order modes. In general this system can be used to generate any arbitrary shape.

To illustrate the relation between the geometrical aberrations and the higher Hermite-Gaussian modes we analyze a simple case. Consider a pure TEM_{00} laser beam impinging, at waist position, upon a deformable mirror of arbitrary surface shape:

$$U_{in}(\vec{x}) = A\Phi_{00}(\vec{x}) \tag{5.3}$$

For small perturbations of the wavefront, the beam after the reflection can be written as:

$$U_{ref}(\vec{x}) = a_{00}\Phi_{00}(\vec{x}) + \sum_{m,n=1}^{\infty} (a_{mn} + ib_{mn})\Phi_{mn}(\vec{x}) \tag{5.4}$$

where the Φ_{mn} modes are evaluated at waist position again.

For example, we can simply shape the mirror surface spherically (with radius of curvature R). In this case the effect on the incoming beam is to change the diameter and the radius of curvature of the beam. If we consider a small change of the diameter of the reflected beam $w_0^{'} = w_0(1+\epsilon)$, the amplitude of this beam can be written as [31]:

$$\psi(r) \approx A[V_0(r) + \epsilon V_1(r)] \tag{5.5}$$

where $V_0(r)$ and $V_1(r)$ are respectively the fundamental and the first order Laguerre-Gauss mode [50, 67] (we have switched to Laguerre-Gauss description only for this example motivated by the symmetry of the problem, of course we can use the Hermite-Gauss modes). Instead, if we consider a small change of the radius of curvature, the reflected beam is:

$$\psi(r) \approx A[V_0(r) + i(k/2)V_1(r)] \tag{5.6}$$

where the radius of curvature is $R = k^{-2}$. In our case (spherical mirror) the variation of diameter and radius of curvature are correlated, so for an incoming beam $V_0(r)$, after the reflection we have:

$$\psi(r) \approx A[V_0(r) + (a + ib)V_1(r)] \tag{5.7}$$

with $b = f(a)$. If a second spherical mirror of radius $R^{'}$ is placed at a distance d, so that

$$d = \frac{1}{2}(R + R^{'}) \tag{5.8}$$

the beam after the second reflection has the wavefront flat and the diameter equal to $R^{'}/R$. This is clearly, depending by the fraction $R^{'}/R$, a simple beam expander or reducer. The effect of such a system on an incoming beam, is that of changing the beam diameter without changing the wavefront shape.

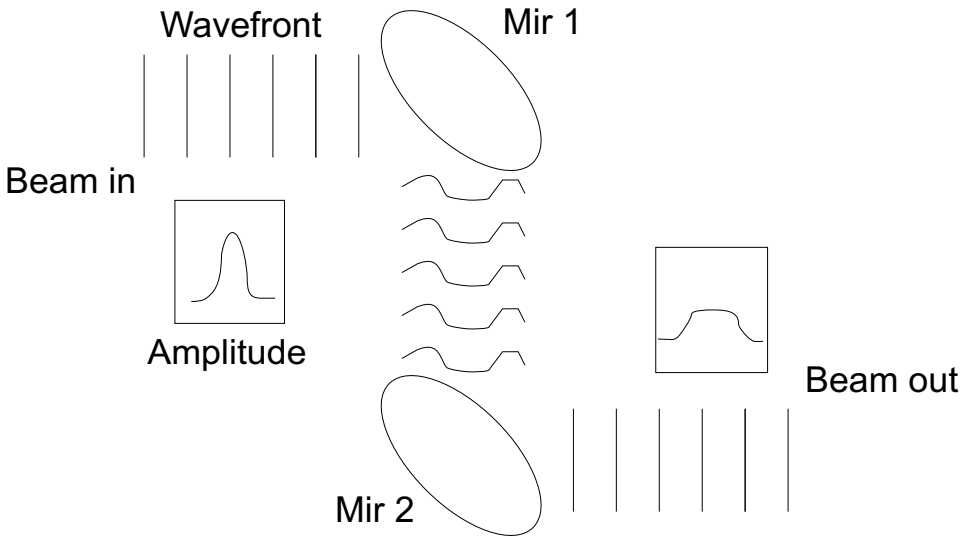

Figure 5.2: An incoming gaussian beam is flattened by using two deformable mirrors. The first mirror (placed at the beam waist of the beam) is shaped to defocusing the central area of the gaussian beam while focusing the external area. The second mirror is shaped inversely in order to flatten again the wavefront. The total effect is to flatten the amplitude profile.

We can generalize this system by using a couple of deformable mirrors with arbitrary shape (fig. 5.2). Consider a laser beam of arbitrary amplitude distribution, for simplicity at the waist position. If we give an arbitrary shape at the first mirror, we can calculate, knowing the distance d from the second mirror, the amplitude and phase distributions on the second mirror. At this point we can shape the surface of the second mirror so that the wavefront after the reflection is again flat. Therefore, the total effect of our system is to change arbitrary the amplitude distribution at the waist position. This is the simplest choice because a laser beam defined at waist is defined everywhere. Of course it is also possible to shape the wavefront, that is, to have a beam with different amplitude and phase distribution after the reflection on the second mirror.

Consider now the special case of transforming a gaussian beam in a FB. The first

mirror is shaped to defocusing the central area of the gaussian beam while focusing the external area. This can be done by giving to the mirror surface a total focusing shape plus a local defocusing shape in the central area (fig. 5.2). Instead the second mirror is shaped inversely in order to flatten again the wavefront. The total effect (after the second mirror) is to 'redistribute' radially the power of the beam, that is to flatten the amplitude profile.

As we saw in previous chapter the surface of a deformable mirror can be described by using Zernike Polynomials [52]. Moreover, there is a direct correspondence between Hermite-Gauss modes and Zernike Polynomials. By using this relation it is easy to add perturbations to the laser beam, as higher order Hermite-Gaussian modes, by driving the mirror surfaces with the Zernike Polynomials. Therefore, we need a representation of FB in terms of Hermite-Gauss modes.

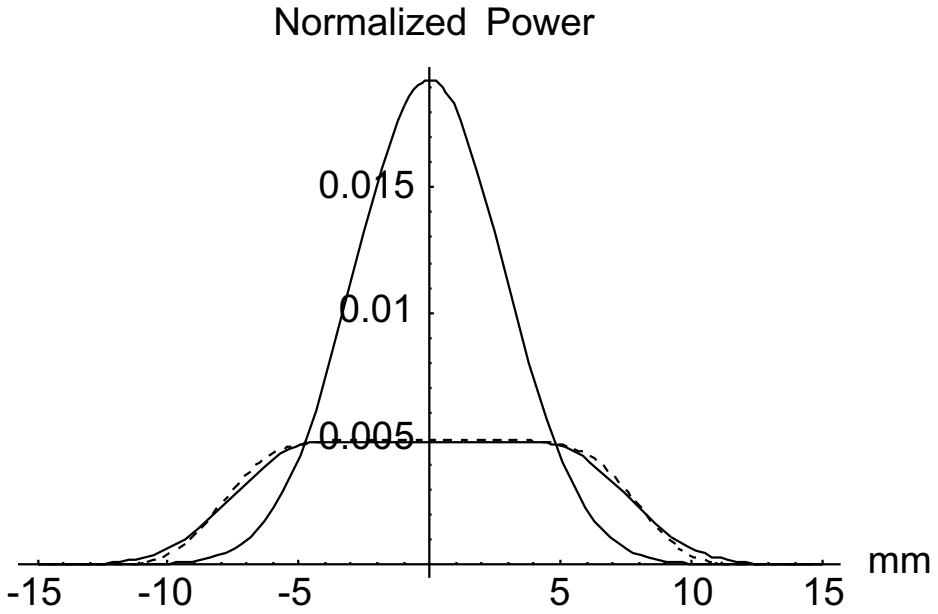

Figure 5.3: Initial gaussian beam and transformed flat beam [eq. 5.9] (solid line); exact flat beam [eq. 5.1](dashed line).

We can approximate a FB by superposing Hermite-Gauss modes with different beam waist w_0. In our case we limit the superposition only to second order modes. In particular, at waist position we can write the approximate beam $u_{app}(\vec{x})$ as:

$$\begin{aligned} u_{app}(\vec{x}) &= a\ \Phi_{00}(\vec{x}, v_0)+ \\ &+b\ \tfrac{1}{\sqrt{2}}(\Phi_{20}(\vec{x}, v_0) + \Phi_{02}(\vec{x}, v_0))+ \\ &+c\ \tfrac{1}{\sqrt{2}}(\Phi_{20}(\vec{x}, k_0) + \Phi_{02}(\vec{x}, k_0)) \end{aligned} \tag{5.9}$$

Where $\Phi_{mn}(\vec{x}, v_0)$ are Hermite-Gauss modes with beam waist v_0, $\Phi_{mn}(\vec{x}, k_0)$ are Hermite-Gauss modes with beam waist k_0 and (a,b,c) are the expansion coefficients. In fig. 5.3 is shown a normalized FB obtained with this superposition, the initial standard gaussian beam, and the exact FB obtained by equation 5.1. In order to evaluate the accuracy of this approximation we can calculate the overlap coefficient C between the two FB:

$$C = \int U_f^*(\vec{x}) U_{app}(\vec{x}) d\vec{x} = 0.994 \tag{5.10}$$

where $U_f(\vec{x})$ and $U_{app}(\vec{x})$ are the normalized fields corresponding respectively to $u_f(\vec{x})$ and $u_{app}(\vec{x})$.

The value of C obtained assures us that we can have a good approximation of a FB, at less of 0.6%, by using only low order gaussian modes, in particular up to second order. If we consider that the Zernike polynomials associated to the defocusing (and focusing) of the mirror surfaces are of second order, it results that we can generate

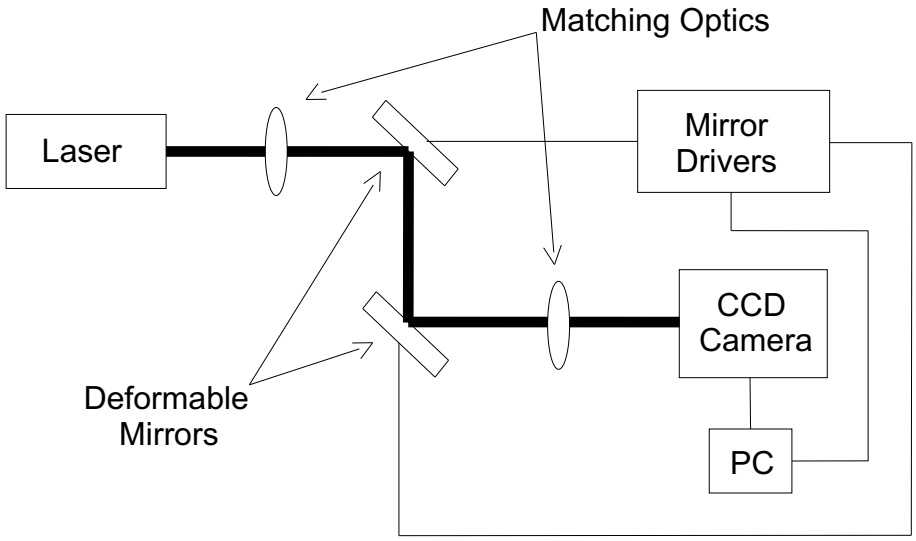

Figure 5.4: Experimental apparatus.

a FB only by adding focusing and defocusing terms to the mirror surfaces. The feasibility of this technique has been tested by using the experimental apparatus schematically shown in fig. 5.4. The initial gaussian beam is a 10 mW He-Ne laser. A lens is used to match the beam waist on the first deformable mirror. After the second deformable mirror the beam is focused on a 8 bit CCD camera, the frame is read by a PC and the signals are analyzed with Matlab routines. The mirrors are the micromachined membrane deformable mirrors described in par. 4.4.3.

5.5 Results and discussion

In fig. 5.5 is shown the power profile of the first FB generated with this prototype system. A comparison between the data and the theoretical model is shown in fig. 5.6, the coupling between the two beams is about 99%. The beam presents residual aberrations, these aberrations can be generated by different effects, the first one is a non perfect alignment of the two mirrors and a non perfect matching of the input

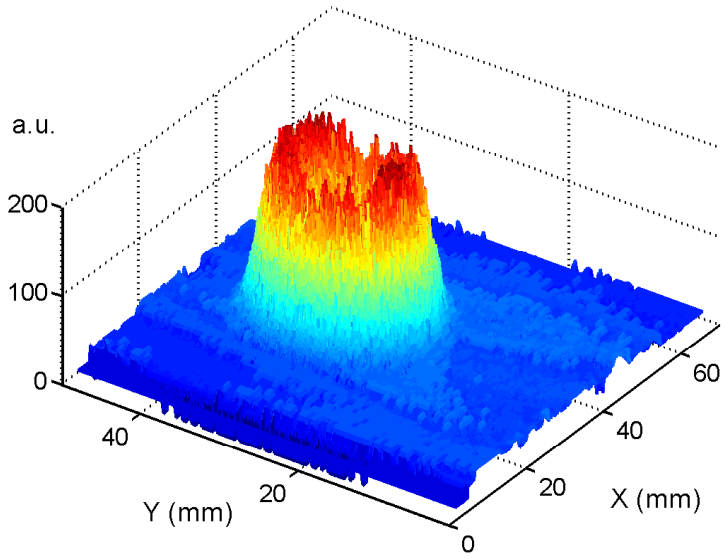

Figure 5.5: 3D power profile of flat beam generated with two deformable mirrors.

beam on the first mirror. Moreover, a non optimal diagonalization of the actuators matrix of the mirrors, can generates a coupling of higher order modes.

Finally, as we saw in th previous chapter, the membrane deformable mirrors used must work pre-tensioned due to the fact that the electrostatic force between the electrodes and the metallic membrane is always attractive, this cause intrinsic mirror aberrations which degrade the reflected beams. In order to improve the performances of the system it could be used the piezoelectric deformable mirrors, which have higher optical quality. Moreover, an automation of the system need to be studied, especially for the centering of the beam and for the alignment of the mirrors. Nevertheless, even if the system is not yet optimized, the results demonstrate the feasibility of such technique to generate flat beams. If the further tests with high power laser and in closed-loop (to match the beam to Mexican-Hat Fabry-Perot cavity) will be positive, this technique could be used for the future generation of gravitational

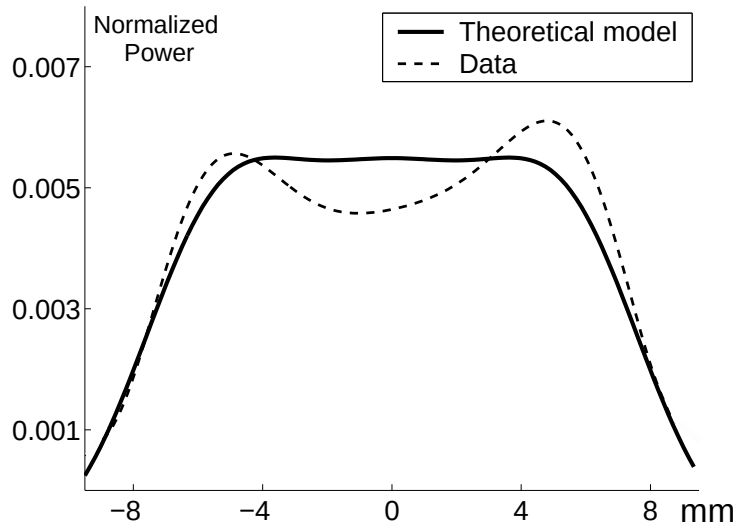

Figure 5.6: Comparison between the data (dashed line) and the theoretical model (solid line). The coupling is about 99%.

waves interferometers if they will be equipped with flat beams and Mexican-Hat mirrors Fabry-Perot cavities.

Chapter 6

Scanning wavefront sensor for the analysis of thermal deformation effects of the Virgo mirrors

6.1 Thermal compensation problem

As we saw in Chapter 2, one of the fundamental noise which limit the sensitivity of gravitational wave interferometers, for frequency higher than about 300-400 Hz, is the shot-noise. To lower such noise, high power lasers (10-20 Watts) and recycling techniques are typically used. Moreover, in order to still reduce the shot noise, it has been foreseen to use higher power lasers (hundreds of Watts) for the advanced detectors.

Unfortunately the use of high power laser presents serious problems, due to the non zero absorption coefficient of the mirrors. Absorption in the coating and in the substrate of the optics causes a local heating and consequently a geometric deformation, producing a wavefront deformation of the reflected and transmitted beams. Moreover, the variation of temperature causes a variation of the refractive index of the material which produces *thermal lensing* effects [68, 69]. The are two main effects on the interferometer operation. The first one is a non perfect interference at

the output of the interferometer without improving the sensitivity but, on the contrary, increasing the phase noise. The second one is a degradation of the sidebands resonating in the recycling cavity (which can totally lose the resonant condition) compromising the control of the interferometer [70, 71].

Different solutions have been proposed in order to actively compensate these thermal effects. In particular, the most important, and not invasive, is heating the *cold* parts of the mirror by means of heating ring (for gross corrections) or high power laser with properly wavelength so to be totally absorbed by the materials of the mirrors (fine corrections) [70, 71, 72].

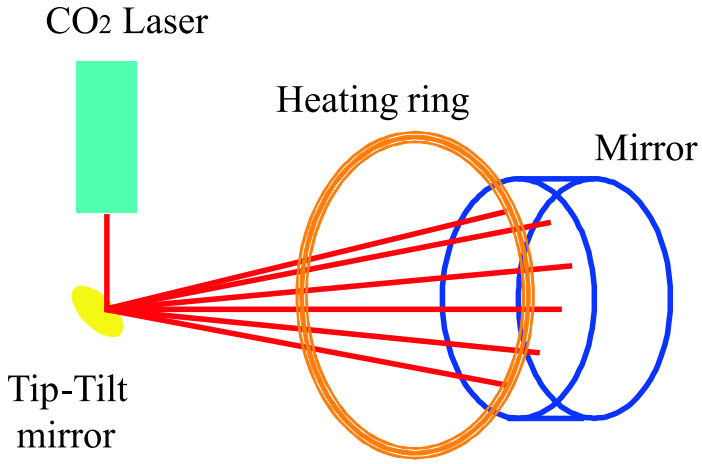

Figure 6.1: Thermal compensation techniques.

As shown in fig. 6.1 a heating ring can be placed near the mirror in order to heat the external cold parts, being the central part warmer since crossed by the laser beam. In the same way a CO_2 laser (10 micron) can be used to heat locally the mirror. In the case of Virgo the fused silica mirrors become opaque for wavelength higher than a few micron then absorbing almost all the laser power.

Considering the Virgo mirrors design specifics it can be possible to do a simple

estimation of the effects of thermal induced deformations on the interferometer sensitivity. It is possible to take into account these thermal effects by considering the changes in the shot noise limited sensitivity [73]:

$$\delta h_{shot} \approx \left\{ \frac{1}{P^c_{PRC}} + 16 \frac{C_d}{\Gamma^2} P^c_{PRC} \left[1 + C_c \left(P^c_{PRC} \right)^2 \right]^2 \right\}^{1/2} \tag{6.1}$$

where P^c_{PRC} is the carrier power in the recycling cavity, Γ is the modulation deep of the input beam, C_d and C_c are coefficients depending by the induced aberrations in the mirrors.

In the case of Virgo it can be found that at a typical frequency of 100 *Hz*, for a 10 Watts power input laser, the phase noise remains essentially unchanged, while for a 100 Watts power input laser, as foreseen for advanced detectors, there is a strong increasing (fig. 6.2).

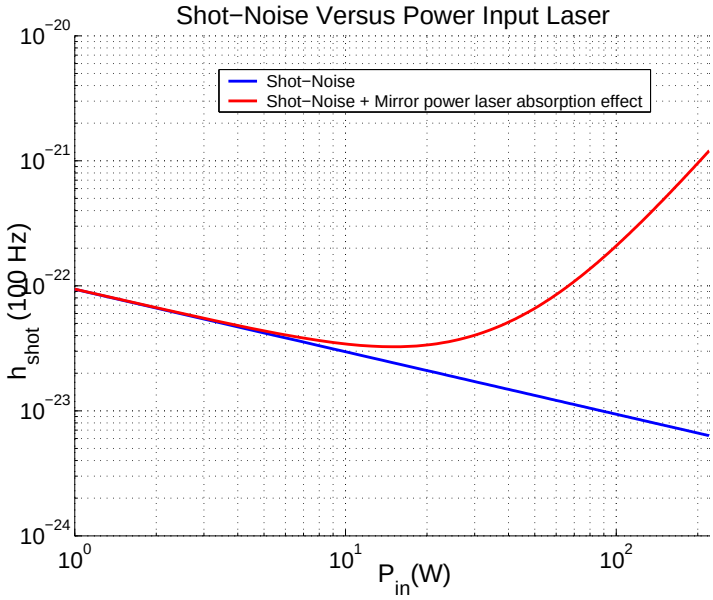

Figure 6.2: Shot noise limited sensitivity (with and without thermal effects) at 100 Hz for different powers of input laser beam.

Then, in the actual state (10 Watts power input laser) the Virgo interferometer should not presents thermal effects. Unfortunately, thermal effects have been recently observed. In particular, a decrease of carrier and, especially, sidebands power have been observed during the first minutes of lock (fig. 6.3).

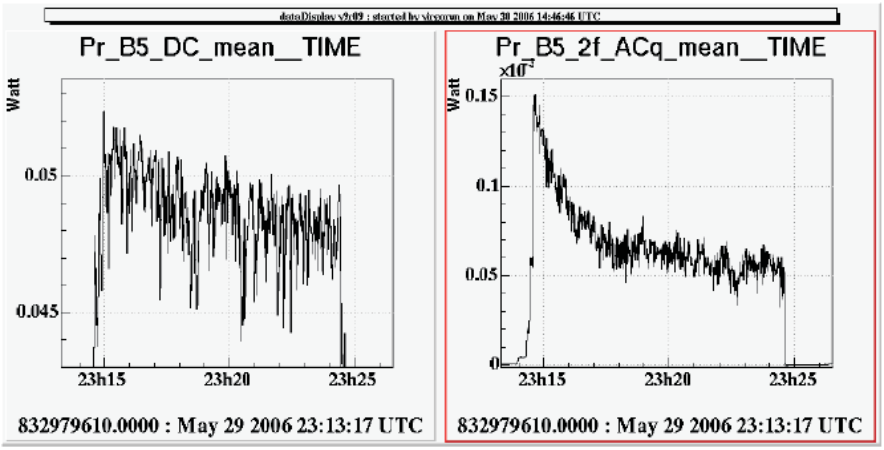

Figure 6.3: Carrier power (left) and sidebands power (right) over about 15 minutes of lock.

A finite element modeling (FEM), developed ad hoc with Matlab, explained this effect as a thermal lensing in the input mirrors. A possible explanation is that the absorption in the mirrors is larger than the nominal value considered in the design of the detector. For this reason, it arises the necessity to develop a wavefront system to analyze the fields geometry of both the carrier and the sidebands inside the interferometer, in order to study and detect thermal deformation effects in the Virgo optics. In particular, as described in the next paragraph, we need first to study the effects of these thermal effects over the fields inside the interferometer, so to understand the signals to use for the wavefront reconstruction, then we can study the wavefront system for the reconstruction.

6.2 Wavefront signal extraction

Here is reported a calculation of the wavefront signals reconstruction at the dark port (DP) and pick-off port (BS) of the Virgo interferometer. The fields inside the interferometer are recalled to clarify the approximation used. The signals in DP and BS are calculated first in the ideal case, than in the not ideal case of input mirrors aberrations.

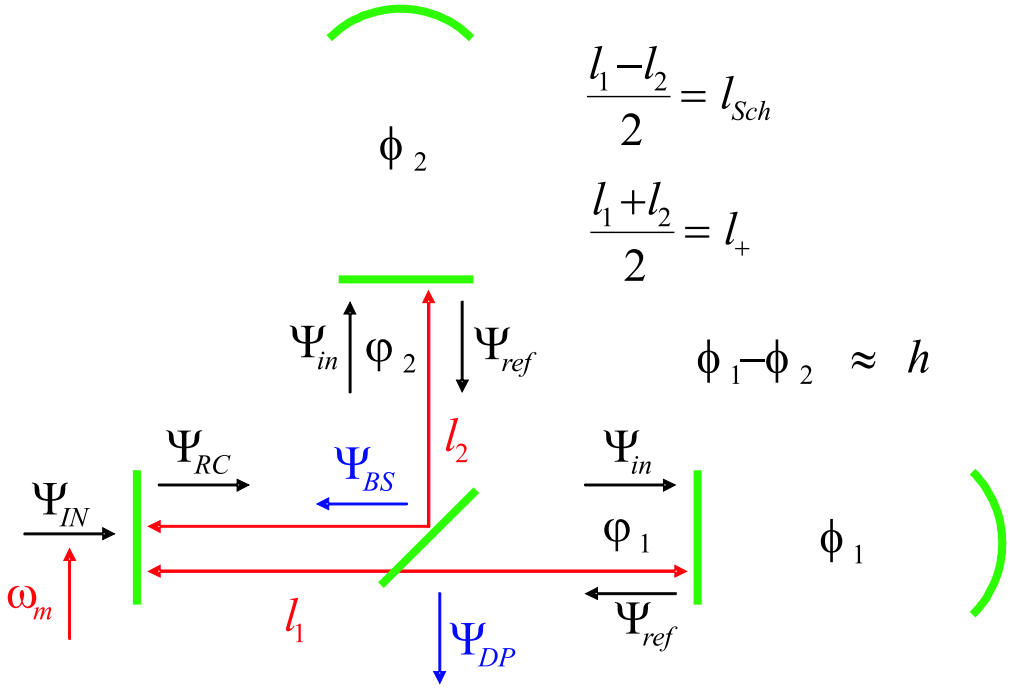

Figure 6.4: Fields inside the interferometer.

6.2.1 Signals in DP and BS in the ideal case and introduction to approximations

The notation of the fields inside the interferometer is reported in fig. 6.4. [74]. The field Ψ_{IN} is the result of the phase modulation of the input laser beam $E_L = E_0 e^{i\omega t}$.

It can be written as a superposition of carrier and sidebands:

$$\Psi_{IN} = E_0 e^{i(\omega t + m\, cos\omega_m t)} = \sum_{-\infty}^{+\infty} \Psi_{IN}^n \tag{6.2}$$

where m is the modulation depth and the ω_m is the modulation frequency. Each sideband is thus:

$$\Psi_{IN}^n = E_L[i^{|n|} J_{|n|}(m) e^{inw_m t}] \tag{6.3}$$

In this way each sideband is indicated with the integer n and the carrier can be also indicate as the zero-order sideband.

Now we can calculate the fields inside the interferometer, considering the sidebands order up to n=2 [75]. With the notation of fig 6.4 the field reflected by the arms is:

$$\Psi_{ref} \approx \Psi_{ref}^{CR} + \Psi_{ref}^{+1} + \Psi_{ref}^{-1} + \Psi_{ref}^{+2} + \Psi_{ref}^{-2} \tag{6.4}$$

The carrier field reflected by the arm 1,2 is:

$$\Psi_{ref1,2}^{CR} \approx \Psi_{in}^{CR}[1 + \frac{2iF}{\pi}\phi_{1,2} - \frac{F}{\pi}\eta_{1,2}] \tag{6.5}$$

The sidebands reflected fields are:

$$\Psi_{ref1,2}^{\pm 1,2} \approx -\Psi_{in}^{\pm 1,2} e^{i\theta_{1,2}^{\pm 1,2}(x,y)} \tag{6.6}$$

here the superscript 1,2 refers to the sidebands while the subscript 1,2 refers to the arms of interferometer, the term $\theta_{1,2}^{\pm 1,2}(x,y)$ take into account the aberrations eventually acquired by the sidebands. The reflectivity of the mirror is approximated to unity. It is useful to express the fields with the field in the recycling cavity. So just before recombining at the beam splitter the carrier field is:

$$\Psi_{ref1,2}^{CR} \approx \frac{1}{\sqrt{2}} \Psi_{RC}^{CR}[1 + \frac{2iF}{\pi}\phi_{1,2} - \frac{F}{\pi}\eta_{1,2}] e^{2i\omega(L_+ \pm L_{Sch})} \tag{6.7}$$

the 1 omega sidebands in the arm 1 are:

$$\Psi_{ref1}^{\pm 1} \approx -\frac{1}{\sqrt{2}} \Psi_{RC}^{\pm 1} e^{2i(\omega \pm \omega_m)(L_+ + L_{Sch})} e^{i\theta_1^{\pm 1}(x,y)} \tag{6.8}$$

while the 1 omega sidebands in the arm 2 are:

$$\Psi_{ref2}^{\pm 1} \approx -\frac{1}{\sqrt{2}} \Psi_{RC}^{\pm 1} e^{2i(\omega \pm \omega_m)(L_+ - L_{Sch})} e^{i\theta_2^{\pm 1}(x,y)} \tag{6.9}$$

where $L_{Sch} = \frac{(L_1 - L_2)}{2}$ and $L_+ = \frac{(L_1 + L_2)}{2}$ indicate the Schnupp and the Recycling lengths respectively. In the same way we can write the fields for the sidebands $|n| = 2$. Before to consider the aberrations we recall the ideal optical conditions. Thus we impose dark fringe condition for the carrier at the output port $2\omega L_{Sch} = 2n\pi$ and carrier resonance condition in the recycling cavity $2\omega L_+ = 2n\pi$. Up to now we have expressed all the fields in function of the field inside recycling cavity. This is the best procedure in our case because the measurements in DP and BS are indeed a measurement of the field in this cavity. Nevertheless it can be useful to express these fields starting from the fields Ψ_{IN} of the beam entering the interferometer. If t_{RM} and r_{RM} indicate the transmittivity and reflectivity of the recycling mirror, we can write the fields in the recycling cavity as:

$$\Psi_{RC}^{CR} = \frac{t_{RM}}{1 - r_{RM}} \Psi_{IN}^{CR} \tag{6.10}$$

$$\Psi_{RC}^{\pm 1} = \frac{t_{RM}}{1 + r_{RM} \cos \frac{2\omega_m L_{Sch}}{c} e^{\pm 2i\omega_m L_+/c}} \Psi_{IN}^{\pm 1} \tag{6.11}$$

$$\Psi_{RC}^{\pm 2} = \frac{t_{RM}}{1 + r_{RM} \cos \frac{2\omega_m L_{Sch}}{c} e^{\pm 4i\omega_m L_+/c}} \Psi_{IN}^{\pm 2} \tag{6.12}$$

The resonant condition for $|n| = 1$ sidebands is:

$$2\omega_m L_+/c = (2n+1)\pi \tag{6.13}$$

and all the $|n| = 1$ sidebands exit the dark port if:

$$\cos \frac{2\omega_m L_{Sch}}{c} = r_{RM} \tag{6.14}$$

This condition make not-resonant the $|n| = 2$ (and even) sidebands and resonant all the odds. It is now possible to express the field at the dark port and the pick-off port, in this case the reflected field in arm 1 from the beam-splitter.
The field at the DP is (c=1):

$$\begin{aligned}\Psi_{DP} = \frac{1}{2}\Psi_{RC}^{CR}[\frac{2iF}{\pi}(\phi_2 - \phi_1) - \frac{F}{\pi}(\eta_2 - \eta_1)]+ \\ -i\hat{\Psi}_{RC}^{+1}e^{i\omega_m t}\sin(2\omega_m L_{Sch})+ \\ +i\hat{\Psi}_{RC}^{-1}e^{-i\omega_m t}\sin(2\omega_m L_{Sch})\end{aligned} \tag{6.15}$$

While the field at pick-off port BS is given by:

$$\Psi_{BS} = \frac{1}{\sqrt{2}}\left\{\Psi_{RC}^{CR}[1 + \frac{2iF}{\pi}\phi_1 - \frac{F}{\pi}\eta_1] - \hat{\Psi}_{RC}^{\pm 1}e^{\pm i\omega_m t} - \hat{\Psi}_{RC}^{\pm 2}e^{\pm 2i\omega_m t}\right\} \tag{6.16}$$

Where the time dependence of the signals is evidenced by indicating $\Psi^n = \hat{\Psi}^n e^{in\omega t}$. Having discussed the main conditions regulating the work of the interferometer we can now recover the signals at the two ports at the 1-omega demodulation frequency. Just to simplify the calculations we remember that in general the signal is:

$$|\Psi|_{\omega_m}^2 = (a + ib)e^{-i\omega_m t} + (a - ib)e^{i\omega_m t} \tag{6.17}$$

so that

$$|\Psi|_{\omega_m}^2 = 2Re(a + ib)cos(\omega_m t) - 2Im(a - ib)sin(\omega_m t) \tag{6.18}$$

and this makes it convenient to calculate the quantity N=(a+ib) and finally write:

$$|\Psi|_m^2 = 2Re(N)cos(\omega_m t) + 2Im(N)sin(\omega_m t) \tag{6.19}$$

In the ideal case the sidebands remain imaginary with respect to the carrier, so that we can continue to assume that:

$$\hat{\Psi}_{RC}^{+1} = \hat{\Psi}_{RC}^{-1} \propto i\hat{\Psi}_{RC}^{CR} \tag{6.20}$$

We expect that this condition will be changed by aberrations. If we calculate the quantity N_{DP} we can found that:

$$N_{DP} \propto \frac{1}{2} sin(2\omega_m L_{Sch}) \left[\frac{4iF}{\pi} (\phi_1 - \phi_2) \right] \tag{6.21}$$

As expected N_{DP} is imaginary, then the quadrature signal is:

$$S_{DPq} = 2Im(N) sin(\omega_m t) \propto \frac{1}{2} sin(\vartheta) \left[\frac{8iF}{\pi} (\phi_1 - \phi_2) \right] \tag{6.22}$$

where $\vartheta = 2\omega_m L_{Sch}$. It is proportional only to the gravitational signal while, as expected, the in-phase signal $2Re(N_{DP})cos(\omega_m t)$ is equal to zero.
In the same way, for the pick-off signal, if we suppose that (in the ideal case) the sidebands are imaginary and perfectly superposed to the carrier, we obtain:

$$N_{BS} \propto \frac{1}{2} \left\{ \frac{4F}{\pi} \phi_1 \right\} \tag{6.23}$$

As expected it is real, so the signal proportional to the phase difference between carrier and sidebands is recovered by the in-phase signal:

$$S_{BSI} = 2Re(N_{BS}) cos(\omega_m t) \propto \frac{1}{2} \left\{ \frac{8F}{\pi} \phi_1 \right\} cos(\omega_m t) \tag{6.24}$$

while the quadrature signal is equal to zero.

6.2.2 Signals in DP and BS in the not ideal case of input mirrors aberrations

We first consider the DP signal, which is a bit less evident then the BS signal. Here we repeat the derivation already seen for the ideal case considering the effects due to the aberrations. As we saw, we can consider the mirrors aberrations by introducing the phases $\theta_{1,2}^{\pm 1}(x,y)$ acquired by the sideband ± 1 in reflection in the arm 1,2. Tacking into account these phases the DP signal can be written as:

$$\begin{aligned}\Psi_{DP} = -\frac{1}{2}\Bigg\{ & \Psi_{RC}^{CR}\left[1+\frac{2iF}{\pi}\phi_1-\frac{F}{\pi}\eta_1\right]e^{2i\omega(L_++L_{Sch})}+ \\ & -\Psi_{RC}^{+1}e^{i\theta_1^{+1}(x,y)}e^{2i(\omega+\omega_m)(L_++L_{Sch})}-\Psi_{RC}^{-1}e^{i\theta_1^{-1}(x,y)}e^{2i(\omega-\omega_m)(L_++L_{Sch})}+ \\ & -\Psi_{RC}^{CR}\left[1+\frac{2iF}{\pi}\phi_2-\frac{F}{\pi}\eta_2\right]e^{2i\omega(L_+-L_{Sch})}+ \\ & +\Psi_{RC}^{+1}e^{i\theta_2^{+1}(x,y)}e^{2i(\omega+\omega_m)(L_+-L_{Sch})}+\Psi_{RC}^{-1}e^{i\theta_2^{-1}(x,y)}e^{2i(\omega-\omega_m)(L_+-L_{Sch})}\Bigg\}\end{aligned} \tag{6.25}$$

If we ignore the minus sign and the common phase term $e^{2i\omega L_+}$, imposing the dark fringe condition $2\omega L_{Sch} = 2n\pi$ we have:

$$\begin{aligned}\Psi_{DP} = \frac{1}{2}\Bigg\{ & \Psi_{RC}^{CR}\left[\frac{2iF}{\pi}(\phi_1-\phi_2)-\frac{F}{\pi}(\eta_1-\eta_2)\right]+ \\ & -\Psi_{RC}^{+1}e^{i\theta_1^{+1}(x,y)}e^{2i\omega_m L_{Sch}}e^{2i\omega_m L_+}-\Psi_{RC}^{-1}e^{i\theta_1^{-1}(x,y)}e^{-2i\omega_m L_{Sch}}e^{-2i\omega_m L_+}+ \\ & +\Psi_{RC}^{+1}e^{i\theta_2^{+1}(x,y)}e^{-2i\omega_m L_{Sch}}e^{2i\omega_m L_+}+\Psi_{RC}^{-1}e^{i\theta_2^{-1}(x,y)}e^{-2i\omega_m L_{Sch}}e^{-2i\omega_m L_+}\Bigg\}\end{aligned} \tag{6.26}$$

Now we can suppose that the mean phases are equal to zero in reflection. This seems reasonable in that it should be just a rescaling of L_{Sch}. With this condition true the conditions for resonance of sidebands are the usual $2\omega_m L_+ = (2n+1)\pi$ and the field at the dark port can be written as:

$$\Psi_{DP} = \frac{1}{2}\left\{\Psi_{RC}^{CR}\left[\frac{2iF}{\pi}(\phi_1-\phi_2)-\frac{F}{\pi}(\eta_1-\eta_2)\right]+\right.$$
$$+\Psi_{RC}^{+1}e^{i\theta_1^{+1}(x,y)}e^{2i\omega_m L_{Sch}}+\Psi_{RC}^{-1}e^{i\theta_1^{-1}(x,y)}e^{-2i\omega_m L_{Sch}}+$$
$$\left.-\Psi_{RC}^{+1}e^{i\theta_2^{+1}(x,y)}e^{-2i\omega_m L_{Sch}}-\Psi_{RC}^{-1}e^{i\theta_2^{-1}(x,y)}e^{2i\omega_m L_{Sch}}\right\} \tag{6.27}$$

The phases can be divided in a common and differential phase such that $\theta_1^{\pm1}(x,y) = \theta_C^{\pm1}(x,y)+\theta_D^{\pm1}(x,y)$ and $\theta_2^{\pm1}(x,y) = \theta_C^{\pm1}(x,y)-\theta_D^{\pm1}(x,y)$. After some algebra we have:

$$\Psi_{DP} = \frac{1}{2}\left\{\Psi_{RC}^{CR}\left[\frac{2iF}{\pi}(\phi_1-\phi_2)-\frac{F}{\pi}(\eta_1-\eta_2)\right]+\right.$$
$$+2i\hat{\Psi}_{RC}^{+1}e^{i\theta_C^{+1}(x,y)}e^{i\omega_m t}\sin\left(2\omega_m L_{Sch}+\theta_D^{+1}(x,y)\right)+$$
$$\left.-2i\hat{\Psi}_{RC}^{-1}e^{i\theta_C^{-1}(x,y)}e^{-i\omega_m t}\sin\left(2\omega_m L_{Sch}+\theta_D^{-1}(x,y)\right)\right. \tag{6.28}$$

Now we consider that the sidebands are affected in the same way by reflection and impose $\theta_C^{+1}(x,y) = -\theta_C^{-1}(x,y) = \theta_C(x,y)$ and $\theta_D^{+1}(x,y) = -\theta_D^{-1}(x,y) = \theta_D(x,y)$. Of course here we are neglecting the effects of differences in sidebands.

In this way we can write:

$$\Psi_{DP} = \frac{1}{2}\left\{\Psi_{RC}^{CR}\left[\frac{2iF}{\pi}(\phi_1-\phi_2)-\frac{F}{\pi}(\eta_1-\eta_2)\right]+\right.$$
$$+2i\hat{\Psi}_{RC}^{+1}e^{i\theta_C(x,y)}e^{i\omega_m t}\left[\sin(2\omega_m L_{Sch})\cos(\theta_D(x,y))+\cos(2\omega_m L_{Sch})\sin(\theta_D(x,y))\right]$$
$$\left.-2i\hat{\Psi}_{RC}^{-1}e^{-i\theta_C(x,y)}e^{-i\omega_m t}\left[\sin(2\omega_m L_{Sch})\cos(\theta_D(x,y))-\cos(2\omega_m L_{Sch})\sin(\theta_D(x,y))\right]\right\} \tag{6.29}$$

The sidebands are almost imaginary with respect to carrier so that it is convenient to write them as: $\hat{\Psi}_{RC}^{\pm1} = i\hat{\Psi}_{RC}^{\pm1}$. An eventual common phase of the two carrier can be considered comprised in $\theta_C(x,y)$. So we can calculate N_{DP}:

$$N_{DP} = [\cos(\theta_C(x,y)) - i\sin(\theta_C(x,y))]$$

$$\left\{\left[\frac{-4iF}{\pi}\left(\phi_1-\phi_2\right)\right]\sin(\vartheta)\cos\left(\theta_D(x,y)\right)+\left[\frac{2F}{\pi}\left(\eta_1-\eta_2\right)\right]\cos(\vartheta)\sin\left(\theta_D(x,y)\right)\right\} \tag{6.30}$$

The real part of N_{DP} is equal to:

$$\begin{aligned} Re(N_{DP}) = \Bigg\{&\cos(\theta_C(x,y))\cos(\vartheta)\sin\left(\theta_D(x,y)\right)\left[\frac{2F}{\pi}\left(\eta_1-\eta_2\right)\right]+ \\ &-\sin(\theta_C(x,y))\sin(\vartheta)\cos\left(\theta_D(x,y)\right)\left[\frac{4F}{\pi}\left(\phi_1-\phi_2\right)\right]\Bigg\} \end{aligned} \tag{6.31}$$

and in the same way, for $Im(N_{DP})$ it can be found:

$$\begin{aligned} Im(N_{DP}) = -\Bigg\{&\cos(\theta_C(x,y))\sin(\vartheta)\cos\left(\theta_D(x,y)\right)\left[\frac{4F}{\pi}\left(\phi_1-\phi_2\right)\right]+ \\ &\sin(\theta_C(x,y))\cos(\vartheta)\sin\left(\theta_D(x,y)\right)\left[\frac{2F}{\pi}\left(\eta_1-\eta_2\right)\right]\Bigg\} \end{aligned} \tag{6.32}$$

These are the most important expressions to observe to understand what signal can be interesting for our purpose. The signal proportional to the $Im(N_{DP})$ is in quadrature with respect to the modulation signal and it is called in Virgo "In Phase" for historical reasons and it is the signal of the gravitational wave. On the opposite, what is called "In quadrature" is the signal proportional to $Re(N_{DP})$ which is in phase with the modulation signal.

For what concerns the signal that can be taken at the pick-off port the situation is much more clear. We can write the signal at the modulation frequency following the previous approximations, imposing that $\theta_1^{+1}(x,y) = -\theta_1^{-1}(x,y) = \theta_1$ and neglecting the loss $\frac{F}{\pi}\eta$ respect to unity. With these considerations N_{BS} is given by:

$$N_{BS} = -\frac{1}{2}\left\{2Re\left[\hat{\Psi}_{RC}^{CR}\left(\hat{\Psi}_{RC}^{+1}\right)^*\right]+\frac{4F}{\pi}\phi_1 Im\left[\hat{\Psi}_{RC}^{CR}\hat{\Psi}_{RC}^{+1}\right]\right\}e^{-i\theta_1(x,y)} \tag{6.33}$$

The signal in phase with the modulation signal is:

$$S_{BSI} = 2Re(N_{BS})\cos(\omega_m t) =$$

$$= -\frac{1}{2}\left\{2Re\left[\hat{\Psi}_{RC}^{CR}\left(\hat{\Psi}_{RC}^{+1}\right)^*\right] + \frac{4F}{\pi}\phi_1 Im\left[\hat{\Psi}_{RC}^{CR}\hat{\Psi}_{RC}^{+1}\right]\right\}\cos[\theta_1(x,y)]\cos(\omega_m t) \quad (6.34)$$

While the signal in quadrature with the modulation signal is:

$$S_{BSq} = 2Im(N_{BS})\sin(\omega_m t) =$$

$$= \frac{1}{2}\left\{2Re\left[\hat{\Psi}_{RC}^{CR}\left(\hat{\Psi}_{RC}^{+1}\right)^*\right] + \frac{4F}{\pi}\phi_1 Im\left[\hat{\Psi}_{RC}^{CR}\hat{\Psi}_{RC}^{+1}\right]\right\}\sin(\theta_1(x,y))\sin(\omega_m t) \quad (6.35)$$

From this equation it is recalled that at the modulation frequency the main in-phase signal is the phase difference between carrier and sidebands. (We remember that sidebands are presently taken to be equal). This is the signal that seems the best to recover aberrations of the sidebands with respect to the carrier.

We can conclude that the signal at 1 omega can be used as a measurement of the ($|n| = 1$) sidebands wavefront aberrations easily in the pick-off port and, with some more difficulties, from the DP quadrature signal. It can be shown that if the sidebands are not equal or are phase shifted one with respect to the other a signal in quadrature arise at the double of the modulation frequency that could be considered eventually as an error signal for their differences.

From these considerations it follows that in order to analyze the effects of the mirrors thermal deformations on the fields inside the interferometer, we need to develop a wavefront sensor which is able to acquire beams images at least at the modulation frequency of the input beam.

6.3 Scanning wavefront sensor

The first idea for the wavefront sensor has been, of course, to use a photodiode array as described in chapter 4. Unfortunately, for technical problems it was not possible to do it. In fact, first it was necessary a customized photodiode array in the infrared region (for the laser beam used in Virgo), second it was necessary to develop a customized electronics for the simultaneous demodulation of 16 photodiode signals. Then, in order to reduce time and costs, it has been decided to start with a simplest solution based on a scanning pin-hole system, postponing the photodiode array solution later. In particular, the scanning pin-hole system allows to use only one photodiode and only one demodulation board (already available in the Virgo framework).

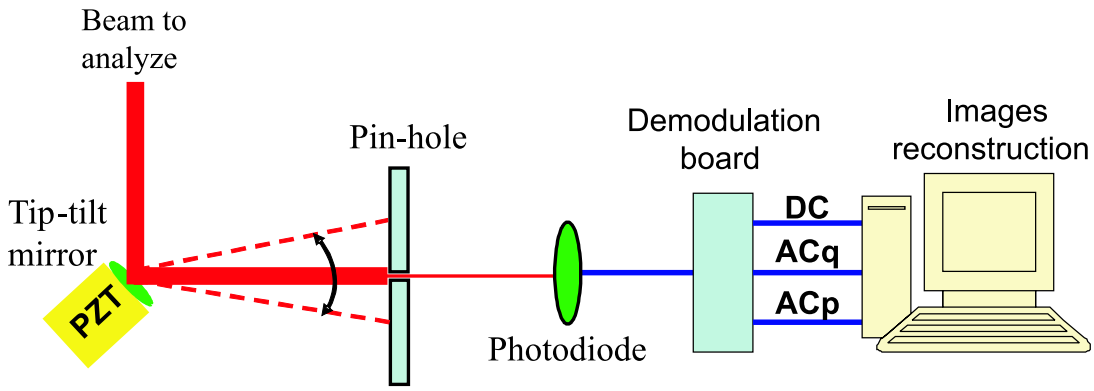

Figure 6.5: Scanning wavefront system set-up.

The scanning wavefront system developed is shown in fig. 6.5. The laser beam to be analyzed is steered to a tip-tilt piezoelectric mirror (PZT), the beam is reflected onto a pin-hole (with diameter smaller than beam diameter) and is acquired by a photodiode. The photodiode signal is demodulated to obtain the DC, the AC in-

quadrature (ACq) and the AC in-phase (ACp) signals. The PZT mirror is driven in order to scan the beam on the pin-hole, scanning pattern being a spiral. The point-to-point image detection allows to reconstruct the DC, ACq, ACp images of the beam.

As described the wavefront analysis is performed on the recombining beam at the dark-port (DP) and at the pick-off port (BS). The total space available for the system on the Virgo detection bench is about 20x10x10 cm^3 and the beam waist is about 800 micron (in this case the pin-hole diameter is 50 μm). This implies that the transversal range is about 3 mm, to be obtained driving the mirror at a distance of about 10 cm. The required total time to obtain a wavefront image is a few seconds as it is expected that the major aberrations will be given by very low frequency thermal drifts. Thus the mirror requirements are:

- Mirror mechanical rotation range: the beam must be transversally moved by about 3 mm. The maximum available distance L between the rotating mirror and the pin-hole will be about L =10 cm, so that the maximum angular range θ, given by $2\theta L = 3 \times 10^{-3} m$, must be $\theta \geq 15 mrad$.

- Bandwidth: the total time required to acquire an image is few seconds, as it is expected to be sufficient in analyzing the long term aberrations produced by long term drift. Considering that the total number of data taken in one second can be maximum 20×10^3 (Virgo sampling rate), a bandwidth of about 50 Hz is required if all the image is to be taken in one second.

- Minimum mirror diameter : the beam waist is 800 μm on the mirror, so that a 10 mm diameter is more than sufficient. This allows to choose a scanning system supporting a light weight.

- Repeatability/hysteresis : the important requirement here is the measurability of the angle of the mirror at a given data taken from the photodiode.

6.4 Characterization of the PZT tip-tilt mirror

Following the above requirements, a characterization of a tip-tilt selected mirror has been performed. The tested PZT system is a Ultra-Long-Range Piezo Tip/Tilt Mirror, model S-334-2SL, from Physics Instrument (PI).

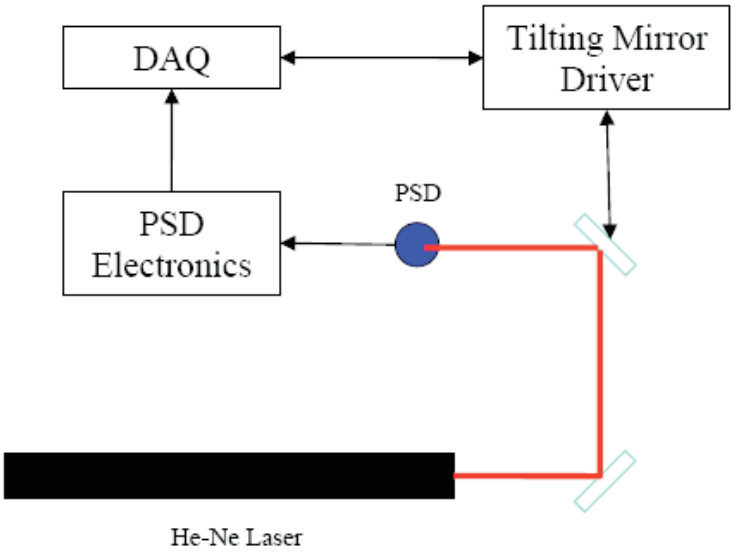

Figure 6.6: Scheme of the experimental set-up.

The experimental set-up was formed by a 1.5 mW HeNe laser, emitting at 543.5 *nm*, an auxiliary mirror that steers the beam on the tilting mirror, a 2D position sensing photodiode, model 2044 from Hamamatsu, with an home made front-end electronics, and a digital DAQ system used to acquire the data coming from the PSD front-end, as well as to send the driving voltages to the tilting mirror drivers.

In fig. 6.6 a schematic of the experimental set-up is shown. The distance between the tilting mirror and the PSD was 10 *cm*. The sampling frequency used to perform all the measurement, with this set-up, was 1 *kHz*. The front end electronics was designed to provide for the not normalized asymmetries, in both x and y degrees of freedom, and the total power on the PSD.

6.4.1 Characterization of the PSD readout

The measurement system was characterized by performing a calibration of the PSD response and a transfer function of the PSD front-end electronics. The calibration was performed by using a fixed mirror instead of the tilting one and by moving the PSD, placed on a high precision XY translator, by a known amount of steps. The results of these measurements are summarized in fig. 6.7. In both the figures the points are the measured values and the solid line is the linear fit.

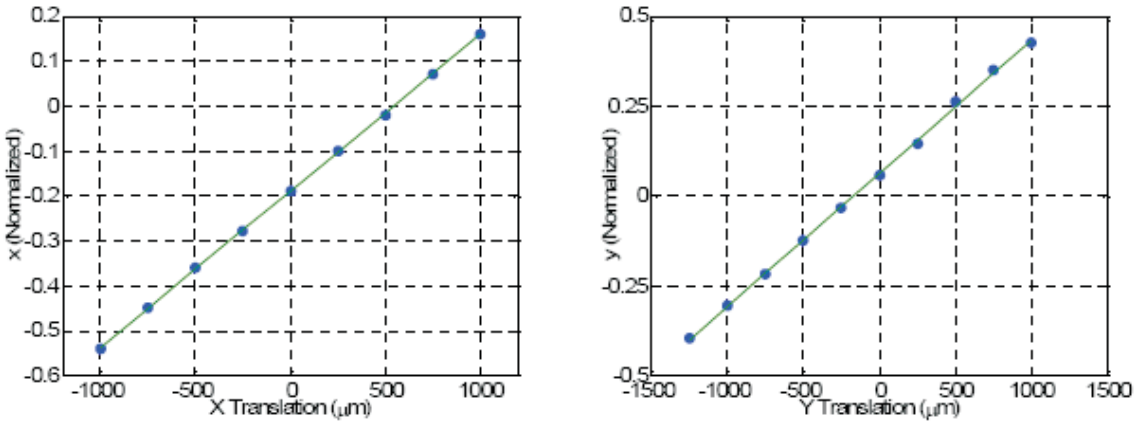

Figure 6.7: Calibration of the PSD device, x and y axis.

The resulting calibration factors are Cx=2873 μm for the x axis and Cy=2699 μm for the y axis. Since these values are very similar, it has been chosen a single calibration

factor for both the axis: C=2800 μm. The transfer function measurement of the PSD read-out was performed by sending a white noise voltage signal, digitally filtered with a 4 poles, 10 Hz filter, to the front-end electronics input, through 4 nominally equal resistors. To perform the xTF measurement the resistors were coupled in order to have a pair short cut on the upper-left and down-left inputs, while the other two were coupled on the other inputs. The filtered white noise was sent to the first pair and its opposite was sent to the other pair. In this way it was possible to simulate a x-motion noise. Of course, for the measurement of the yTF the upper-left and upper-right inputs were coupled. In this way it was possible to measure both the direct and the mixed transfer function, i.e. driving on x and looking on the x and y behavior. The results are summarized in fig. 6.8, where all the TFs are reported.

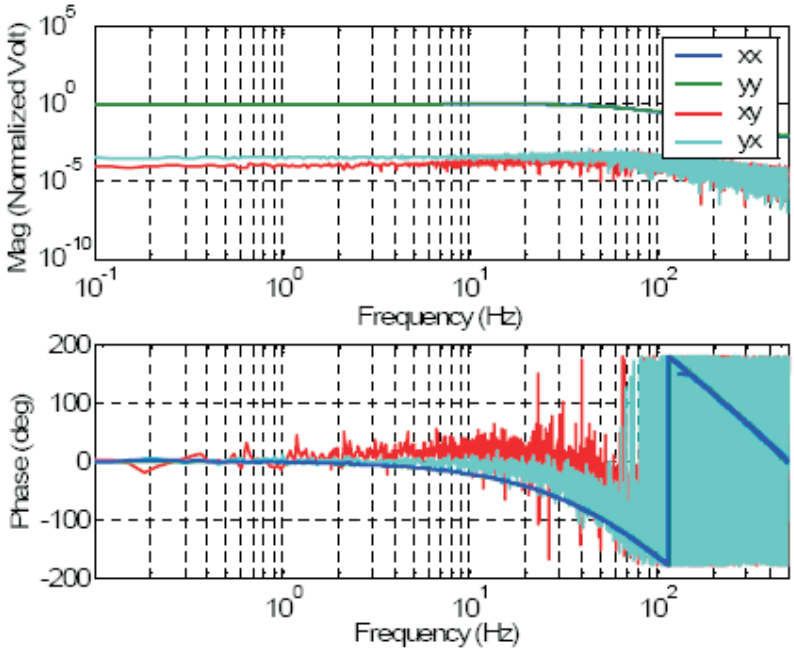

Figure 6.8: Transfer functions of the front-end electronics of the PSD.

As it is possible to see, the two direct TFs (xx and yy) have basically the same behavior. The form of the TFs can be easily explained taking into account the 3 low pass filtering stages included in the PSD front-end electronics, and the phase-delay due to the digital acquisition systems. By putting all these factors together, it is possible to fit the experimental results, at least for the direct transfer functions, with a simple model. The model contains, a part the phase delay due to the 1 kHz sampling rate, a simple pole at 40 Hz and two single poles at 180 Hz. In fig. 6.9 the comparison between the model and the data is reported. The agreement is very good, especially in the low frequency band, up to 100 Hz.

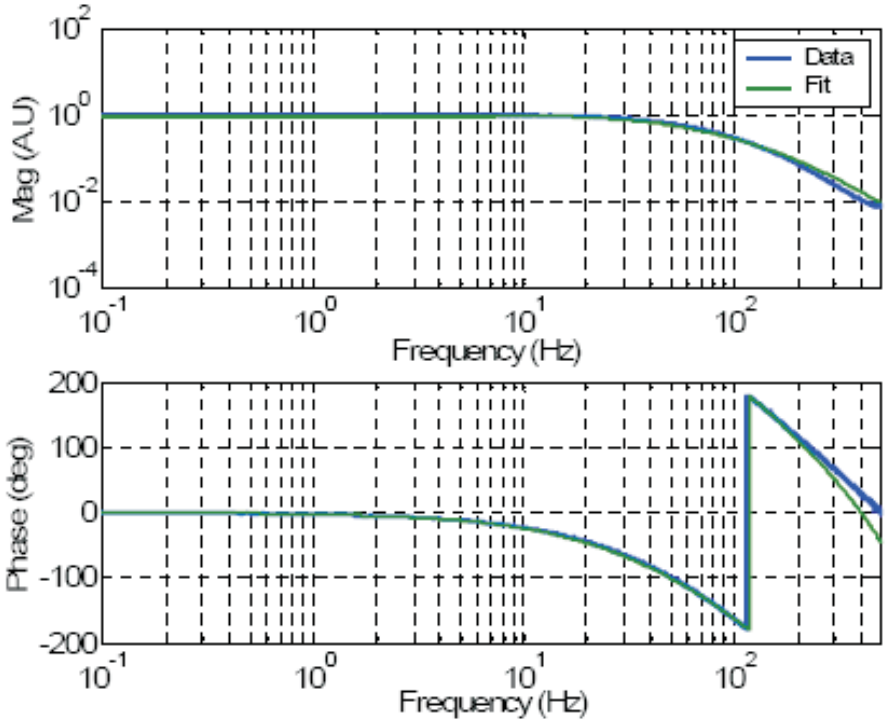

Figure 6.9: Comparison between the data and the model of the front-end electronics transfer function.

6.4.2 Characterization of the PZT mirror

The PZT tilting mirror was fully characterized by using the experimental set-up described above. The characterization consisted in: measuring the transfer function, the linearity and the repeatability of the positioning. Since this devices is provided with an integrated position sensor, it is possible to use it in closed loop conditions. In this way the driving is performed on the locally measured mirror position and not directly on the PZT voltage. For the sake of completeness all the measurements were performed both in open and closed loop conditions.

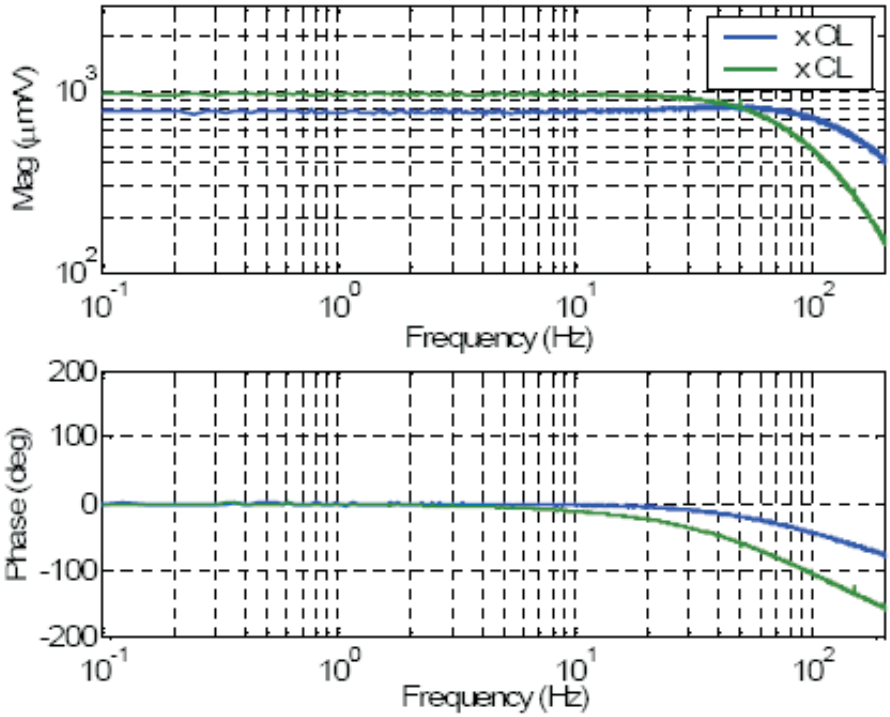

Figure 6.10: Transfer Function of the PZT tilting mirror, x axis, in open and closed loop conditions.

Transfer Function measurement

The measurement of the transfer function of the PZT tilting mirror was performed by applying a digitally filtered white noise to each driving channel of the PZT front end electronics. The digital filter used in this measurement was the same used to measure the TF of the PSD front end electronics. The fig. 6.10 reports the result obtained for the x axis, both in open and closed loop conditions. Of course the

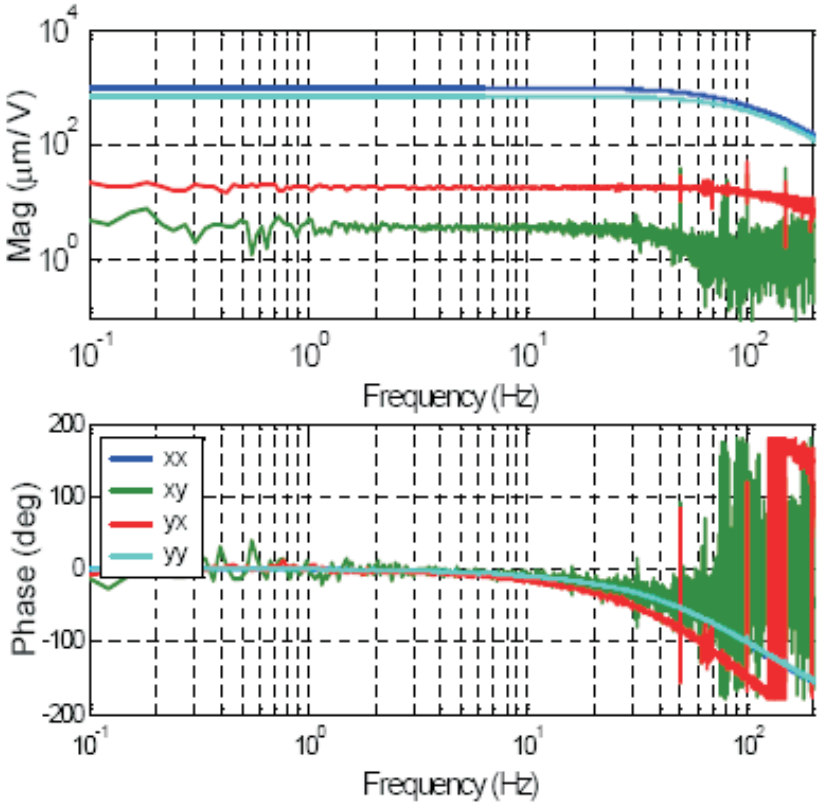

Figure 6.11: Complete set of the transfer functions of the PZT.

effect of the PSD electronics was removed by using the theoretical model discussed above. It is interesting to note that the frequency band of the device goes from 100 *Hz* to 50 *Hz* by switching from open to closed loop. The measurement performed

on the y axis shows the same behavior, except from a different DC gain due to the geometrical configuration of the set-up.

It is also interesting to compare the direct transfer function, to the indirect ones. The comparison is reported in fig. 6.11, and refers to a measurement performed in closed loop. It is possible to note the slight difference between the x and y axis, a factor $1/\sqrt{2}$ due to the angle of 45 degrees formed by the tilting mirror and the impinging beam, as well as a very small coupling between the two DoF. In the worst case the measured coupling was 2.5 % in open loop and 0.5 % in closed loop.

Linearity measurement

The linearity of the PZT mirror was estimated by applying a linear ramp signal to the driving electronics, in order to make the beam spanning the full size of the PSD. Of course in this kind of measurement it is important to take into account the possible non linearity of the sensor. The best performances can be obtained by using only the central area of the PSD, in particular, following the nominal characteristics provided by the manufacturer, the most linear response area is the internal circle with 0.45 mm radius. In order to not overestimate the non linearity of the PZT mirror, even if the scanning was performed almost on the full available area, the measurement of the linearity was performed only on the optimal PSD range.

The measurement, also in this case, was performed on both the axis and in open and closed loop. Of course, due to the well known hysteretic behavior of a piezo, the open loop measurement results very non liner. The results are reported in fig. 6.12, and refers to the x axis span, with the y position close to the zero. Of course the result for the y axis is very similar. The estimated non linearity is about 0.4%.

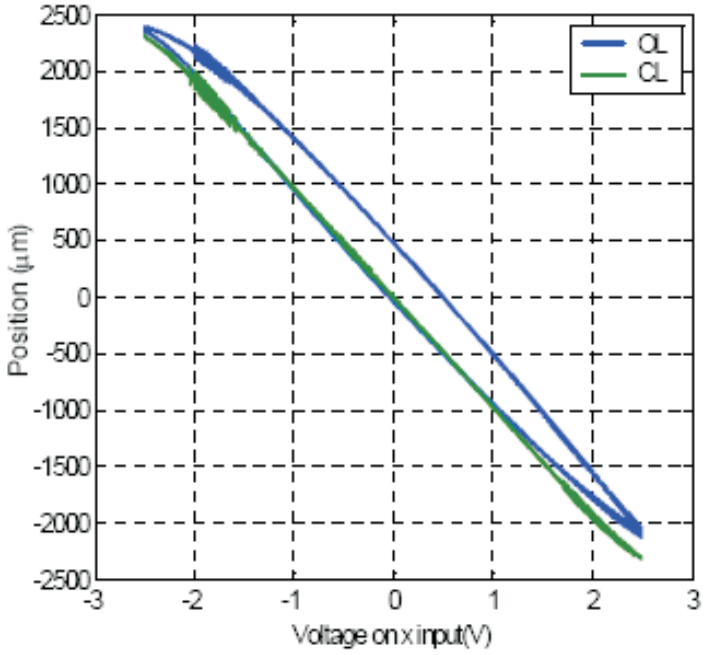

Figure 6.12: Linearity measurement for PZT mirror in open and closed loop.

In fig. 6.12 it is also evident the effect of the increasing non linearity of the PSD as the beam approaches to the edges of the sensors (the active area of the PSD is 4.7x4.7 mm^2).

Repeatability measurement

The repeatability of positioning of the PZT tilting mirror is a crucial characteristic of this device, since it is involved with high precision beam positioning that requires high performances in order to satisfy the requirements of the applications. This is true for both the foreseen applications: fast quadrant centering and scanning wave-front sensor. The measurement of the repeatability was performed by applying a square wave signal to the driving electronics of the PZT mirror. In this way it is

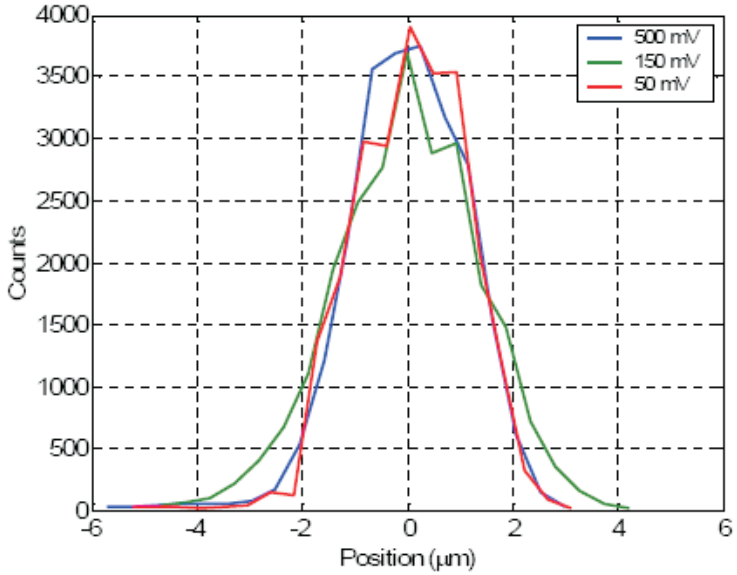

Figure 6.13: Residual motion of the beam around the issued positions along the x axis.

possible to place the beam in two suitable positions, inside the PSD active area, and to measure the residual motion around those positions. This measurement gives a clear idea of the quality and repeatability of the issued positions.

In fig. 6.13 an example of the measurement results is reported. It refers to the closed loop residual motion around a issued position, for three different amplitude square wave: 500, 150 and 50 mV. In all the cases the wave frequency was 1 Hz and the same number of points (N=10^4) was considered to build the histograms. These were built by using only the points close to the target positions as it is shown in fig. 6.14. Of course, to better compare the results for each amplitude, the mean value of the position was removed and only the residual motion around it is reported. The standard deviations of the residual motion, for the measurements shown in fig. 6.13 are respectively: 1.1, 1.4 and 1.1 μm. Very similar results come from the same measurements performed on the y axis.

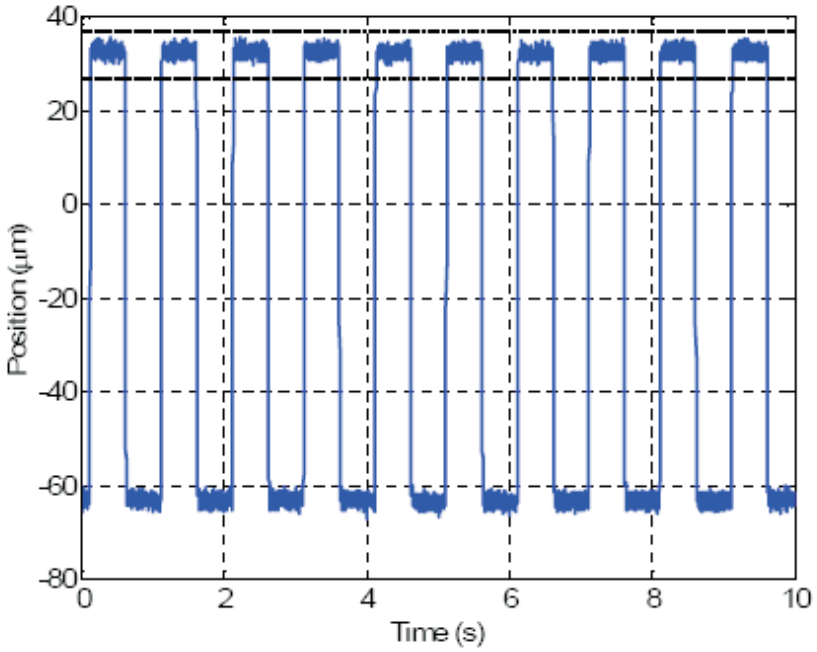

Figure 6.14: Time evolution of the beam position by driving the PZT with a 50 mV, 1 *Hz*, square wave. The data included between the two dash-dotted lines were used to build the histogram.

6.4.3 Tests results

It is important to point out that, in the measured performed all the requirements are referred to tilts while the results are expressed in positions on the PSD. In order to express them in *rad* we can normalize them to the length of the arm between the tilting device and the PSD, remembering that this distance is 10 *cm*. Table 6.1 summarizes all the results.

There are some comment to do about the results quoted in the table. Concerning the dynamic range, no measurements were performed, but the nominal characteristics

Device	PZT	Requirement
Dynamic Range (mrad)	OK	2
Bandwidth (Hz)	50	50
Resolution (μrad)	OK	$13 rms$
Repeatability (μrad)	11	10
Non Linearity (%)	0.4	
Coupling (%)	0.5	
Optics diameter (mm)	12.5	15

Table 6.1: PZT tilting device performances.

of the device were used. Also for the resolution, no dedicated measurement was done, but these characteristics is mainly limited by the input noise voltage. As a measure of the intrinsic resolution of the device, the standard deviation, as measured during the repeatability tests, can be used. Concerning this last characteristic, it is important to stress that the repeatability measured is strongly biased by the intrinsic jitter of the beam due to the experimental set-up itself. Finally there are no explicit requirements for the linearity and the coupling between the two axis, but since also these characteristics are important, they are included in the table.

In conclusion the PZT tip-tilt mirror tested is a good device to perform the scanning of the beam for the scanning wavefront application, since it is very linear, repeatable and has reduced size.

6.5 Implementation in Virgo: first images acquisition

After the tests on tilting mirror, the scanning wavefront system, has been installed on the Virgo detection bench.

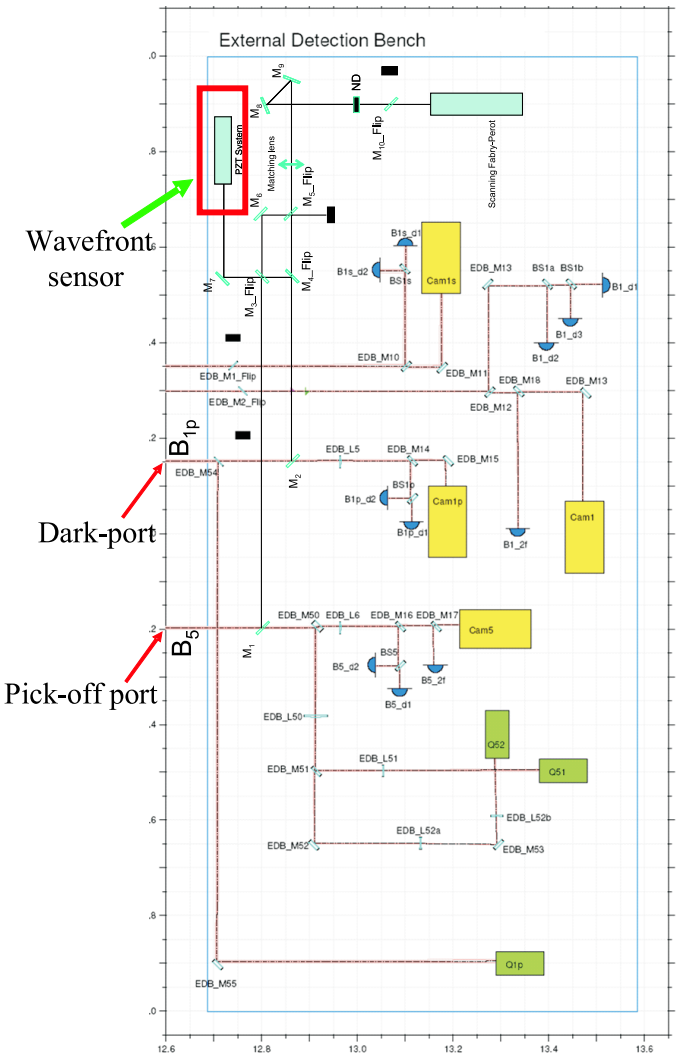

Figure 6.15: Virgo detection bench optical layout with the scanning wavefront system, the dark port and the pick-off port evidenced.

In fig. 6.15 is drawn the Virgo detection bench optical layout with the scanning wavefront system, the dark port and the pick-off port evidenced. As first step the pick-off port signal has been taken. In fact, as we saw, it seems the best to recover aberrations of the sidebands with respect to the carrier.

A simple algorithm that implements a spiraling motion was used for the scanning. In fig. 6.16-6.17 are shown the spiral path for both the driving signals and the real motion of the mirror obtained taking the DC component of the pick-off port (BS) photodiode signal. The mirror is driven by a quadratic spiral which is smoothened in the real motion due to the limited bandwidth of the tilting mirror.

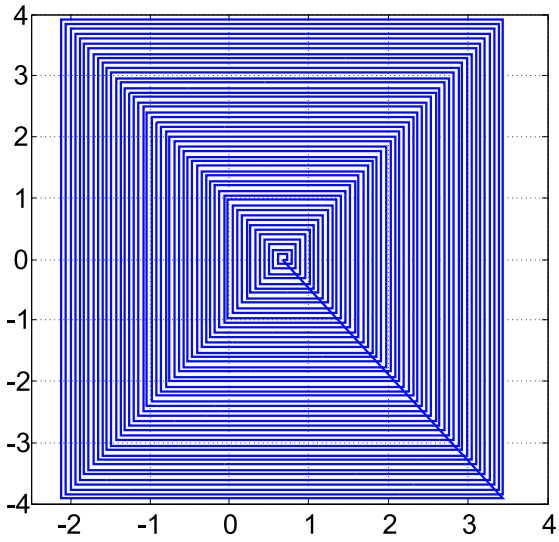

Figure 6.16: Mirror driving spiral.

In fig. 6.18-6.20 are shown the first beam images acquired by the scanning wavefront system at the pick-off port. In particular, fig. 6.18 is the simple DC component while fig. 6.19-6.20 are the in-quadrature and in-phase images at the modulation frequency $\omega = 6.26\ MHz$.

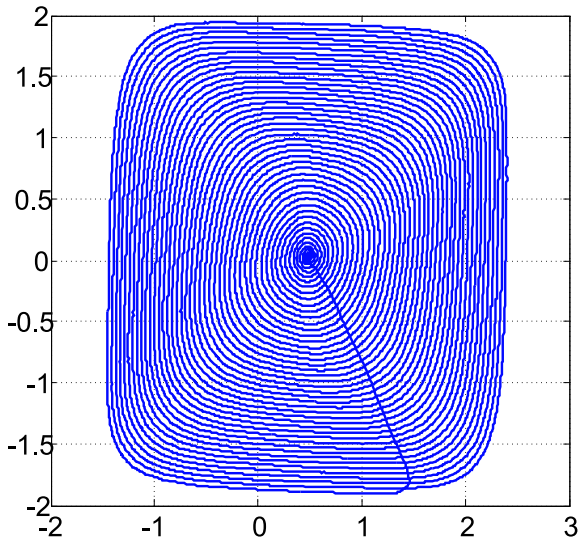

Figure 6.17: Real motion smoothened spiral.

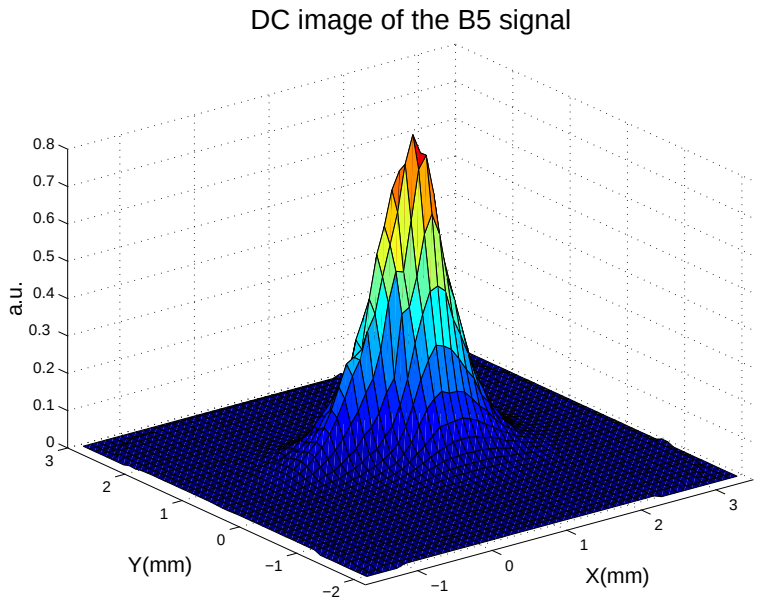

Figure 6.18: DC image of the B5 signal at the pick-off port.

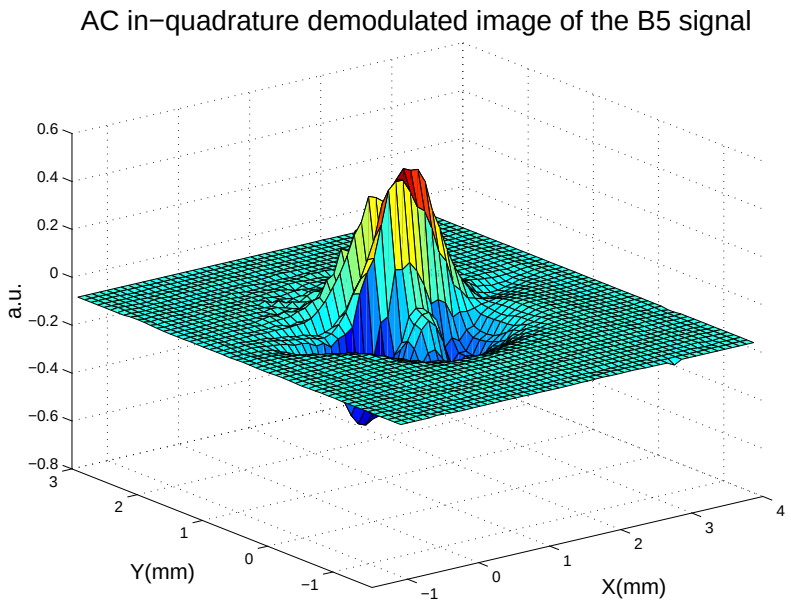

Figure 6.19: In-quadrature demodulated image of the B5 signal at the pick-off port.

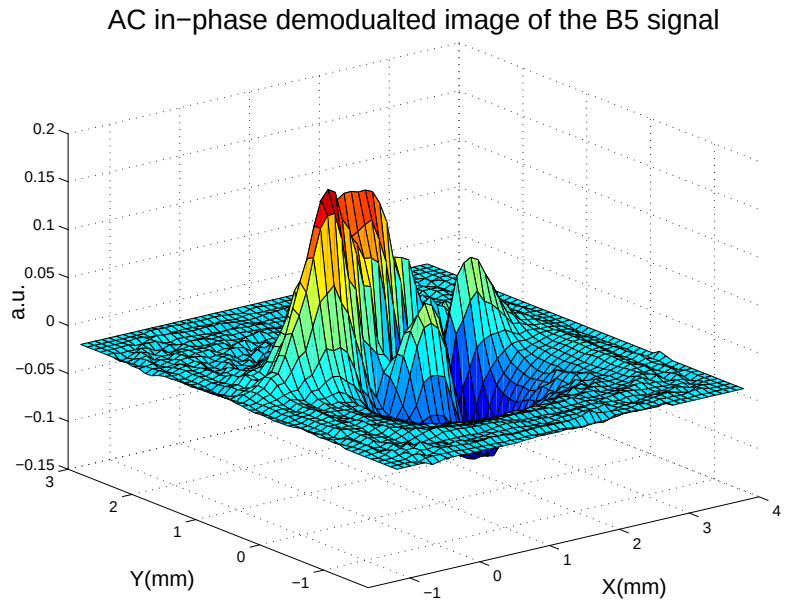

Figure 6.20: In-phase demodulated image of the B5 signal at the pick-off port.

We can focus now to the in-phase demodulated image which, following eq. 6.34, will give us the main informations about the sidebands aberrations respect to the carrier. In fig. 6.20 is shown the in-phase image when the interferometer is longitudinally controlled, which is the minimum condition to have a detectable signal in B5 for the images reconstruction. If we look at this image after a rotation around x-y axis (fig. 6.21), strong tilt components are intuitively evident. However, we must remark that in this condition, with rough alignment operating (but not fine alignment), the in-phase aberrations signal at B5 is the sum of two components.

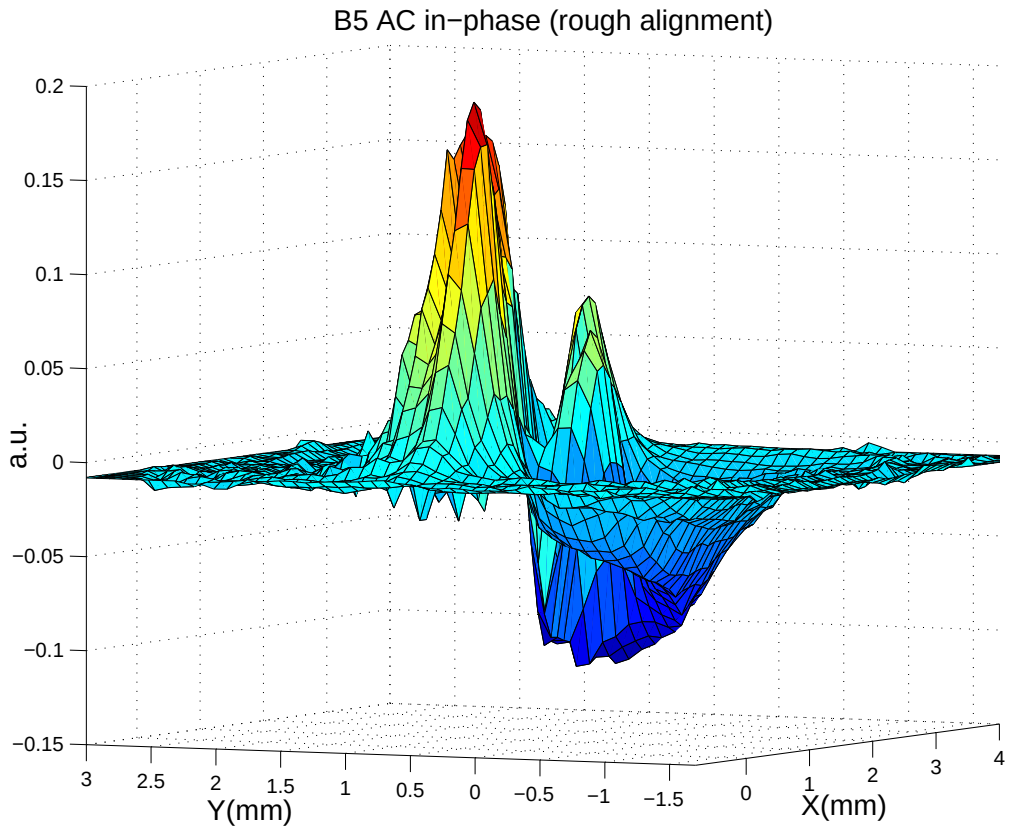

Figure 6.21: B5 AC in-phase rough alignment.

The first (only for the tilts components) is generated by rough aligning of angular degrees of freedom: the carrier takes first order aberration terms (ψ_{10} and ψ_{01}) which interfere with the sidebands fields inside the recycling cavity bringing to the strong tilt terms observed. The second is just our signal, the aberrations of the sidebands respect to the carrier. In the case of fig. 6.21 the strong tilts evidenced are due mainly to the first effect. For this reason, a second acquisition has been performed when the interferometer was in the fine alignment condition, the image is shown in fig. 6.22, where it is evident the reduction of angular tilts.

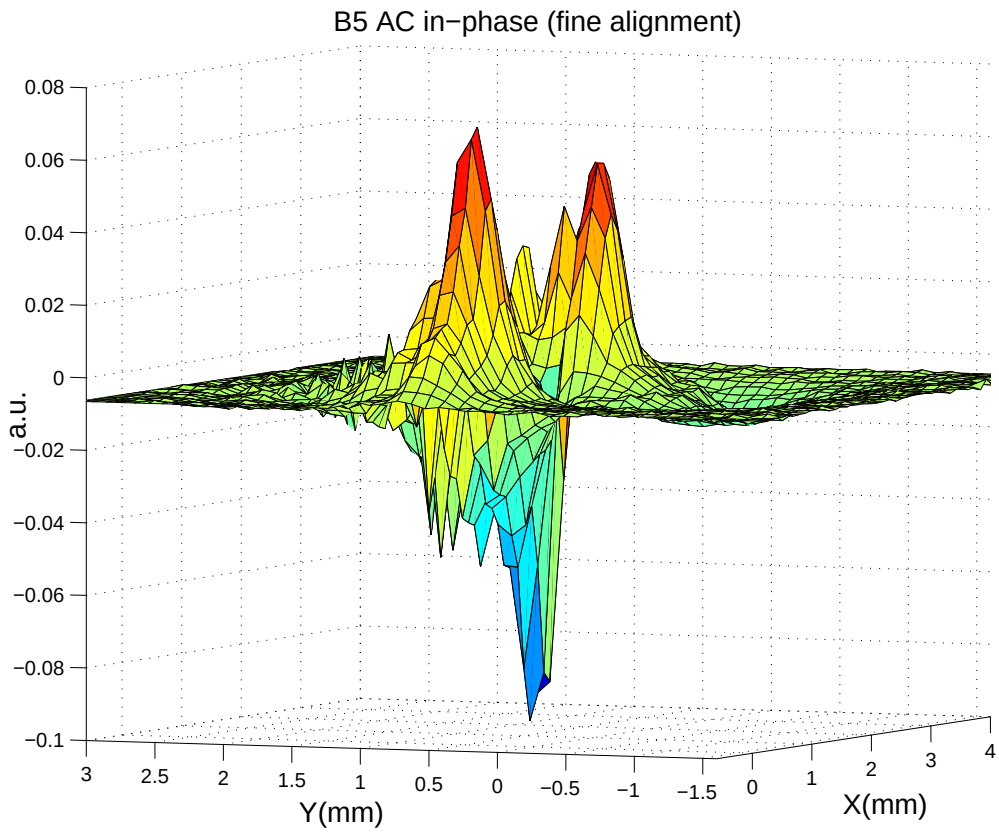

Figure 6.22: B5 AC in-phase fine alignment.

Nevertheless, residual aberrations are present either for tilts (due to residual angular misalignments of the cavity arm) or for second order aberrations (essentially defocus and astigmatism) which are interpreted as sidebands aberrations due to mirror thermal deformations. These results can be well understand by projecting the aberrated fields onto the classical Hermite-Gauss modes (like in par. 4.4.2). The coefficients of aberrations for the two case are shown in fig. 6.23, where the tilts coefficients are referred, essentially, to carrier aberrations respect to the carrier fundamental mode, while the other coefficients are referred to sidebands aberrations respect to the sidebands fundamental mode.

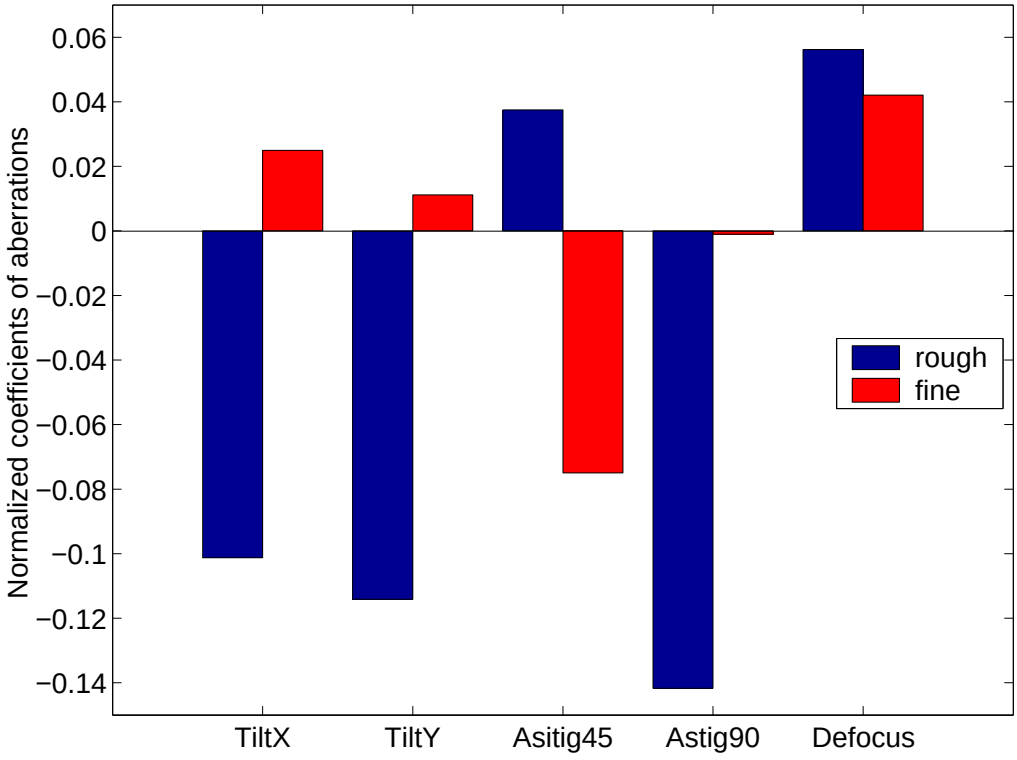

Figure 6.23: Normalized coefficients of aberrations with rough (blue) and fine alignment (red).

In conclusion, the system developed has been installed on the Virgo detection bench. First tests and image acquisitions have been performed showing the capability of this device in reconstructing the beam spatial profile at the modulation frequency. A first simple analysis shows that with the present input power there are already sidebands aberrations of about 10%. Even if this level of aberrations still allows to control the interferometer, surely for higher power laser will be necessary to perform a thermal compensation. In this case, probably it will be necessary to have a faster wavefront sensor (at least for the transient locking states), as it could be the matrix photodiode discussed before (chapter 4). However, the wavefront signal extraction technique developed here could be used in the same way.

Conclusions

In this thesis it has been studied the possibility to apply Adaptive Optics techniques in the framework of gravitational wave interferometers, in particular for the Virgo detector.

In the first part of the work it has been realized a Michelson interferometer controlled with Adaptive Optics based on deformable mirrors. A particular signal extraction technique based on interferometric wavefront detection using a photodiodes array has been developed. By using this technique it is possible to extract directly (through simple combinations of array signals) the coefficient of aberrations of the laser beam in terms of Hermite-Gauss higher order modes. In particular, the system has shown an efficiency of about 60 dB at low frequency, a unity gain of about 50-60 Hz and a reintroduced noise at high frequency under the limit $\tilde{A}_{mn} < 10^{-5}\frac{1}{\sqrt{Hz}}$ foreseen for the application in the Virgo interferometer.

This system could be implemented in a gravitational wave interferometer by using two deformable mirrors acting on the beam before the mode-cleaner. The implementation of this system could be used to correct the thermally induced aberrations as well as to perform a fast pre-mode-cleaning of the input laser beam already in the present detectors if necessary, or surely in the next generation high power interferometers.

A different and interesting application of this system is the generation of non-

Gaussian flat laser beams proposed to reduce the thermoelastic noise in advanced gravitational wave interferometers. In fact, as demonstrated, a system based on a couple of deformable mirrors can be used to produce Flat-Beams starting from standard Gaussian beams. Even if the system is not yet optimized, the results demonstrate the feasibility of such technique.

The last part of the thesis focused on the problem of thermal deformation effects of the Virgo mirrors induced by laser power absorption. In particular, a wavefront signal extraction technique to analyze the fields (the expected aberrated sidebands respect to the carrier) at the output of the Virgo interferometer has been studied. Then, a wavefront sensor based on a scanning pin-hole system to reconstruct field images at the modulation frequency has been realized. The system has been installed on the Virgo detection bench and first tests and image acquisitions have been performed, showing the capability of this device in reconstructing the beam spatial profile at the modulation frequency. A first simple analysis has shown that with the present input power there are already sidebands aberrations of about 10%. Even if this level of aberrations still allows to control the interferometer, surely for higher power laser will be necessary to perform a thermal compensation. In this case, it will be necessary to have a faster wavefront sensor: the photodiodes array used in the first part of the thesis is presently the planned solution.

In conclusion, Adaptive Optics techniques have *entered* the gravitational wave interferometric detectors: if the planned high power input lasers will be used in the next generation of interferometers, Adaptive Optics will represent a powerful tool to reach the desired sensitivity.

Appendix A

Calculation of the c_{ij} coefficients

Referring to the photodiodes matrix in fig. A.1 and to the equation A.1, we can found the coefficients $\mathbf{c}_{ij}(l, w_0)$.

$$|\mathbf{E}_{tot}|^2/2A^2 = |\mathbf{E}_1 + \mathbf{E}_2|^2/2A^2 = (1+\phi)|\Psi_{00}|^2 + \mathbf{a^*}_x\Psi_{00}\Psi_{10} +$$
$$+\mathbf{a^*}_y\Psi_{00}\Psi_{01} + \mathbf{a^*}_{45}\Psi_{00}\Psi_{11} +$$
$$+\mathbf{a^*}_{90}\Psi_{00}(\Psi_{20} - \Psi_{02})/\sqrt{2} + \mathbf{a^*}_D\Psi_{00}(\Psi_{20} + \Psi_{02})/\sqrt{2} \qquad \text{(A.1)}$$

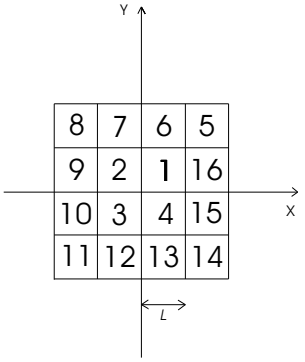

Figure A.1: Photodiodes matrix.

Consider the following functions (depending by l and w_0). These will be used later to find the six signals expressions.

$$\int_{-2l}^{2l} \exp\left(-\frac{2x^2}{w_0^2}\right)dx = \sqrt{2\pi}\frac{w_0}{2} erf\left(\frac{4l}{w_0}\right) \equiv \mathbf{K}_1(l) \tag{A.2}$$

$$\frac{4\sqrt{2}}{w_0^2}\int_{-2l}^{2l} x^2 \exp\left(-\frac{2x^2}{w_0^2}\right)dx = 4\sqrt{2}l\exp\left(-\frac{8l^2}{w_0^2}\right) + \sqrt{\pi}w_0 erf\left(\frac{4l}{w_0}\right) \equiv \mathbf{K}_2(l) \tag{A.3}$$

$$\frac{2\sqrt{2}}{w_0^2}\int_{0}^{2l} x \exp\left(-\frac{2x^2}{w_0^2}\right)dx = \frac{\sqrt{2}}{2}w_0\left[1-\exp\left(-\frac{8l^2}{w_0^2}\right)\right] \equiv \mathbf{K}_3(l) \tag{A.4}$$

$$\int_{-l}^{l} \exp\left(-\frac{2x^2}{w_0^2}\right)dx = \sqrt{2\pi}\frac{w_0}{2} erf\left(\frac{2l}{w_0}\right) \equiv \mathbf{K}_4(l) \tag{A.5}$$

$$\frac{4\sqrt{2}}{w_0^2}\int_{-l}^{l} x^2 \exp\left(-\frac{2x^2}{w_0^2}\right)dx = 2\sqrt{2}l\exp\left(-\frac{2l^2}{w_0^2}\right) + \sqrt{\pi}w_0 erf\left(\frac{2l}{w_0}\right) \equiv \mathbf{K}_5(l) \tag{A.6}$$

The first signal is defined as:

$$\mathbf{S}_1 = \int_{-2l}^{2l} dx \int_{-2l}^{2l} dy |\mathbf{E}_{tot}|^2 \tag{A.7}$$

Since the integrals containing the products $\Psi_{00}\Psi_{10}, \Psi_{00}\Psi_{01}, \Psi_{00}\Psi_{11}, \Psi_{00}(\Psi_{20}-\Psi_{02})$ give a null contribution for symmetry, we have:

$$\mathbf{S}_1 = \int_{-2l}^{2l} dx \int_{-2l}^{2l} dy \left[(1+\phi)|\Psi_{00}|^2 + \mathbf{a}^*{}_D \Psi_{00}(\Psi_{20}+\Psi_{02})\right] =$$

$$= N_{00}^2(1+\phi)\int_{-2l}^{2l}\int_{-2l}^{2l} dxdy \exp\left(-2\frac{x^2+y^2}{w_0^2}\right) +$$

$$N_{00}N_{20}\mathbf{a^*}_D \int_{-2l}^{2l}\int_{-2l}^{2l} dxdy \left[\frac{4}{w_0^2}(x^2+y^2)-2\right] \exp\left(-2\frac{x^2+y^2}{w_0^2}\right) =$$

$$= N_{00}^2\mathbf{K}_1^2(l)(1+\phi) + N_{00}N_{20}[2\mathbf{K}_1\mathbf{K}_2 - 2\sqrt{2}\mathbf{K}_1^2]\,\mathbf{a^*}_D =$$

$$= \mathbf{c}_{11}(l,w_0)[1+\phi] + \mathbf{c}_{16}(l,w_0)\mathbf{a}_D^* \tag{A.8}$$

The second signal is defined as:

$$\mathbf{S}_2 = \int_{-2l}^{2l} dy \left[\int_0^{2l} dx|\mathbf{E}_{tot}|^2 - \int_{-2l}^{0} dx|\mathbf{E}_{tot}|^2\right]$$

Since the integrals containing the products $|\Psi_{00}|^2, \Psi_{00}\Psi_{01}, \Psi_{00}\Psi_{11}, \Psi_{00}(\Psi_{20}-\Psi_{02})$, $\Psi_{00}(\Psi_{20}+\Psi_{02})$ give a null contribution for symmetry, we have:

$$\mathbf{S}_2 = \mathbf{a^*}_x \int_{-2l}^{2l} dy \left[\int_0^{2l} dx\Psi_{00}\Psi_{10} - \int_{-2l}^{0} dx\Psi_{00}\Psi_{10}\right] =$$

$$= \mathbf{a^*}_x a_x) 2N_{00}N_{10} \int_{-2l}^{2l} dy \int_0^{2l} \frac{\sqrt{2\pi}}{w_0} x \exp\left(-2\frac{x^2+y^2}{w_0^2}\right) dx =$$

$$= 2N_{00}N_{10}\mathbf{K}_1\mathbf{K}_3\,\mathbf{a^*}_x = \mathbf{c}_{22}(l,w_0)\mathbf{a}_x^* \tag{A.9}$$

The third signal is defined as:

$$\mathbf{S}_3 = \int_{-2l}^{2l} dx \left[\int_0^{2l} dy|\mathbf{E}_{tot}|^2 - \int_{-2l}^{0} dy|\mathbf{E}_{tot}|^2\right] \tag{A.10}$$

It is evident that for $\mathbf{S}_3$ we have the same result of $\mathbf{S}_2$:

$$\mathbf{S}_3 = 2N_{00}N_{01}\mathbf{K}_1\mathbf{K}_3\,\mathbf{a}^*{}_y = \mathbf{c}_{33}(l, w_0)\mathbf{a}^*_y \tag{A.11}$$

The fourth signal is defined as:

$$\mathbf{S}_4 = \int_0^{2l} dx \int_0^{2l} dy|\mathbf{E}_{tot}|^2 + \int_{-2l}^{0} dx \int_{-2l}^{0} dy|\mathbf{E}_{tot}|^2 +$$

$$- \int_0^{2l} dx \int_{-2l}^{0} dy|\mathbf{E}_{tot}|^2 - \int_{-2l}^{0} dx \int_0^{2l} dy|\mathbf{E}_{tot}|^2 \tag{A.12}$$

Since the integrals containing the products $|\Psi_{00}|^2, \Psi_{00}\Psi_{10}, \Psi_{00}\Psi_{01}, \Psi_{00}(\Psi_{20} - \Psi_{02})$, $\Psi_{00}(\Psi_{20} + \Psi_{02})$ give a null contribution for symmetry, we have:

$$\mathbf{S}_4 = \left[\int_0^{2l} dx \int_0^{2l} dy\Psi_{00}\Psi_{11} + \int_{-2l}^{0} dx \int_{-2l}^{0} dy\Psi_{00}\Psi_{11} +\right.$$

$$\left. - \int_0^{2l} dx \int_{-2l}^{0} dy\Psi_{00}\Psi_{11} - \int_{-2l}^{0} dx \int_0^{2l} dy\Psi_{00}\Psi_{11}\right] =$$

$$= \mathbf{a}^*{}_{45}a_{45})4N_{00}N_{11}\int_0^{2l} dy \int_0^{2l} \frac{2\pi}{w_0^2} xy \exp\left(-2\frac{x^2+y^2}{w_0^2}\right)dx =$$

$$= 4N_{00}N_{11}\mathbf{K}_3^2\,\mathbf{a}^*{}_{45} = \mathbf{c}_{44}(l, w_0)\mathbf{a}^*_{45} \tag{A.13}$$

The fifth signal is defined as:

$$\mathbf{S}_5 = \int_l^{2l} dy \int_{-l}^{l} dx|\mathbf{E}_{tot}|^2 + \int_{-2l}^{-l} dy \int_{-l}^{l} dx|\mathbf{E}_{tot}|^2 +$$

$$- \int_l^{2l} dx \int_{-l}^{l} dy|\mathbf{E}_{tot}|^2 - \int_{-2l}^{-l} dx \int_{-l}^{l} dy|\mathbf{E}_{tot}|^2 \tag{A.14}$$

Since the integrals containing the products $|\Psi_{00}|^2, \Psi_{00}\Psi_{10}, \Psi_{00}\Psi_{01}, \Psi_{00}\Psi_{11}$, $\Psi_{00}(\Psi_{20}+\Psi_{02})$ give a null contribution for symmetry, we have:

$$\mathbf{S}_5 = \int_l^{2l} dy \int_{-l}^{l} dx \Psi_{00} \frac{(\Psi_{20}-\Psi_{02})}{\sqrt{2}} + \int_{-2l}^{-l} dy \int_{-l}^{l} dx \Psi_{00} \frac{(\Psi_{20}-\Psi_{02})}{\sqrt{2}} +$$

$$- \int_l^{2l} dx \int_{-l}^{l} dy \Psi_{00} \frac{(\Psi_{20}-\Psi_{02})}{\sqrt{2}} - \int_{-2l}^{-l} dx \int_{-l}^{l} dy \Psi_{00} \frac{(\Psi_{20}-\Psi_{02})}{\sqrt{2}} =$$

$$= \mathbf{a}^*{}_{90} a_{90}) 4 N_{00} N_{20} \int_l^{2l} dy \int_{-l}^{l} \frac{4}{w_0^2}(x^2-y^2) \exp\left(-2\frac{x^2+y^2}{w_0^2}\right) dx =$$

$$= 2N_{00}N_{20}[\mathbf{K}_1\mathbf{K}_5 - \mathbf{K}_2\mathbf{K}_4]\,\mathbf{a}^*{}_{90} = \mathbf{c}_{55}(l, w_0)\mathbf{a}^*_{90} \tag{A.15}$$

Finally, the sixth signal is defined as:

$$\mathbf{S}_6 = \int_{-l}^{l} dx \int_{-l}^{l} dy |\mathbf{E}_{tot}|^2 - \int_{-2l}^{2l} dx \int_{l}^{2l} dy |\mathbf{E}_{tot}|^2 - \int_{-2l}^{2l} dx \int_{-2l}^{-l} dy |\mathbf{E}_{tot}|^2 +$$

$$- \int_{-l}^{l} dy \int_{l}^{2l} dx |\mathbf{E}_{tot}|^2 - \int_{-l}^{l} dy \int_{-2l}^{-l} dy |\mathbf{E}_{tot}|^2 \tag{A.16}$$

Since the integrals containing the products $\Psi_{00}\Psi_{10}, \Psi_{00}\Psi_{01}, \Psi_{00}\Psi_{11}, \Psi_{00}(\Psi_{20}-\Psi_{02})$ give a null contribution for symmetry, we have:

$$\mathbf{S}_6 = \int_{-l}^{l} dx \int_{-l}^{l} dy \left[(1+\phi)|\Psi_{00}|^2 + \mathbf{a}^*{}_D a_D)\Psi_{00} \frac{(\Psi_{20}+\Psi_{02})}{\sqrt{2}}\right] +$$

$$-4 \int_{-l}^{l} dx \int_{l}^{2l} dy \left[(1+\phi)|\Psi_{00}|^2 + \mathbf{a}^*{}_D a_D)\Psi_{00} \frac{(\Psi_{20}+\Psi_{02})}{\sqrt{2}}\right] +$$

$$-4\int_l^{2l} dx \int_l^{2l} dy \left[(1+\phi)|\Psi_{00}|^2 + \mathbf{a^*}_D a_D)\Psi_{00}\frac{(\Psi_{20}+\Psi_{02})}{\sqrt{2}}\right] =$$

$$= (1+\phi)N_{00}^2 \left[\int_{-l}^{l} dx \int_{-l}^{l} dy \exp\left(-2\frac{x^2+y^2}{w_0^2}\right) +\right.$$

$$\left. -4\int_{-l}^{l} dx \int_{l}^{2l} dy \exp\left(-2\frac{x^2+y^2}{w_0^2}\right) - 4\int_{l}^{2l} dx \int_{l}^{2l} dy \exp\left(-2\frac{x^2+y^2}{w_0^2}\right)\right] +$$

$$+N_{00}N_{20}\mathbf{a^*}_D \left\{\int_{-l}^{l} dx \int_{-l}^{l} dy 2\sqrt{2}\left[\frac{2}{w_0^2}(x^2+y^2)-1\right]\exp\left(-2\frac{x^2+y^2}{w_0^2}\right) +\right.$$

$$-4\int_{-l}^{l} dx \int_{l}^{2l} dy 2\sqrt{2}\left[\frac{2}{w_0^2}(x^2+y^2)-1\right]\exp\left(-2\frac{x^2+y^2}{w_0^2}\right)+$$

$$\left. -4\int_{l}^{2l} dx \int_{l}^{2l} dy 2\sqrt{2}\left[\frac{2}{w_0^2}(x^2+y^2)-1\right]\exp\left(-2\frac{x^2+y^2}{w_0^2}\right)\right\} =$$

$$= N_{00}^2[2\mathbf{K}_4^2 - \mathbf{K}_1^2](1+\phi)] + N_{00}N_{20}\left[4\mathbf{K}_4\mathbf{K}_5 - 2\mathbf{K}_1\mathbf{K}_2 + 4\sqrt{2}\mathbf{K}_2\mathbf{K}_4 +\right.$$

$$\left. -4\sqrt{2}\mathbf{K}_1\mathbf{K}_4 + 2\sqrt{2}\mathbf{K}_1^2 - 4\sqrt{2}\mathbf{K}_4^2\right]\ \mathbf{a^*}_D = \mathbf{c}_{61}(l,w_0)(1+\Phi) + \mathbf{c}_{66}(l,w_0)\mathbf{a}_D^* \quad \text{(A.17)}$$

Bibliography

[1] S. Weinberg, *Gravitation and cosmology: principles and applications of the general theory of Relativity*, john wiley-Sons, New York (1972).

[2] C.W. Misner, K.S. Thorne, J. Wheeler, *Gravitation*, W. H. Freeman, San Francisco (1973).

[3] C. Moller, *The theory of relativity*, Oxford University Press, New Delhi (1972).

[4] R.M. Wald, *General relativity*, The University of Chicago Press, Chicago, (1984).

[5] D.G. Blair, *The detection of gravitational waves*, Cambridge U. Press, Cambridge (1991).

[6] S. Bonazzola, J.A. Marck, , *Astrophysical sources of gravitational radiation*, Annu. Rev. Nucl. Part. Sci., 45, 655-717 (1994).

[7] K.S. Thorne, *Probing black holes and relativistic stars with gravitational waves*, gr-qc/9706079 (1997).

[8] K.S. Thorne, *Gravitational waves from compact bodies*, in Proc. of IAU Symposium 165, Compact stars in binaries, also gr-qc/9506084 (1995).

[9] E.E. Flanagan, *Astrophysical sources of gravitational radiation and prospects for their detection*, gr-qc/9804024 (1998).

[10] M. Maggiore, *High-energy physics with gravitational wave experiments*, e-Print Archive: gr-qc/9803028, (1998).

[11] B. Allen, *The Stochastic gravity wave background: Sources and detection*, in the proceedings of Astrophysical Sources of Gravitational Radiation, Les Houches, France, 26 Sep - 6 Oct 1995. e-Print Archive: gr-qc/9604033.

[12] A. Buonanno, M. Maggiore, C. Ungarelli, *Spectrum of relic gravitational waves in string cosmology*, Phys. Rev. D, 55:3330-3336, (1997).

[13] P.R. Saulson, *Fundamentals of Interferometric Gravitational Wave Detectors*, World Scientific (1994)

[14] A. abramovic et al., *LIGO: The Laser Interferometer Gravitational-Wave Observatory* Science 256, 325 (1992).

[15] A. Brillet, A. Giazotto et al., The VIRGO Project, *Final Conceptual Design of the French-Italian Interferometric Antenna for Gravitational Wave Detection*, unpublished (1992).

[16] D. Sigg (for the LIGO Science Collaboration), *Status of the LIGO detectors*, Proceedings of the 6th Amaldi conference, Class. Quantum Grav. 23 No 8 (21 April 2006) S51-S56

[17] For a Review: LIGO Scientific Collaboration, *Recent results on the search for continuous sources with LIGO and GEO*, Proc of TAUP - Zaragoza (2005).

[18] TAMA Collaboration, *Upper limits from the LIGO and TAMA detectors on the rate of gravitational-wave bursts*, Phys.Rev. D 72: 122004, (2005).

[19] R.V.Pound, *Electronic Frequency Stabilization of Microwave Oscillators*, Rev.Sci.Instrum. 17 490-505 (1946)

[20] R.W.P.Drever et al., *Laser phase and frequency stabilization using an optical resonator*, Appl. Phys. B: Photophys. Laser Chem. 31 (1983) 97-105

[21] L. Pinard et al., *Low loss coatings for the Virgo large mirrors*, Optical Systems design 2003 proc., 2003.

[22] J.M.Mackowski et al., Opt.Quant.Electr., 31(5/7), 507-514, (1999).

[23] G.Ballardin et al., *Measurement of the VIRGO superattenuator performance for seismic noise suppression*, Rev. Sci. Instrum. 72 3643-3652 (2001).

[24] G.Losurdo et al., *An inverted pendulum pre-isolator stage for the VIRGO suspension system*, Rev. Sci. Instrum., 70(5), 2507-2515 (1999).

[25] G. Ballardin et al., *Measurement of the transfer function of the steering filter of the VIRGO super attenuator suspension*, Rev. Sci. Instrum., 72, 3635 (2001).

[26] M. Bernardini et al., *Suspension last stage for the mirrors of the VIRGO interferometric gravitational wave antenna*, Rev. Sci. Instrum., 70, 3463 (1999).

[27] G. Losurdo et al., *Inertial control of the mirror suspensions of the VIRGO interferometer for gravitational wave detection*, Rev. Sci. Instrum., 72, 3654-3661 (2001).

[28] S. Braccini for the VIRGO Collaboration, *The status of VIRGO*, Proceedings of the 6th Amaldi conference, Class. Quantum Grav. 23 No 8 (2006) S63-S69.

[29] L. Barsotti for the VIRGO Collaboration, *The variable finesse locking technique*, Proceedings of the 6th Amaldi conference, Class. Quantum Grav. 23 No 8 (2006) S85-S89.

[30] F.Cavalier, *Le controle global de Virgo*, These d'Habilitation a diriger des Recherches, Universitè de Paris Sud, LAL 01-69 (2001).

[31] D.Z.Anderson, *Alignment of resonant optical cavities*, Appl. Opt., 23, 2944-2949 (1984).

[32] M. Mantovani for the VIRGO Collaboration, *The VIRGO automatic alignment system*, Proceedings of the 6th Amaldi conference, Class. Quantum Grav. 23 No 8 (2006) S91-S101.

[33] F. Acernese, et al., *First locking of the Virgo central area interferometer with suspension hierarchical control*, Astrop. Phys., 20 (6), 629-640 (2004).

[34] A. Vicere for the VIRGO Collaboration, *The status of coalescing binaries search code in Virgo, and the analysis of C5 data*, Proceedings of the 6th Amaldi conference, Class. Quantum Grav. 23 No 8 (2006) S187-S196.

[35] A.C. Clapson for the VIRGO Collaboration, *Testing Virgo burst detection tools on commissioning run data*, Proceedings of the 6th Amaldi conference, Class. Quantum Grav. 23 No 8 (2006) S197-S205.

[36] *Adaptive Optics in Astronomy*, edited by F. Roddier (Cambridge University Press, Cambridge, UK), (1999).

[37] *Adaptive Optics for Industry and Medicine*, edited by S. R. Restaino and S. W. Teare, Albuquerque, (2002).

[38] A. Tokovinin, *Tutorial on adaptive optics at CTIO*, http://www.ctio.noao.edu/

[39] J.W. Hardy, *Adaptive optics for astronomical telescopes*, New York, NY: Oxford University Press (1998).

[40] Tyson, K. Robert, *Introduction to adaptive optics*, Bellingham, WA: SPIE, The International Society for Optical Engineering (2000).

[41] Tyson, K. Robert, *Principles of adaptive optics*, Boston, MA: Academic Press (1998).

[42] E. Dalimier, C. Dainty, *Comparative analysis of deformable mirrors for ocular adaptive optics* , Optics Express 13, 4275-4285 (2005).

[43] J.D. Mansell, J. Hennawi, E.K. Gustafson, M.M. Fejer, R.L. Byer, D. Clubey, S. Yoshida, D.H. Reitze, *Evaluating the Effect of Transmissive Optic Thermal Lensing on Laser Beam Quality With a Shack -Hartmann Wave-Front Sensor*, Appl. Opt. 40, 366-374, (2001).

[44] E. Calloni, J.T. Baker, F. Barone, R. De Rosa, L. Di Fiore, L. Milano, S.R. Restaino, *Adaptive optics approach for prefiltering of geometrical fluctuations of the input laser beam of an interferometric gravitational waves detector*, Rev. Sc. Instr. 74, (4) 2570-2574, (2003).

[45] A. Rüdiger, R. Schilling, L. Schnupp, W. Winkler, H. Billing and K. Maischberger, *A mode selector to suppress fluctuations in laser beam geometry*, Opt. Acta 28, 641, (1981).

[46] Y. Hefetz, M. Mavalvala, D. Sigg, *Principles of calculating alignment signals in complex optical interferometers*, J. Opt. Am. B, 14, 1597-1605, (1997).

[47] F. Barone, E. Calloni, L. Di Fiore, A. Grado, P. Hello, L. Milano, G. Russo, *Effects of Misalignments and Beam Jitters in Interferometric Gravitational Wave Detectors*, Phys. Lett. A 217, 90-96, (1996).

[48] G Mueller, R.S. Amin, D. Guagliardo, D. McFeron, R. Lundock, D.H. Reitze and T.B. Tanner, *Method for compensation of thermally induced modal distortions in the input optical components of gravitational wave interferometers*, Class. Quant. Grav. 19, 1793-1801, (2002).

[49] E. Calloni, F. Barone, L. Di Fiore, A. Grado, P. La Penna, L. Milano, *Effects of misalignment and beam jitter in Fabry-Perot laser stabilization*, Opt. Comm. 142, 50-54, (1997)

[50] H.Kogelnick and T. Li, *Laser beams and resonators*, Appl. Opt. 5 (1966) 1550.

[51] O. Svelto, *Principles of lasers*, Plenum press, New York (1982).

[52] O. Born and E. Wolf, *Principles of Optics*, Pergamon, London, (1970).

[53] E. Morrison, B. J. Meers, D. I. Robertson, H. Ward, *Automatic alignment of optical interferometers* Appl. Opt. 33, 5037 (1994).

[54] F Bondu, A Brillet, F Cleva, H Heitmann, M Loupias, C N Man, H Trinquet and the VIRGO Collaboration Class. Quant. Grav. 19, 1829-1833, (2002).

[55] H. Luck, K.O. Muller, P. Aufmuth, K. Danzmann, *Correction of wavefront distortions by means of thermally adaptive optics*, Opt. Comm. 175, 275-287, (2000).

[56] E. Calloni, A. Brillet, C.N. Man, F. Barone, F. Fusco, R. De Rosa, L. Di Fiore, A. Grado, L. Milano, G. Russo, *Digital Alignment System for a Laser Beam*, Phys. Lett. A 193, 15-20 (1994).

[57] F. Bondu, J.Y. Vinet, *Mirror thermal noise in interferometric gravitational-wave detectors*, Phys. Lett. A 198: 74-78, (1995).

[58] F. Bondu, P. Hello, J.Y. Vinet, *Thermal noise in mirrors of interferometric gravitational wave antennas*, Phys. Lett. A 246: 227-236, (1998).

[59] V.B. Braginsky, M.L. Gorodetsky, *Thermodynamical fluctuations and photo-thermal shot noise in gravitational wave antennae*, S.P. Vyatchanin, Phys. Lett. A 264: 1-10, 1999.

[60] Y.T. Liu, K.S. Thorne, *Thermoelastic noise and homogeneous thermal noise in finite sized gravitational-wave test masses*, Phys. Rev. D 62: 122002, (2000).

[61] J.Y. Vinet, *Mirror thermal noise in flat-beam cavities for advanced gravitational wave interferometers*, Class. Quant. Grav. 22: 1395-1404, (2005).

[62] V. Braginsky et al., LIGO Report No. G010333-00-D, (2001); E. D'Ambrosio, LIGO Report No. G010297-00-D, (2001).

[63] E. D'Ambrosio, *Nonspherical mirrors to reduce thermoelastic noise in advanced gravitational wave interferometers*, Phys. Rev. D 67: 102004, (2003).

[64] E. D'Ambrosio, R. O'Shaughnessy, K.S. Thorne, P. Willems, S. String, S. Vyatchanin, *Advanced LIGO: non-Gaussian beams*, Class. Quant. Grav. 21: S867-S873, (2004).

[65] E. D'Ambrosio, R. O'Shaughnessy, S. String, K.S. Thorne, S. Vyatchanin, *Reducing thermoelastic noise in gravitational-wave interferometers by flattening the light beams*, e-Print Archive: gr-qc/0409075 (Submitted to Phys.Rev. D)

[66] J. Agresti et al., *Design and construction of a prototype of a flat top beam interferometer and initial tests*, J. Phys. Conf. Ser. 32:301-308, (2006).

[67] A. E. Siegman, *Lasers*, University Science Books, Sausalito CA, (1986).

[68] W. Winkler, K. Danzmann, A. Rudiger, R. Schilling, *Heating by optical absorption and the performance of interferometric gravitational-wave detectors*, Phys. Rev. A 44:7022-7036,(1991).

[69] P. Hello, *Compensation for thermal effects in mirrors of gravitational wave interferometers*, Eur. Phys. J. D 15:373-383, (2001).

[70] R. Lawrence, M. Zucker, P. Fritschel, P. Marfuta, D. Shoemaker, *Adaptive thermal compensation of test masses in advanced LIGO*, Class. Quantum Grav. 19, 1803-1812, (2002).

[71] H. Luck, A. Freise, S. Gobler, S. Hild, K. Kawabe, K. Danzmann, *Thermal correction of the radii of curvature of mirrors for GEO 600*, Class. Quantum Grav. 21, S985-S989, (2004).

[72] J. Degallaix, C. Zhao, L. Ju, D. Blair, *Thermal lensing compensation for AIGO high optical power test facility*, Class. Quantum Grav. 21, S903-S908, (2004).

[73] R.C. Lawrence, *Active wavefront correction in laser interferometric gravitational wave detectors*, PhD thesis (2003).

[74] E. D'Ambrosio, *Study of the different responsive behaviour of the sidebands in LIGO I*, Class. Quantum Grav. 21, S1113-S1120, (2004).

[75] E. Calloni, M. Parisi, *Private communication*.

Acknowledgments

Many people helped and encouraged me during the realization of this work.
Special thanks are for my *mentor* Enrico Calloni: for the enormous patience, the total avalaibility and the fundamental collaboration; for all the precious lessons and advice which mainly contributed to my formation; for always believing in me. Thank of all.
Thanks to Prof. Leopoldo Milano for his encouragement, supervision and for always believing in me.
Thanks to Rosario De Rosa, for his essential help and collaboration in laboratory, and to Luciano Di Fiore for his very useful advice.
Thanks to all people of the Naples Virgo group with who I spent the longest part of my time during the last three years. In particular, Alessio Tierno for shearing with me the greatest part of the *hard* laboratory work, Silvio Pardi for the *moral* sustain during the long nights of work and my *adventure's friend* Gennaro Venoso.
Thanks to Sergio Restaino for his precious support and important collaboration.
Thanks to the Virgo collaboration. In particular, to Giovanni Losurdo, Irene Fiori and Edwige Tournafier for their fundamental collaboration during my time spent on the Virgo site in Cascina.
Finally, thanks to all my friends, to my family and my love Isabel, who, even if far from the *Physics World*, always sustained and believed in me.